# Shadow Engineering Semiconductor-Superconductor Hybrid Nanowires for Quantum Devices

Rasmus Dalsgaard Schlosser

Niels Bohr Institute
Center for Quantum Devices
University of Copenhagen

2021
Last revision: August 30, 2021

Academic supervisor: Professor Jesper Nygård

**Abstract**

Semiconductor nanowires are at the very heart of current state of the art experiments in the field of quantum transport. Their dimensions make them a quasi one-dimensional material, and when coupled with a superconductor they constitute a hybrid structure, inheriting the properties of both constituents. This makes them the material of choice in the search for novel qubit systems, proposed to arise from the realisation and control of exotic quantum states. To this end, ultra clean materials that exhibit ballistic transport are required. Epitaxial films, formed under high vacuum have proven to fulfil part of this request. Shadow deposition, has recently emerged as a viable method for forming the necessary semiconductor-superconductor patterns without the introduction of a chemical etchant. This work expands on the shadow patterning concept by establishing the parameters necessary for precise control of the deposition, in order to create designer architectures, with extensive possibilities in design, and rapid prototyping of hybrid structures. Indium arsenide nanowires with epitaxial aluminium are produced to demonstrate the concept and are subsequently characterised in transport experiments.

# Preface

> *It's easy to play any musical instrument: all you have to do is touch the right key at the right time and the instrument will play itself.*
>
> Johann Sebastian Bach

*It's easy to build any quantum state: all you have to do is follow the right theory using the right materials and the state will build itself.*

21st century Bach


## Acknowledgements

Naturally, a project of this undertaking is not an entirely lonesome process. Everyone in the research group have contributed to this work in some way, be it either through experimental work, contribution of ideas, or by discussions. For this I am grateful. I would like to extend my appreciation to Dāgs Olšteins, who taught me all I ever wanted to know about cleanroom fabrication and electron beam lithography. Miķelis Marnauza, who divulged his secrets to beautiful SEM imaging. Thomas Kanne, a fountain of ideas, who taught me about the local MBE, involved me in the growth process, and showed me the beauty of bendy arrows in figure design. Joggerino E. Sestoft, who taught me about device design, the cryostat setup, and who was always available for discussion and great humor. Daniel Ross, who displays an inspiring commitment to his work and always sets a good mood in any situation. Daniel S. D. Kjær, who will hopefully continue measuring devices for a long time to come. Aske Gejl, great beard. Kasper Grove-Rasmussen, who was always on hand to answer my questions, willing to provide his technical expertise, and was always glad to discuss the newest data and ideas. Jesper Nygård, for the opportunity to undertake this work, for the advice, teaching, data discussions, talks along the way, and for gently nudging me to finish up the writing. Common to all of you is that you provide a great work environment, with enthusiasm, humor, and Thank you all for welcoming me into your cheerful group. I wish you the best of luck in the future. ᚠᚠᚠ

Mange tak til jer, som bidrog, lo, og gjorde arbejdet fornøjende.

# Contents

# Abbreviations

**2DEG** 2-Dimensional Electron Gas.

**ABS** Andreev Bound States.

**EBL** Electron beam lithography.

**EBLS** Electron beam lithography shots.

**IPA** Isopropanol (propan-2-ol).

**KNW** Kinking nanowire.

**MBE** Molecular Beam Epitaxy.

**MDC** Metal Deposition Chamber.

**MIBK** Methyl isobutyl ketone (4-methylpentan-2-one).

**OLAP** Objective lens aperture.

**PMMA** Poly(methyl methacrylate) (poly(methyl 2-methylpropenoate)).

**QPC** Quantum Point Contact.

**SEM** Scanning electron microscopy.

**TNW** Target nanowire.

**VLS** Vapour-Liquid-Solid.

# List of Publications

Contributions to papers made during the production of this work. Data or concepts from two papers are included in this document, and one paper has been excluded due to time constraints.

## Manuscripts with data/concepts included in this document

I Thomas Kanne, Dāgs Olšteinss, Miķelis Marnauza, Alexandros Vekris, Juan Carlos Estrada Saldaña, Sara Loric, Rasmus D. Schlosser, Daniel Ross, Szabolcs Csonka, Kasper Grove-Rasmussen, Jesper Nygård *Double nanowires for hybrid quantum devices* (submitted); preprint: arXiv:2103.13938 [cond-mat.mes-hall]

II Miķelis Marnauza, Dāgs Olšteins, Thomas Kanne, Joachim E. Sestoft, Rasmus D. Schlosser, Daniel Ross, Daniel Kjær, Aske N. Gejl, Jesper Nygård *From hybrid wires to hybrid devices: etch or shadow?* (manuscript in preparation)

## Manuscripts not included in this document

I Joachim E. Sestoft, Aske N. Gejl, Thomas Kanne, Rasmus D. Schlosser, Daniel Ross, Daniel Kjær, Kasper Grove-Rasmussen, and Jesper Nygåard *Scalable Platform for Nanocrystal-based Quantum Electronics* (manuscript in preparation)

# 1 Introduction

Semiconductor nanowires (NWs) are crystal structures with a diameter on the order of 100 nanometers, but which can extend several micrometers in height.

The spatial confinement in the radial direction, coupled with the high aspect ratio resulting from their considerable length, makes NWs a quasi-1-dimensional material. When coupled with superconductor materials made by evaporating the superconductor element onto the NW, they constitute a hybrid material. Because the base NW is a semiconductor, they inherit a gate tunable charge density, and this property is maintained in the hybrid material as well.[1,2] This puts them at the heart of current proposals for the realisation of qubit relevant systems, which require semiconductor-superconductor hybrid materials strongly confined to a 1-dimensional space.[3–9] Of fundamental interest to these systems is the Josephson Junction (JJ); two superconductors coupled by a weak link (e.g. a semiconductor channel), that through Andreev reflection can give rise to bound states, located within the superconducting gap. Named Andreev Bound States (ABS), they are proposed as a path to new qubit systems when they can be manipulated in a coherent manner,[2,7,10] and they are the basis for the formation of zero-energy Majorana Bound States (MBS).[7,11,12]

Common to all these proposals is the need for hybrid structures that exhibit ballistic or quasi ballistic transport. This sets a high standard for the quality of the materials, as disorder inherently leads to scattering, and the loss of ballistic behaviour.[2,13,14]

Epitaxial growth of aluminium (Al) thin-films onto indium arsenide (InAs) NWs has proven to create a hybrid structure with an interface that is practically disorder free,[15] leading to superior transport properties compared to materials formed by conventional evaporation techniques.[16] The number of publications involving InAs/Al NWs has rapidly increased in recent years, and epitaxial Al is at the forefront, as the primary superconductor material in combination with InAs.[17] However, ballistic transport in InAs has proven a challenge, disorder is a common problem that results in the unintentional formation of quantum dots.[18]

Devices are usually created by chemically etching away part of the superconductor film to form gate tunable region; a junction. However, while Al is relatively stable, and does not appear to be overly sensitive to processing, nor exposure to ambient conditions,[19] there is growing concern, that chemical processing introduces unintended disorder in the system.[15,16,18,20]

In the last few years, new schemes have been developed for the creation junctions formed by a patterned deposition of the superconductor onto the NW, performed without breaking ultra-high vacuum.[21] The concept was pioneered with the use of additional neighbouring NWs to block the path of the evaporated material,[22,23] effectively creating a *shadow* on the untouched, bare section of the target NW. This shadow deposition yields a material that is not exposed to chemical processing at any point in the fabrication process, thus gaining the full benefit of the epitaxial growth.

Hybrid InAs/Al NWs formed by shadow deposition are specifically included in the current proposal for Andreev qubits.[1,9,14] These qubit architectures require InAs NWs based JJs that exhibit ballistic electron transport, with near perfect transmission,[2] and it is expected that the method to achieve this, is by the creation of resistless junctions; that is, junctions formed without chemical processing of the NW.[14]

In this work, the concept of shadow deposition is expanded upon, in order to create designer InAs/Al NW architectures, including shadow Josephson Junctions. Effort is given to understand the necessary control parameters that allow for extensive possibilities in design of hybrid structures. The concept is also used in a double-evaporation scheme which allows in-situ deposition of Au leads onto a Pb thin-flm without breaking vacuum.

InAs/Al NWs, created with the shadow patterning method, are characterised in electron transport measurements in the normal (nonsuperconducting) regime. Here, ballistic transport is distinguished by quantisation of conductance, and this makes the Quantum Point Contact (QPC) useful as a reference model for an idealised, ballistic 1-dimensional channel.[24]

## Thesis outline

Chapter 2 begins with an introduction to the principles of nanowire fabrication using the vapour-liquid-solid mechanism, and electron beam lithography as a method to design the nanowire growth. This is followed by a brief summary of some basic points related to the use of the QPC as a reference model for a ballistic conduction channel, and the influence of a magnetic field on the transport measurements.

Chapter 3 describes the electrical setup used for transport measurements. This is supplemented with considerations on tuning of the setup to minimise noise in the data.

Chapter 4 contains the specifics of preparing the growth substrate for nanowire fabrication. This acts as a protocol for general substrate processing that was used in this work. This chapter also describes experimental results that are used to understand the control parameters that can be tuned to yield precise nanowires.

Chapter 5 introduces the principles of shadow patterning. Here, the necessary equations for fine control of the process are described. This is followed by a description of selected design patterns to yield variations of superconductor-semiconductor-superconductor junctions, and the experimental realisation of these designs. The chapter ends with a design scheme for the in-situ contacting of an epitaxial lead (Pb) layer of lead to gold (Au), followed by its experimental realisation.

Chapter 6 will describe electron transport results for selected InAs/Al shadow junctions, performed in the normal state with, and without the application of a magnetic field.

Chapter 7 concludes this thesis and describes potential next steps for future work.

Supplementary data from the experiments is compiled in the appendix.

# 2 Theoretical Background

This chapter introduces the principles of nanowire fabrication using the vapour-liquid-solid mechanism, and electron beam lithography as a method to design the nanowire growth. This is followed by a brief summary of some basic points related to the use of the QPC as a reference model for a ballistic conduction channel, and the influence of a magnetic field on the transport measurements.

## 2.1 Nanowire Fabrication

Fabrication of nanowires is a delicate, multi-step process. This section will briefly describe the two major components in the process, the Vapour-Liquid-Solid mechanism of growth and electron beam lithography, necessary for the design of advanced architectures. A later chapter will describe the general fabrication methods, and some of the necessary parameters for precision designs.

### 2.1.1 Vapour-Liquid-Solid growth

InAs nanowires used in this work are grown using an Au-catalysed, vapour-liquid-solid (VLS) method; specifically using a molecular beam epitaxy (MBE) system. The MBE chamber is under high vacuum ($\sim 2 \cdot 10^{-10}$ Torr), necessary for high purity growth. Here, selected materials undergo sublimation in an effusion cell, and are projected as a directed beam of gas phase matter. InAs NWs are grown using an InAs substrate with crystal orientation (111), that has been seeded with Au particles, acting as a catalyst for the growth. During growth, the sample is heated and the Au particle adopts a droplet shape. The sample is then exposed to In and As, which diffuse around the surface of the substrate, finding an energy minimum in the liquid state of the Au droplet. When the droplet reaches a critical saturation point, the In and As will find

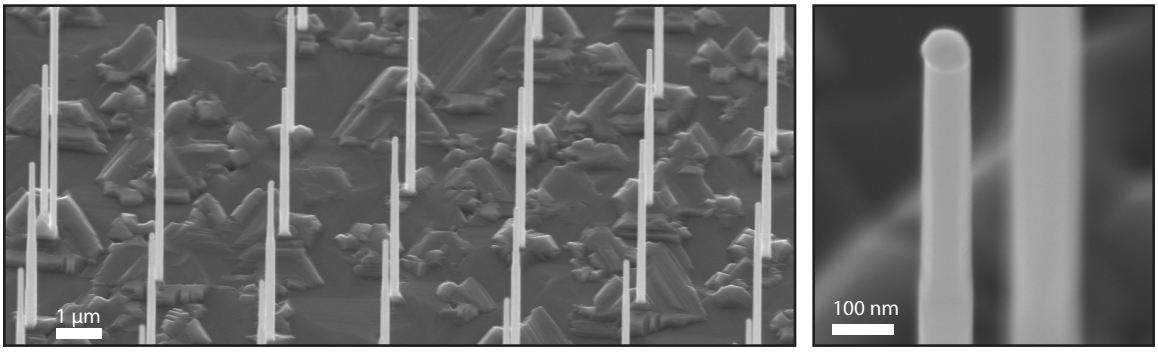


**Figure 2.1:** Scanning electron microscopy image of an array of nanowires grown with molecular beam epitaxy. Right panel: a close-up of the top of a nanowire from the same array, with the Au catalyst visible on the top of the wire.

a new energy minimum by precipitating as an InAs crystal at the liquid-solid interface between the droplet and the substrate, where the crystallographic orientation of the substrate promotes an ordered direction of the crystal growth. The Au seed particle remains on top, so as vapour phase atoms are continuously provided, the growth continues, creating the elongated structures. The size of the Au particle has a direct influence on the finished NW dimensions;[25] a small Au droplet will form a small foundation for the InAs solid state, and thus the structures grow thin, but tall. Large sized Au droplets result in thicker, but shorter NWs. The dimensions are ultimately decided by the growth parameters, the growth rate and time.[26]

Arrays of nanowires (as shown in Fig. 2.1), or more specific patterns can be achieved by selectively depositing Au particles in pre-specified locations. In this work, this is achieved via carefully processed growth substrates.

### 2.1.2 Electron Beam Lithography

The pattern for Au particle placement, and thus NW growth must be precisely defined if the aim is to yield complex nanostructures. Defining the sites for Au catalyst particles is performed using electron beam lithography (EBL), and this section will briefly summarise the main principles used to create the design patterns which will be presented later.

EBL is a method for patterning an electron sensitive resist with a directed electron beam. Unlike conventional photolithography using UV light, the significantly smaller wavelength of electrons makes EBL a high precision instrument. The operation is analogous to the principles used in scanning electron microscopy (SEM); an electron source emits electrons that are accelerated to 100 keV by an electron gun,[i] and travel through a set of condenser lenses and magnetic coils to focus and shape the beam, before it goes through an objective lens that focuses the beam spot size onto the stage. The spot size can be adjusted using the objective lens aperture (OLAP), and the beam current. The patterns created in this work were consistently made using a beam current of 500 pA, and an OLAP of 40 µm, for a beam spot diameter of 2.7 nm.

The electron beam energy modifies the structural integrity of the exposed resist. The electron sensitive resist used is a poly(methyl methacrylate) (PMMA), a so called positive resist, because exposure to the electron energies breaks the chemical bonds of the resist, leaving it vulnerable to etching by a chemical developer.[ii] Penetration depth of electrons into the sample depend on the acceleration voltage used for the electron emission, and will affect the amount of backscattered electrons that re-enter the resist area. Backscattered electrons can travel several micrometers in the resist,[27] and this becomes an issue when producing nanowire arrays, and especially if the arrays have complex architectures. Also, the generation event probability of secondary electrons is inversely proportional to the primary beam energy,[28] so for precision designs, a large acceleration voltage should be chosen to eliminate unintended modification of the area surrounding the design pattern.

As mentioned in the previous section, the dimensions of the finished nanowires are linked to the dimensions of the Au catalyst particle. With a beam spot of 2.7 nm, a single dot, or electon bream lithography *shot* (EBLS), defined by a short pulse of the electron beam is used to define the smallest Au catalyst sites; and thus yield the thinnest, and longest NWs. Larger Au catalyst sites are defined by placing multiple shots spaced by 20 nm. Fig. 2.2 shows a selection

[i] System dependent. 100 keV for the system used in this work.

[ii] The reverse case is a negative resist, which hardens with exposure due cross-linking of the molecules.

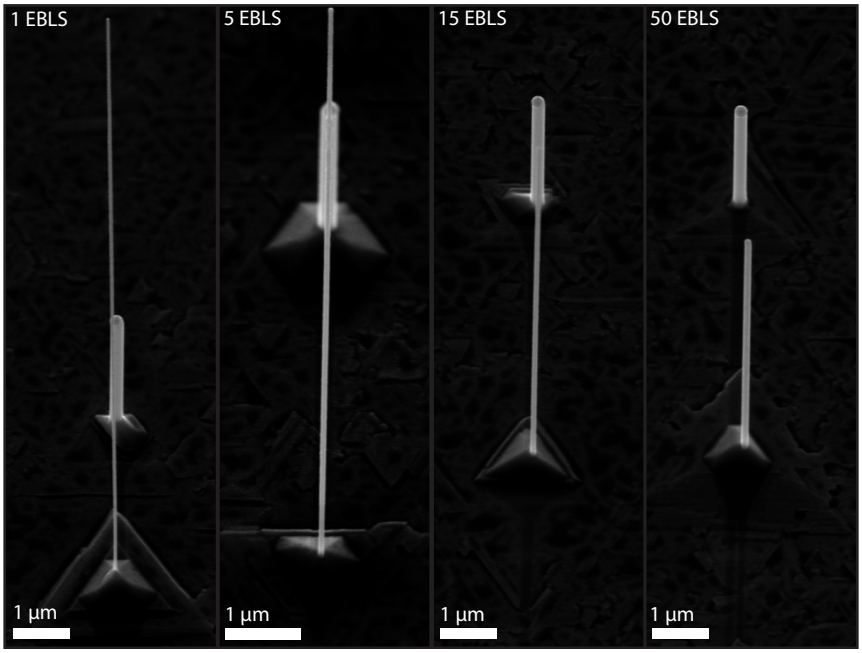


**Figure 2.2:** Nanowires created from electron beam lithography shots of 1, 5, 15, and 50. The thicker structure in the back is a nanowire created from 150 shots.

of nanowires that were grown from patterns of 1, 5, 15, and 50 EBLS, they are contrasted against a 150 EBLS nanowire in the background.

## 2.2 The Quantum Point Contact

The transport experiments in this work are primarily focused on the exhibition of quantum point contact behaviour in nanowires. It is therefore useful to shortly summarise some key points, that will aid our discussion of the data to come.

The Quantum Point Contact (QPC) is a fundamental and widely studied system. In its simplest description, the QPC consists of two electron reservoirs connected by a constriction narrow enough to approximate a 1-dimensional system (sketched in Fig. 2.3a). The confinement of electrons entering the constriction leads to a parabolic dispersion relation with distinct sub-bands, which in turn results in quantisation of conductance. For quantised states along a 1D wire, the energy dispersion for the $n$th mode $E_n$ is given by

$$E_n(k_x) = E_n + \frac{\hbar^2 k_x^2}{2m^*} \tag{2.1}$$

where $m^*$ is the effective mass of the electron, and $k_x$ is the wavenumber of states travelling along the $x$ direction.

An external electric field, for example generated by a local capacitor (e.g. a gate) will raise or lower the chemical potential, effectively changing the Fermi energy $E_F$, decreasing or increasing the number of open channels. Applying a voltage between these reservoirs effectively shifts the energy at the leads, changing the Fermi-Dirac distribution of the electrons in the reservoirs.

Ideally, the reservoirs transmit electrons perfectly. In the adiabatic approach, the reservoirs are gradually decreased (or the confining potential increased) in a smooth manner until the potential forms a 1-dimensional constriction.

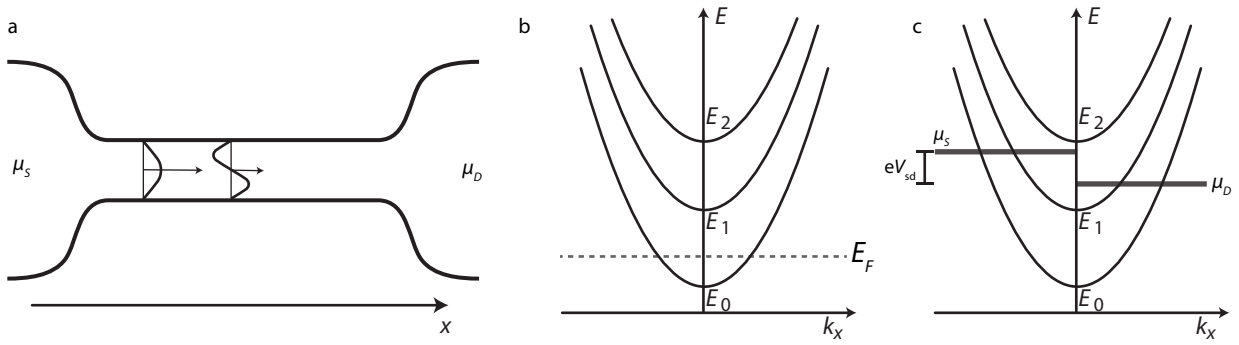


**Figure 2.3: a.** Sketched 1-dimensional constriction connecting two reservoirs; source and drain. Outside the constriction, transverse moving modes can propagate continuously, but within the constriction they are confined to defined energies, approximated by Eq. (2.1) in the ideal case. **b.** Energy dispersion relation (Eq. (2.1)) for electrons within the 1-dimensional confinement. Raising or lowering of the Fermi energy $E_F$, for example via an external electric field, increases or decreases the number of modes that can populate the constriction. **c.** An applied voltage sets the Fermi distributions of the two leads out of equilibrium; driving a finite current. Adapted from Ref. [29].

The transmission probability can then be somewhat tuned by the geometry of this potential. Such is usually the case for experimental QPCs formed in 2-dimensional electron gasses (2DEG), but for nanowires, where connecting the leads more or less resembles the stacking of LEGO bricks, the transmission and reflection amplitudes become less controllable. Nevertheless, an idealised model will be useful for discussion of the data that will be presented later.

### 2.2.1 Saddle point model as theoretical QPC

The saddle point model is an approximation of a 2-dimensional potential which, as the name suggests, assumes a smoothly curved potential, and is thus a variant of the adiabatic approach. It is a an analytical model that allows the transmission amplitudes to be separated into their coefficients $t_n$ for the $n$th modes. It assumes confinement in the $xy$ direction, and the potential of the constriction is given as[31]

$$V(x,y) = -\frac{1}{2}m^*\omega_x^2 x^2 + \frac{1}{2}m^*\omega_y^2 y^2 + V_0 \tag{2.2}$$

where $\omega$ is some factor to modify the parabolic curve of the potential, and $V_0$ is the potential at the center of the saddle. Fig. 2.4 shows an illustration of the assumed potential of Eq. (2.2). The energy in the $y$ direction is a harmonic oscillator

$$E_y = \hbar\omega_y(n + \frac{1}{2}) \, . \tag{2.3}$$

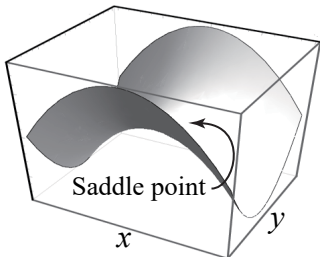


**Figure 2.4:** Idealised adiabatic QPC formed in a saddle point potential described by Eq. (2.2). Reprinted from Ref. [30].

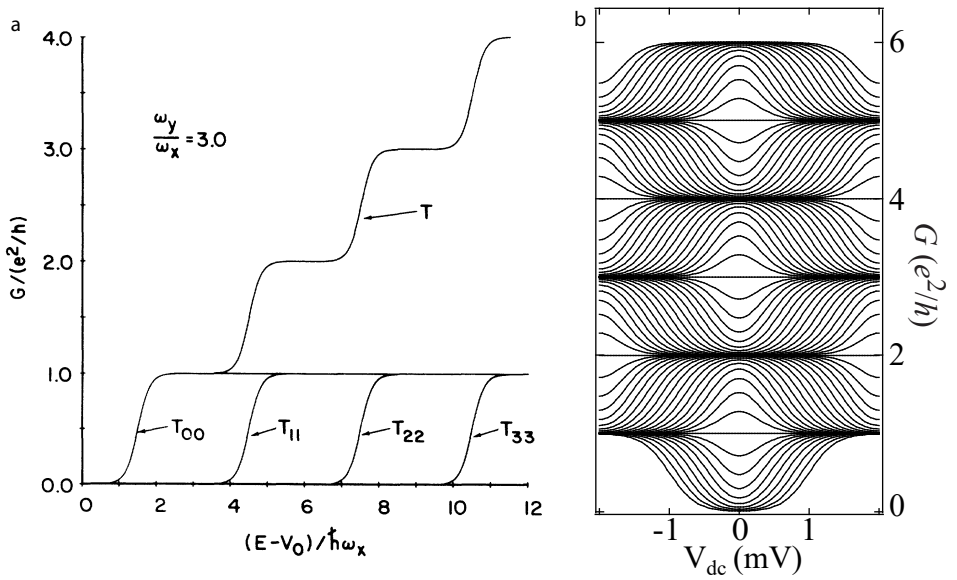


**Figure 2.5:** Idealised QPC formed by a saddle point potential. **a.** Conductance through the idealised QPC occurs only via single channel transmission, the total conductance is then the sum of all open channels. **b.** Bias spectrum as a function of the chemical potential $\mu$ and source-drain bias $V$ of an idealised saddle point model QPC.
Adapted from Ref. [31] (**a**) and Ref. [30] (**c**).

Considering then the potential in the $x$ direction, and inserting it into the 1-dimensional Schrödinger equation $\left(-\frac{\hbar^2}{2m^*}\partial_x^2 + V(x)\right)\psi(x) = E\psi(x)$, Büttiker showed that the transmission probabilities of the $n$th mode can be expressed as[31]

$$T_n = \frac{1}{1 + e^{-2\pi\epsilon_n}} \tag{2.4}$$

where the energy $\epsilon_n$ for the $n$th mode is given

$$\epsilon_n = \frac{E - \hbar\omega_y(m + \frac{1}{2}) - V_0}{\hbar\omega_x} \, . \tag{2.5}$$

The conductance through the QPC is then raised accordingly with the opening of a new channel, the total transmission being the sum of each open transmission mode. Fig. 2.5a shows the conductance through a saddle point QPC as individual transmission modes become available as the energy is increased.

In a 1D system, current takes the form

$$I = \frac{2e}{h}\sum_{n=1}^{N_m} = \int dE T_n(E)\left(f_L(E) - f_R(E)\right) \tag{2.6}$$

where $N_m$ is the number of transverse modes travelling through the system, and $f_L$ and $f_R$ are the Fermi distributions of the left and right leads, respectively.

Eq. (2.4) can be rewritten to express the energy $E$ explicitly,

$$T_n = \frac{1}{1 + \exp\left(-\frac{2\pi}{\hbar\omega_x}(E - \epsilon_n)\right)} \, . \tag{2.7}$$

If the transmission probability in Eq. (2.7) is used in Eq. (2.6), the differential conductance $G = \partial I/\partial V$ for small values of the bias voltage $V_{sd}$, $(f_L - f_R \approx 0)$

can be expressed[30,32]

$$G(\mu, V_{sd} \approx 0) = \frac{2e^2}{h} \sum_{n=1}^{N_m} 1/(1 + e^{-\frac{2\pi}{\hbar\omega_x}(\mu - \epsilon_n)}) \tag{2.8}$$

where $\mu$ is the chemical potential of the system. The conductance when $V_{sd} \neq 0$ can then be approximated as the average of two zero bias conductance measurements where the chemical potential of the zero-bias system is set to the chemical potential of simulated lead,[32,33]

$$G(\mu, V_{sd}) = aG(\mu_s, V_{sd} = 0) + (1 - a)G(\mu_d, V_{sd} = 0) \tag{2.9}$$

where $a = \frac{1}{2}$ has been found to fit adiabatic 1D systems,[32,34] so we may write

$$G(\mu, V_{sd}) = \frac{G(\mu_s, V_{sd} = 0) + G(\mu_d, V_{sd} = 0)}{2} \, . \tag{2.10}$$

For an energy $\epsilon_n$ that resides between the bias window, $\mu_d < \epsilon_n < \mu_s$, the difference between $G(\mu_s, V_{sd} = 0)$ and $G(\mu_d, V_{sd} = 0)$ is then exactly $2e^2/h$, so the averaged value becomes $e^2/h$. So it is possible to analytically simulate the conductance as a function of a bias voltage and gate voltage (we now assume that the Fermi energy changes proportionally with an applied electric field).

A simulated bias spectrum, based on the saddle point QPC at zero temperature is shown in Fig. 2.5b, also called a waterfall plot. Every line in the plot represents a $V_sd$ trace at a different gate voltage, with the lines ascending as the gate voltage is increased to more positive values. At zero bias, plateaus form at multiples of $2e^2/h$ which is seen as the bundling of lines at conductance values $G = 1G_0, 2G_0, 3G_0$, and half-plateaus (multiples of $e^2/h$) form in the finite bias regions.

### 2.2.2 In semiconducting nanowires

The strict geometrical confinement in nanowires and high aspect ratio resulting from their considerable length (Fig. 2.6) make them a quasi 1-dimensional material, which leads to quantisation of electron states traversing the wire, with an energy dispersion relation that somewhat mimics that of the idealised 1D system. Semiconducting nanowires inherit the properties of their constituent

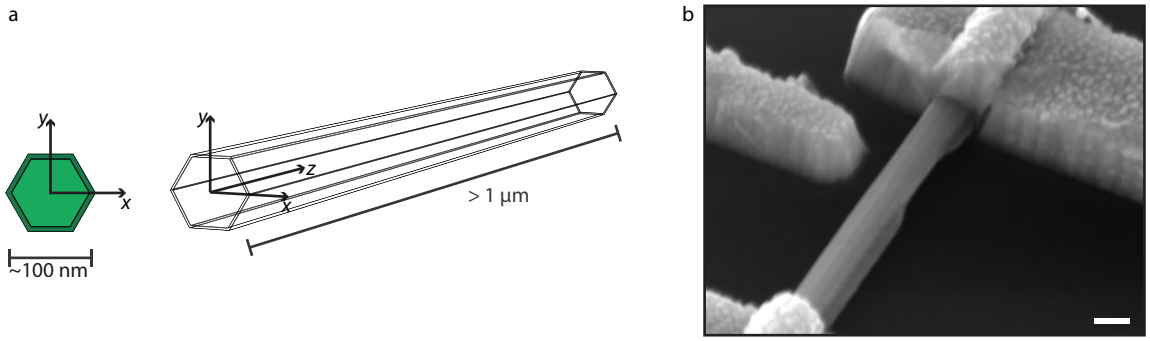


**Figure 2.6: a.** The high aspect ratio coupled with strong confinement in $xy$ makes for a quasi-1-dimensional channel. **b.** SEM image of an InAs nanowire connected to two Ti/Au leads (top and bottom) and positioned near a sidegate; the transition from reservoir to nanowire is far from adiabatic. A thin-film composed of Al is deposited on the nanowire, responsible for a junction opposite the sidegate. The scalebar represents 100 nm, but note that the image is taken at an angle of 40°, so the length scale along the nanowire is more than double of the scalebar.

material, allowing the gate tunable chemical potential to control the carrier density within the wire.

While these two points make semiconductor nanowires a candidate platform for ballistic transport and QPC-like behaviour, there are, however, some distinct characteristics that set nanowires apart from the idealised 1D wire and the smoothly walled potential of the 2DEG. The linked reservoirs are not adiabatically coupled to the nanowire; on the contrary, they usually consist of leads that are lithographically defined onto the nanowire, Fig. 2.6b shows a scanning electron microscopy image of a nanowire device connecting two leads of this type. Disorder at the interface between the leads and the nanowires will induce non-zero reflection probabilities that are not easily tuned, or rather impossible to get rid of. Charge impurities in the nanowire can lead to local potential differences, and such charge impurities may move around in the presence of a changing external electric- or magnetic field. If these elements lead to coherent backscattering in the wire, the transport properties are systematically changed.

## 2.3 Zeeman effect and effective $g$ factor

In an external magnetic field, the Zeeman energy splitting in the one-dimensional approximation is described by

$$\Delta E_z = g^* \mu_\mathrm{B} B \tag{2.11}$$

where $g^*$ is the effective $g$ factor and $\mu_\mathrm{B} = e\hbar/(2m_\mathrm{e})$ is the Bohr magneton. Fig. 2.7 shows a sketched example of the change in the energy dispersion relation for system with a single spin band subjected to a magnetic field. When the magnetic field is applied, the spin up and spin down bands separate by $g^*\mu_B B$ exactly. For a free particle $g^*_\mathrm{free} = g = 2$, but in condensed matter systems $g^*$ can be significantly different. As an example, the effective $g$ factor for bulk InAs is $\sim 15$.[35,36] Nanostructured hybrid systems offer many different experimentally derived values of $g^*$, as an example, the following values are all reported for InAs systems 4,[18] 5,[37] 6.5,[38] 8.5,[39] 20,[6,40] 23,[6] 50,[6] and field tunable values 2-18,[41] 8-22.[42] One speculated reason for an apparently high $g^*$ for hybrid InAs/Al systems is the possible enhancement of a local magnetic field in the NW, as a result of repulsion of the magnetic field from the Al superconducting thin film, resulting in local magnetic fields higher than the intended, applied field.[40] A numerical study on nanostructured InAs by Gawarecki and Zieliński[43] has shown that the effective $g$ factor is heavily localisation dependent, with a continuum bulk approxmiation of InAs reporting a $k$-space dependent range

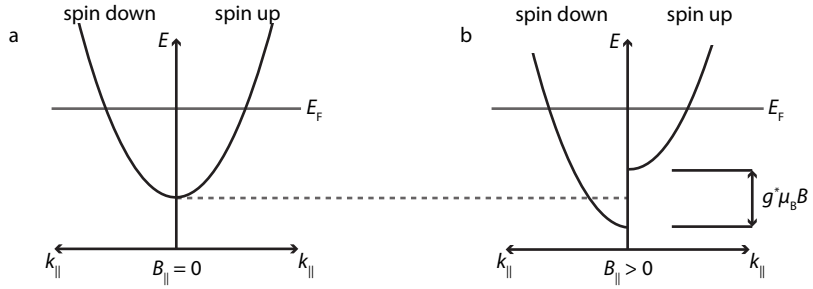


**Figure 2.7:** Change in a single spin band system by a parallel magnetic field in the absence of other spin altering effects. **a.** Equilibrium state of the system as $B = 0$. **b.** At $B > 0$, the spin up and spin down components are separated by exactly $g^*\mu_\mathrm{B}B$.

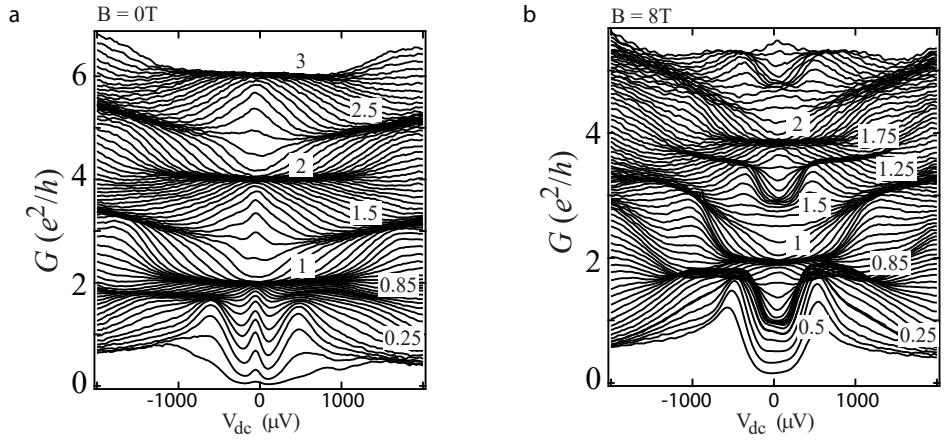


**Figure 2.8:** Bias spectroscopy of a quantum point contact with and without Zeeman energy splitting. **a.** Magnetic field $B = 0$. Conductance quantisation is seen as the formation of $2e^2/h$ plateaus in the zero bias regime and $e^2/h$ plateaus in the finite bias regime. **.** A large magnetic field $B = 8$ T splits the sub bands causing distinct half plateau formation in the zero bias regime, and further splits the finite bias half plateaus into quarter plateaus. The annotated values represent values of $2e^2/h$. Reprinted from Ref. [30]

$g^*_{\mathrm{InAs}} = [-14, 2]$ with $|g^*|(k = 0) \sim 14$ and $g^*(k \to \infty) \to 2$. Numerical calculations of box sized, ideally impurity- and fault free nanostructured InAs, using a tight binding approximation[i] as well as $\boldsymbol{k}\cdot\boldsymbol{p}$ pertubation theory[ii] suggests that the effective $g$ factor for the conduction band should approach 2 as the box size is decreased towards zero, and decay towards $\sim 14$ as the size was increased up to at least 120 nm.[43] It has been shown that, at least for III-V and II-VI semiconductor nanostructures, $g^*$ can be described by a combination of two constituent $g$ factors; a bulk term (which is band gap dependent) and a surface geometry dependent term, which makes only a minor contribution, and does not explain the broad range of experimentally reported values.[44]

The effect of Zeeman energy splitting can be seen in the bias spectrum of conductance quantised devices. Fig. 2.8 shows such an example; without a magnetic field (Fig. 2.8a), the bias spectrum shows conductance quantisation as the formation of plateaus at integer $G_0$ in the zero bias regime, and half-plateau formation in finite bias. An applied field splits the sub bands, creating half plateaus in the zero bias regime; the half plateaus in finite bias regime are further split.

[i] We have not defined *tight binding* in this work, and we will not go further than this description: the approximation of electrons being tightly confined to their host atoms, similar to how atomic orbitals are commonly modeled.

[ii] Again, we will not go into exact details of *what* this theory says, but describe it as a rewriting of the Schrödringer equation for solids with a periodic potential, based on the Bloch function $\psi(r) = e^{i\mathbf{k}\cdot r}\mu(r)$, in a way that allows the crystal periodic potential $\mu$, wavevector $\boldsymbol{k}$, the band number, and the momentum operator $\boldsymbol{p}$ to take part in its description.

# 3 Methods for Transport Experiments

## 3.1 Electrical Setup

This section explains the electrical setup used in this work. All transport data was measuring in a 2-terminal configuration. A 4-terminal approach was unfortunately not feasible since the functional devices did not have four separate working contacts.

Fig. 3.1 shows a diagram of the setup. An AC bias signal is produced by the lock-in amplifier and a DC signal is produced by a digital-to-analogue converter (DAC), and both signals are passed through a voltage divider, where the AC signal is reduced by a factor 10,000, and the DC signal reduced by a factor 1000. The mixed signal enters the dilution refrigerator (cryostat) that contains a set of series resistors and low pass filters, and is connected to one of the leads on the sample. The sample is grounded by a connection out of the cryostat that passes through an I-V converter (or "current amplifier") which reads the current and outputs a proportional voltage signal. The AC component of the signal is read with the lock-in amplifier, and the DC component is read by a digital multimeter (DMM). Several channels from the DAC can be used to supply voltage to the gates on the sample. In this project, this always consisted of a backgate, and at least one secondary sidegates.

The dilution refrigerator used in this work is a cryofree unit, cooled by mixing liquid $^3$He and $^4$He, allowing the mounted sample to reach millikelvin temperatures. A two-axis vector magnet is fitted inside the main chamber, able to reach magnetic fields of 8.5 T in one direction, and 3 T in another direction.

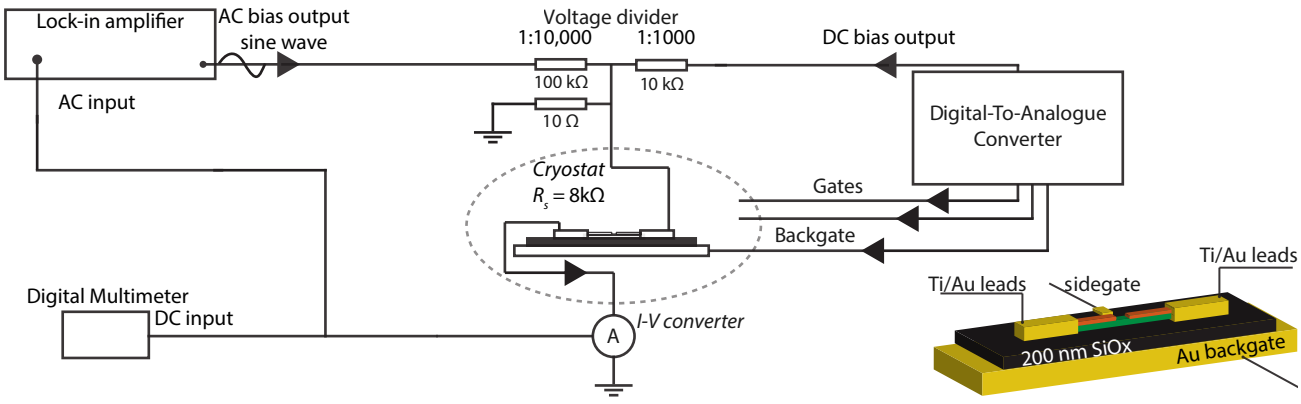


**Figure 3.1:** General setup for the measurements performed on devices presented in this work. Inset: schematic of a device based on a nanowire (green) with a single junction formed by two evaporated metals (orange); placed on a Si chip with electron beam lithography defined leads and a gate, a large gold plate underneath the chip acts as the backgate.

The low temperature is a prerequisite for measuring quantum transport, as the thermal energy at room temperature greatly exceeds the energy scales where the relevant phenomena occur. The next sections will deal with some considerations on the thermal energy, the excitation voltage, and the frequency selection of the AC bias signal. Finally, some notes on efforts to reduce noise at the cost of measurement time are presented.

### 3.1.1 AC-bias amplitude selection and data resolution

The amplitude of the output wave from the lock-in amplifier is directly proportional to the excitation voltage of the electrons, and should not be too large in order to stay in the linear response regime. In practice, the excitation voltage should ideally match the thermal excitation in order to maximise the signal. The derivative of the Fermi distribution produces a Gaussian with FWHM of exactly $3.5k_{\mathrm{B}}T$, and we refer to this as the thermal broadening of the Fermi function. Thus, we can determine an appropriate wave amplitude that matches the thermal excitation, or indeed we may deliberately choose a higher wave amplitude to *simulate* a broadening of the Fermi distribution. In the relevant setup, the reported amplitude value is 2.8 times the root-mean-square of the output wave, the appropriate excitation voltage can thus be calculated as $V_{\mathrm{excitation}} = 3.5k_{\mathrm{B}}T/2.8$. While there may be some reasons one might want to exceed the thermal broadening, there is no reason to select an excitation voltage below the thermal excitation. The bias range of the output wave (the width of the voltage domain that is probed) is directly proportional to the excitation voltage, so when stepping the bias voltage, the number of steps required to achieve full resolution can be calculated via the inverse proportionality

$$n_{\mathrm{sd}} = \frac{V_{\mathrm{sd,\ range}}}{V_{\mathrm{excitation}}} \tag{3.1}$$

and any smaller step size will just provide some amount of repeat measurements within the same excitation area.[i] We can see how an increase in temperature dramatically alters our measurement time, take for example a standard source-drain bias measurement performed a 30 mK, and increase the temperature to 2 K; the increase in thermal excitation is $2/0.03 \approx 67$ and the number of steps to probe the same energy space is reduced by the same factor. For a source-drain bias measurement it is a reduction of thousands of steps to hundreds, which is not much in terms of time; but for bias-spectroscopy where the chemical potential, controlled by a gate voltage, needs to be probed in some detail, we have $n_\mu n_{sd}$ steps and reducing $n_{sd}$ can reduce the acquisition time by several hours.

### 3.1.2 Frequency tuning

The frequency output wave from the lock-in amplifier should ideally be tuned for every setup. Repeatedly measuring the conductance as a function of the lock-in amplifier frequency should yield fluctuating values at frequencies that are multiples of specific harmonics.[ii] Such fluctuations are undesirable, indeed they are the antithesis to the purpose of the lock-in amplifier, so a frequency that produces the most consistent measurement should be selected. In practice this

[i] i.e. small effects that occur in a smaller voltage bias range will be smeared and are unlikely to stand out.

[ii] Such as those corresponding to the oscillations of the alternating current provided by the main power net. These harmonics could originate from electronic lab equipment in the vicinity.

means measuring a wide frequency domain, selecting an appropriate sub-domain, and performing a detailed analysis of the area.

The method for selecting the *best* frequency seems to be a matter of taste among experimentalists, but quantifying it by smallest variance between repeat measurements is an obvious choice. As an example of such tuning, Fig. 3.2 shows data produced during tuning of a device that will be presented in a later section. Fig. 3.2a and b shows the conductance measured as a function of lock-in frequency in the domain range [30 Hz, 300 Hz], repeated 20 times. It has been colour coded by the normalised residual to the mean value as a function of the frequency. There are two areas where variance appears low (the region around 115 Hz and 180 Hz). It is relevant to consider if applying an electric field (for example via a gate voltage) can affect the fluctuation. Therefore, the measurements were redone with a finite gate voltage set near the upper boundary of the gate space of interest (Fig. 3.2b). From inspection it was decided to exclude the lower of the frequency ranges, though the increase in variance is marginal for both regions. Fig. 3.2c shows the summed residuals to the mean of the broad sweeps shown in panels a and b, here it becomes more clear that there are some minimal variations around the lock-in frequency 180 Hz Fig. 3.2d, and e shows fine sweeps near the optimal frequency and Fig. 3.2f shows the summed residuals of the fine detail sweep in panel e; the optimal frequency appears to lie around 183.5 Hz.

### 3.1.3 Digital Multimeter and Number of Power Line Cycles

Periodic AC noise infesting the DC signal can be reduced by integrating the DC signal over a set amount of power line cycles. The power line frequency of the DMM is 50 Hz, so one cycle requires 20 milliseconds, thus increasing the number of power line cycles necessarily increases the acquisition time. Fig. 3.3a shows three similar measurements with the DMM NPLC set to 0.2, 1, and 10. Since the acquisition time scales directly with the NPLC set points, the benefits of setting NPLC = 10 is outweighed by the time bottlenecking, while the quality difference between NPLC = 0.2 or NPLC = 1 sees too small a noise reduction to make the five-fold increase in acquisition time feasible.

### 3.1.4 Time constant and signal fluctuations

The lock-in time constant controls the response to changes in the input signal (measured). Any data points recorded within the period of the time constant will correspond to the same measured signal, it is therefore unnecessary to record data quicker than the time constant, and perhaps even *wrong*, as the recorded data may give an impression of a non-fluctuating signal, which would otherwise have been revealed by a low time constant. Recording data slower than the time constant is in principle not wrong, but introduces the mentioned fluctuations, which could be interpreted as instability of the signal. In the setup relevant to this work, the instrument has a settle time which controls the time period after a new data point has been recorded before the next data point is acquired. The appropriate settle time is the difference between the acquisition time and the time constant on the lock-in amplifier. While a high time constant provides a clean looking signal, the trade off is a large settle time. As an example, Fig. 3.3b shows three measurements of the source/drain bias for a device in a noisy setting where we vary the time constant and have adjusted the settle time appropriately. The signal with a time constant of 3 second is very tolerable, but the trade off was a total acquisition time of 9 minutes. Not a problem for a

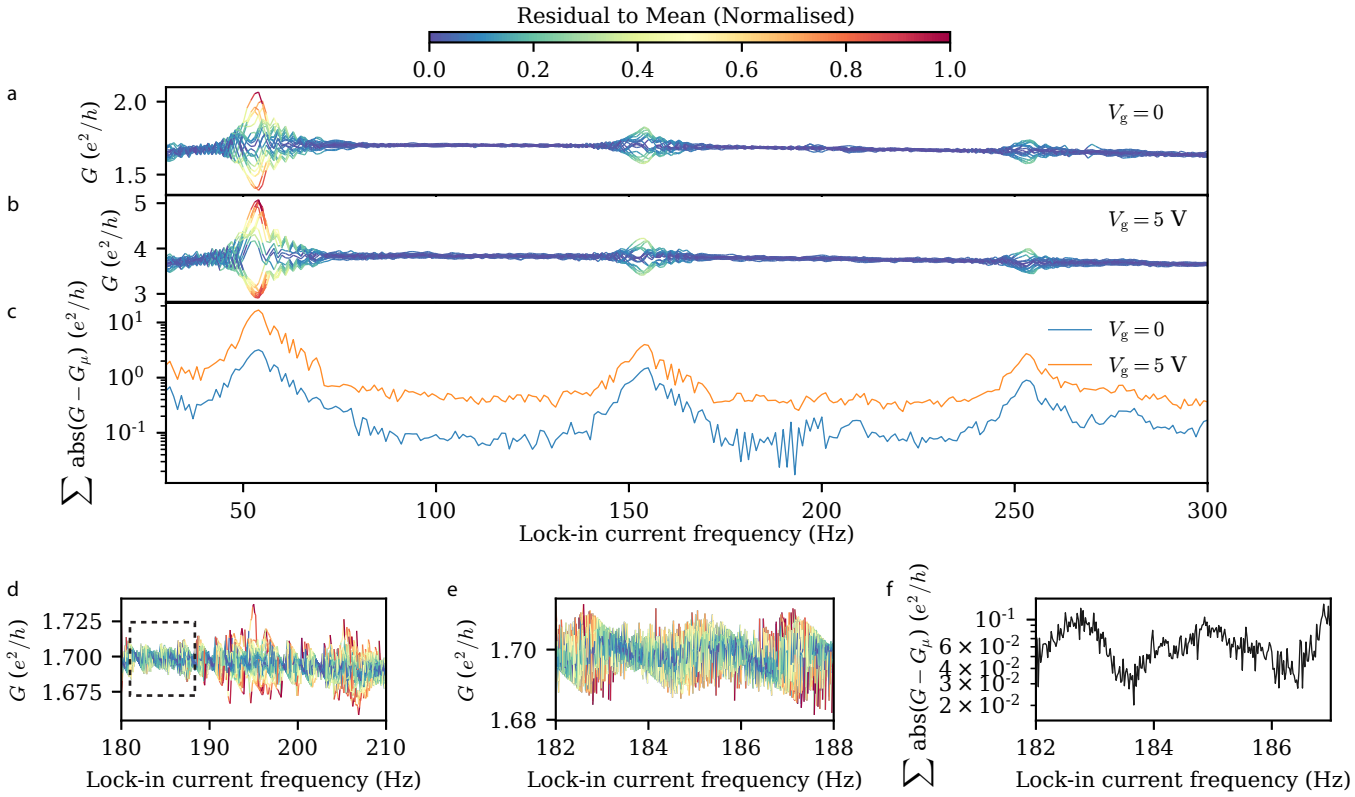


**Figure 3.2: Lock-in amplifier frequency selection. a.** and **b.** The conductance of a device is measured as a function of the current frequency on the lock-in amplifier, with and without an applied electric field. Each frequency sweep is repeated 20 times. Line segment colours represent the calculated residual to the mean conductance $G_\mu$ as measured at each specific frequency for the 20 repeat measurements. **c.** The summed absolute residual to the mean of the 20 repeat measurements at each specific frequency. **d.** Fine sweeps in the [180, 210] Hz range without applied electric field. Dashed line indicate a candidate region. **e.** Fine sweep in the region indicated by dashed lines in **d**. **f.** Summed absolute residual to the mean of the 20 repeat measurements shown in **e**. From **a**, initially two areas are of interest, low noise regions at ranges [100, 120] Hz and [180, 210] Hz. Applying an electric field to *open* the device introduces a marginally higher variance to the [100, 120] Hz range, with a relatively lower increase in the [180, 210] Hz range. It is debatable if one can pick up a difference at all, but we may use the summed residuals shown in **c** to pick out the area with the lowest residual sum. In **f**, we have two areas that are comparable; one could argue that the optimal frequency lies around ∼183.5 Hz as the residual fluctuates less at the immediate neighbouring frequencies.

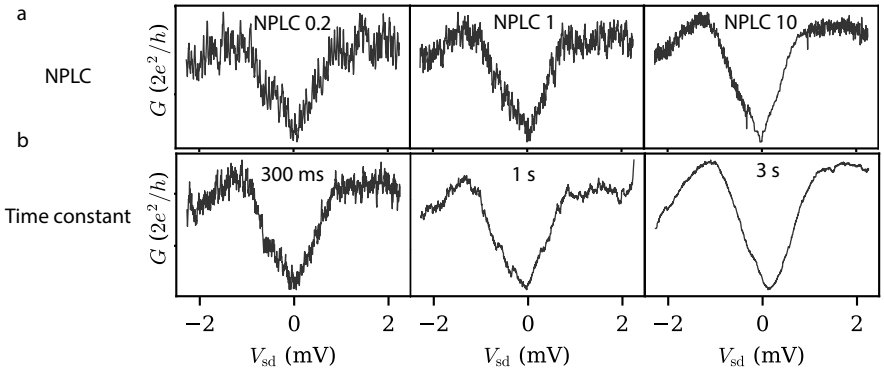


**Figure 3.3: a.** Variation of the NPLC setting for three similar measurements performed in succession. **b.** Variation of the time constant for three similar measurements (with NPLC = 0.2) performed in succession.

single trace, but for multidimensional data this quickly becomes a bottleneck as the complete acquisition time increases exponentially with dimensionality. The total acquisition time for a $d$-dimensional data set can be roughly calculated as $t = \tau \prod_{i=1}^{d}(n_i)$, where $\tau$ is the acquisition time per data point, and $n = (n_1, n_2, ..., n_d)$ is the desired number of steps for each individual parameter. For the specific example given above, if we wanted to probe the source/drain bias as a function of gate voltage we might conservatively choose a gate voltage resolution of 200 data points, for a total acquisition time of 10 to 30 hours depending on the time constant.

# 4 Fabrication Methods

This chapter contains the specifics of preparing the growth substrate for nanowire fabrication. This acts as a protocol for general substrate processing that was used in this work. This chapter also describes experimental results that are used to understand the control parameters that can be tuned to yield precise nanowires. The VLS growth performed in a molecular beam epitaxy system was done by Thomas Kanne.

## 4.1 General procedure for substrate processing

This section will describe the cleanroom fabrication steps taken to fabricate a patterned growth substrate. The VLS growth procedure of nanowires in this work was performed by Thomas Kanne.

### Spincoating

The wafers used in this work are InAs <111>B wafers. The following steps are performed as rapidly as possible to minimize pollution of the substrate. First, to eliminate any unwanted residue or dust that may be present on the wafer after unpacking, the wafer is ashed for 60 seconds in a plasma asher. Before spincoating the wafer is preheated on a hotplate for 2 minutes at 185 C°, as this is expected to increase resist flow, increasing the resist homogeneity. During the preheating, a glass beaker can be placed over the wafer to reduce the chance of settling of airborne dust particles. Once heated, the wafer is spincoated with PMMA resist EL6 at 4000 RPM for 45 seconds, then baked for 2 minutes at 185 C°, hardening the resist. After baking, a second layer of PMMA resist A2, is deposited in the same manner as before and baked once again for 2 minutes at 185 C°. The two baking steps, called a *softbake*, are performed to evaporate the solvent from the resist film, which reduces the thin film thickness, and hardens the resist, increasing the mechanical stability. During the spinning process, one should inspect the wafer/resist for imperfections by eye, as any dust particles that may have settled during one of the previous steps may lead to uneven resist, which in turn may lead to local over- or underexposure during the lithography process. Major dust particles will produce clearly visible streaks in the resist where the distribution is locally blocked. In the event that the resulting resist is of low quality, the wafer can be cleaned by transferring it to a beaker containing a solvent suitable for removal of the resists (acetone for EL6 and A2), then washed with MQ water, dried with nitrogen gas, and ashed once again.

### Electron Beam Lithography

Electron beam lithography was performed with an Elionix ELS-F100 100 kV electron beam lithography system. The beam diameter used for defining the Au

catalyst seed area was approximately 2.7 nm; using a beam current to 500 pA, and OLAP 40 µm.

### Development

After the EBL exposure the sample is developed in a 1:3 ratio solution of 4-methylpentan-2-one (MIBK) for 60 seconds, followed by a rinse in propan-2-ol (IPA) for 30 seconds, and then a rinse in milli-Q water (MQ) for 30 seconds. The sample is then blow dried with $N_2$, and ashed for 60 seconds. MIBK etches the exposed resist, but leaves the unexposed areas intact, thus forming well defined areas where the pure wafer is exposed.

### Metal depostion of growth catalyst particles

Following development, the substrate now has defined patterns for Au seed particles. Au is evaporated onto the sample in a Metal Deposition Chamber (MDC). When the unexposed resist is later removed, the Au layer on top will be removed with it, but the Au in the exposed patterns will remain.

Prior to metal deposition, the sample is cleansed in a hydrofluoric acid (HF) solution consisting of 33.8 - 35.8% $NH_4F$ and 6.2 - 6.6% HF for 30 seconds, followed by a rinse with MQ, and then blow drying with $N_2$. The HF cleanse serves to clean the surface, remove any oxide that has formed on the surface, but also passivate the surface, reducing the formation of new oxide on the exposed substrate. The sample is promptly transferred to a metal deposition chamber where it is put in ultra high vacuum.

All samples in this work have been processed in the AJA Orion thin-film deposition and milling system. The instrument allows for ultra-high vacuum ( $10^{-9}$ Torr) A region of material to be evaporated is heated with an electron beam, until the material evaporates at a constant rate. A monitoring crystal in the chamber is used to evaluate the evaporation rate, and this is used to calculate thickness of the metal film. Once a desirable evaporation rate has been reached, the shutter is opened, allowing the evaporated material to pass onto the sample, where it forms a film. Once the desirable thin film thickness has been reached, the shutter is closed again, and the voltage driving the electron beam is ramped down. The evaporation rate used was roughly 1 Å/s. Typically, 20 nm Au was deposited for NW growth.

### Liftoff

After metal deposition, the sample is transferred to acetone, which dissolves the remaining resist, lifting the Au layer that is not in contact with the substrate. To promote liftoff, the acetone is warmed to 50 C°before the wafer is dipped into the solution, and liftoff effectiveness can be increased further by using a pipette to create a turbulent flow over the sample. Typically, a second container of warmed acetone will have been prepared, and the sample is transferred to this container and stored overnight to remove any unseen, excess resist that has not come off. When liftoff is complete, the sample is rinsed in MQ for 30 seconds, blow dried with $N_2$ and ashed for 60 seconds.

### Molecular Beam Epitaxy

In preparation for growth in the MBE, the sample is dipped in HF again for 20 seconds to cleanse the surface. The prepared sample is then transferred to the MBE chamber where it will undergo growth. The MBE chamber is connected to a metal deposition chamber via a vacuum setup so that evaporation of

materials onto the NWs can be performed without breaking vacuum; enabling the possibility for depositing high quality, epitaxially matched thin-films.

**Device fabrication**

Devices created in this work generally follow the same basics as preparation of growth substrates. A highly doped Si+ chip with pre-patterned, lithography defined Ti/Au leads is used as a substrate. Nanowires are picked up from a substrate, using a micromanipulator needle, and deposited onto the chip. The chip is then spin-coated and is further patterned for contacts and sidegates using EBL. After developing, Ti/Au is deposited in the AJA metal deposition system, and the chip is ready after liftoff.

## 4.2 Parameters for Control of Nanowire Dimensions

Data described in this section is featured in the paper titled "*Double nanowires for hybrid quantum devices*"[45] (submitted).

The parameters necessary the creation of high precision designs are closely linked to the relative size of the nanostructures. For NW growth, the size of the Au catalyst is a parameter that can be tuned outside the VLS growth parameters; control of the Au size therefore forms the basis for defining the structural dimensions of independent NWs grown on the same substrate. There are two ways to influence the dimensions of the nucleator; the electron beam lithography (EBL) defined area on the growth substrate, which we describe in the terms of the number of pulsed EBL *shots* (EBLS) used to define the area; and the thickness of the deposited Au at the metallisation stage.

### 4.2.1 Lithography defined growth area, deposition thickness, and resulting Au particle dimensions

To understand the relation between electron beam lithography defined growth area and the resulting particle dimensions, a quarter wafer sized design populated sites made up of 1, 5, 10, 15, 20, and 50 EBLS was replicated on the four quarters of a 2" InAs wafer. At the Au deposition stage, each quarter was given an individual Au thickness of 20 nm, 50 nm, 75 nm, 100 nm, using an in-house designed quarter-sector mask, to selectively deposit Au layers without scribing the wafer.

The Au particles were characterised with SEM and the particle radii with automated image analysis. The particles adopt a disk shape at room temperature, we denote the radius of this disk $r_D$ and its height $h_D$, which is assumed to be equal to the thickness of the Au layer during metal deposition of the substrate. Fig. 4.1a shows a selection of SEM images from the sample. When $h_D/r_D$ increases the focus in SEM gets progressively worse, which can be gleamed from the images by comparing the images of $h_D = 20, 50, 100$ for any given number of electron beam exposures (*shots*). The fuzzy state of the SEM images of 1 and 5 EBLS defined particles meant large standard deviations between their measured radii, making them unsuitable for analysis. Fig. 4.1b shows the derived Au particle radii $r_D$ for particles as a function of the number of EBLS, for the four different Au deposit thicknesses, but they are offset by a thickness dependent parameter, independent of the number of EBLS.

Using $h_D = 20$ nm as a reference thickness, the residual radius of the 50 nm, 75 nm, and 100 nm disks can be fitted to a linear function. This yields a

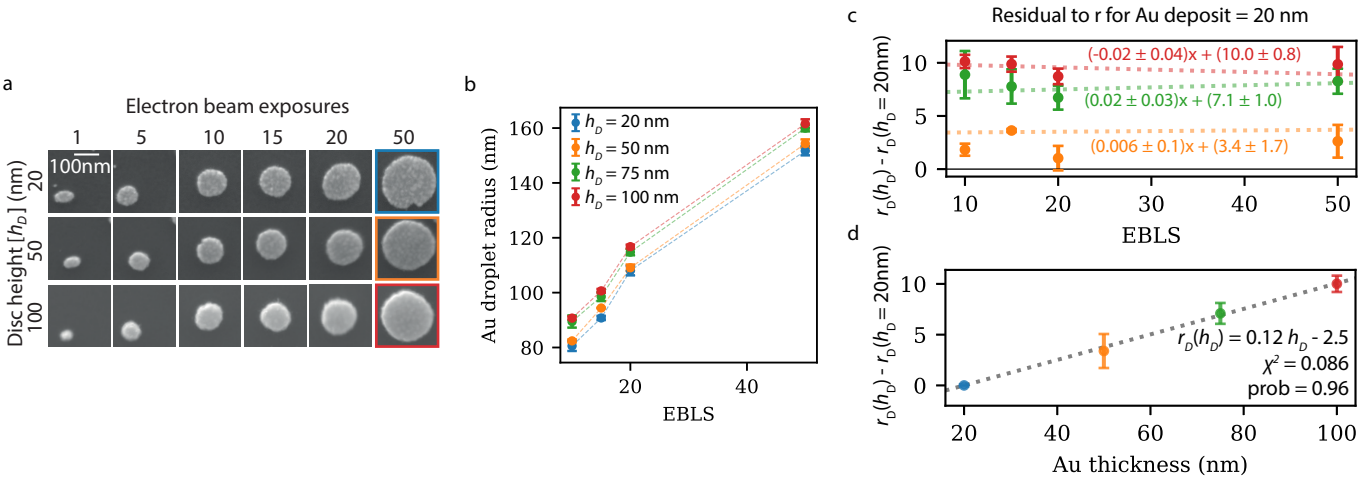


**Figure 4.1: a.** SEM images of deposited Au nucleators defined by different EBLS and deposition thicknesses $h_D$. **b.** $r_D$ for $h_D = 20, 50, 75, 100$ nm show a general trend, but with a noticeable offset in $r_D$ independent of EBLS. `MAX(`$\sigma$`)` $= 0.1$ nm, `MIN(`$\sigma$`)` $= 2.2$ nm, $\sigma_\mu = 0.56$ nm. **c.** Residual of radii $r_D(h_D)$ to the radii for Au thickness 20 nm, $r_D(h_D) = 20$ nm, fitted to linear functions in order to determine the offset parameter. Errors are estimated as the standard deviation of each data point from **b**. Inserted text shows the linear equations that yield the fit, where the offset is, $10 \pm 0.8$, $7.1 \pm 1.0$, $3.4 \pm 1.7$, for $h_D = 100, 75, 50$ nm respectively. **d.** Fitting the offsets as a function of Au thickness provides the relationship $r_D(h_D) = \alpha h_D + \gamma$ with $\alpha = 0.12 \pm (1.8 \cdot 10^{-3})$ and $\gamma = -2.5 \pm (4.5 \cdot 10^{-2})$; goodness-of-fit scores are chi2: 0.086, Prob: 0.96. A version of figure is featured in Ref. [45]: "*Double nanowires for hybrid quantum devices*" (submitted 2021), I collected the data, wrote the automated image analysis module, and analysed the data. Dāgs Olšteins designed and produced the growth substrate, and Thomas Kanne performed the growth.

near zero slope for all three residuals, and an offset term that is distinct for each height $h_D$ (Fig. 4.1c). These offsets, which correspond to some thickness dependent *minimum* radius, are linearly dependent on the thickness $h_D$, as shown in Fig. 4.1d, fitting this offset parameter yields the linear equation

$$r_D(h_D) = 0.12 h_D - 2.5 \,, \tag{4.1}$$

where all values are expressed in nanometers.

### 4.2.2 Influence of Au catalyst size and growth parameters on nanowire diameter

To investigate the relationship between the diameter of the NW and the size of its catalyst particle, a set of closely spaced NWs (placed with their facets in parallel) as well as single NWs were imaged with SEM in order to measure the diameter of the NWs. Al had been evaporated in a half-shell configuration, therefore the images were taken from the naked side of the NWs.[i] Fig. 4.2 shows a selection of double NWs grown in parallel, separated by 110 nm, with Au catalyst particles defined by 1-9 EBLS, to illustrate the changes in height, thickness, and rigidity.

The measured diameters of singly grown and double NWs for two MBE growth schemes as a function of the Au catalyst sizes are shown in Fig. 4.3a. Single NWs always grow thicker than double NWs, as the presence of a secondary Au catalyst creates an overlapping collection area, resulting in a mutual decrease in the collected number of adatoms, resulting in smaller NWs than the lone

[i]The samples originate from an earlier design made to induce growth of double NWs, created by Dāgs Olšteins and Thomas Kanne

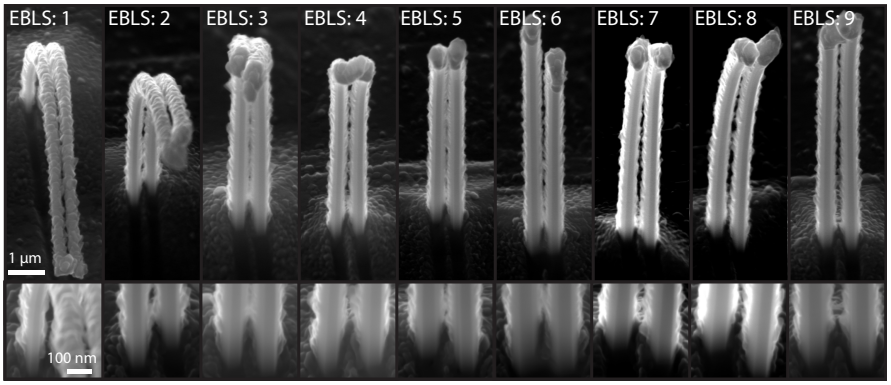


**Figure 4.2:** Selection of parallel grown NWs positioned with a spacing of $\sim$ 110 nm, stemming from EBL shot counts of of 1 to 9, from left to right respectively. A heavy layer of Al has been deposited, resulting in the bending of the less rigid, low EBLS count NWs. The scalebars are common to all images in their row.

grown NW. Different ratios of the As and In flux (defined V/III flux) yield distinctly different NW radii even for similarly defined Au catalyst particles, and the influence is significantly greater than the choice of Au catalyst size with an approximate 50-60% increase in radius when the ratio of the Ga to In flux is decreased during growth. Fig. 4.3b shows a selection of NWs defined by different catalyst sizes and different growth schemes, the difference is obvious.

### 4.2.3 Discussion

The need for finely tuned precision designs requires extensive understanding of the systematic correlations between variables in both design- and growth process. Understanding the relationship between the lithography defined Au catalyst area and the actual Au catalyst size forms the basis for controlling the exact dimensions of nanowires. This is relevant to both design of shadowed structures, but also for more complex architectures of coupled nanostructures.

Three parameters seem to dominate the final thickness of nanowires: The Au catalyst size, which is primarily controlled by the lithographically defined area where it is situated; but which can be increased with the use of a thicker deposition of Au onto the substrate. The growth scheme itself, which is seems to heighten or lower the nanowire diameter with distinct trendlines (although the data set should be expanded further for a more full picture). And finally, the proximity between Au catalyst particles, which directly influence the number of adatoms that are collected in the individual droplet during growth; and thereby the thickness of the nanostructure.

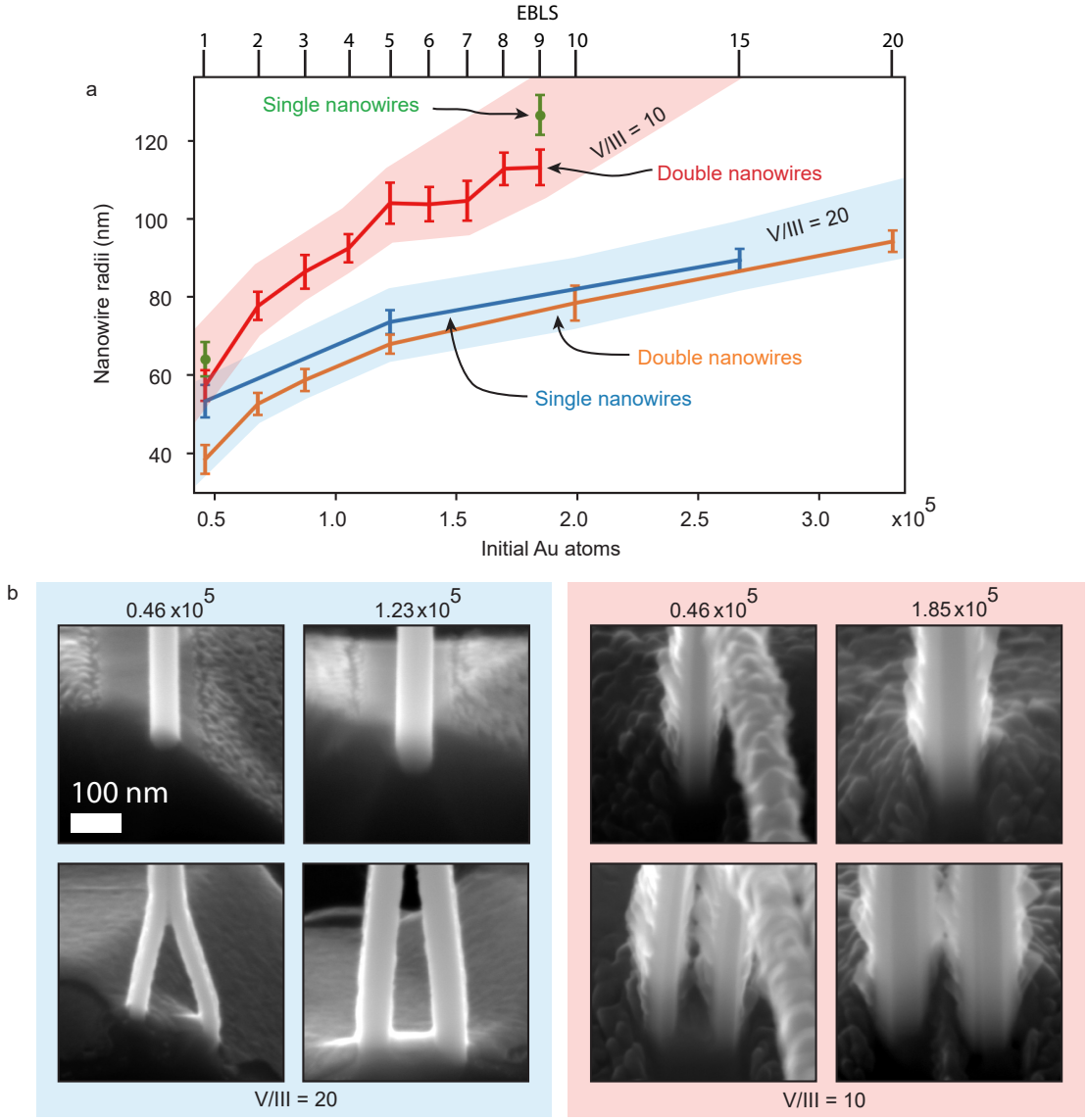


**Figure 4.3:** Comparison of single and double NWs for different Au catalyst size and chemical composition. **a.** NW diameters for single and double NWs as a function of the initial amount of Au atoms (bottom axis), and electron beam lithography shots (top axis). The close presence of a secondary Au catalyst always ensures a mutual decrease in the collected number of adatoms as they must share part of the collection area, in turn forming smaller NWs than their lone counterpart. The choice of flux ratios between In and As during growth plays a larger role than the size of the Au droplets, and enters as an extra control parameter. The blue area marks NWs grown specifically to induce merging of the structures, the red is for a V/III flux parameter with the intention of letting close proximity NWs grow in parallel, but without merging. The size and path of the areas are for illustrative purposes only, to distinguish the data belonging to each growth scheme. Growth schemes by Thomas Kanne, described in Ref. [45]. Each data point is the mean of at least 6 observations, and the error bars are the standard deviation between them. Note that the EBLS/Initial Au atoms is not an entirely linear relationship. **b.** Close-up SEM images of NWs grown from Au catalyst with different amounts of atoms ($0.46 \cdot 10^5 \propto 1$ EBLS, $1.23 \cdot 10^5 \propto 5$ EBLS, $1.85 \cdot 10^5 \propto 9$ EBLS. This figure is adapted from [45]: "*Double nanowires for hybrid quantum devices*" (submitted 2021), I collected the data via SEM and Thomas Kanne performed the analysis and figure design.

# 5 Shadow Engineered Nanowires

This chapter introduces the principles of shadow patterning. The necessary equations for fine control of the process are described. This is followed by a description of selected design patterns to made for the purpose of forming Josephson Junctions, and the experimental realisation of these designs. The chapter ends with a design scheme for the in-situ contacting of an epitaxial Pb layer of lead to gold Au, followed by its experimental realisation.

## 5.1 Shadow Patterning Principles

Shadow masking/patterning has proven a very effective method for in-situ deposition, able to yield epitaxially matched, complex heterostructures with exotic material combinations,[21,46] and the method is increasingly used as a pathway for maintaining the integrity and cleanliness of materials suitable for quantum devices.[20,47]

This section will establish the parameters and considerations necessary for very exact control of the process, enabling fine tuned precision deposition.

The basic principle is illustrated in Fig. 5.1. There are two general methods with two different goals. An object can be placed in front of the target NW, blocking the source from some height and down to the bottom (Fig. 5.1a). An example of this could be a NW placed in front of another NW. If the deposition angle is extreme enough, a region forms between the full flux and the null flux zones, where the flux is gradually decreased. The second option is to use a floating object as a selective barricade to create en enclosed *dark* region; a null flux zone, neighboured by two finite flux regions (Fig. 5.1b). Such an object could be a hanging bridge on a specialised substrate;[21] or a secondary NW that

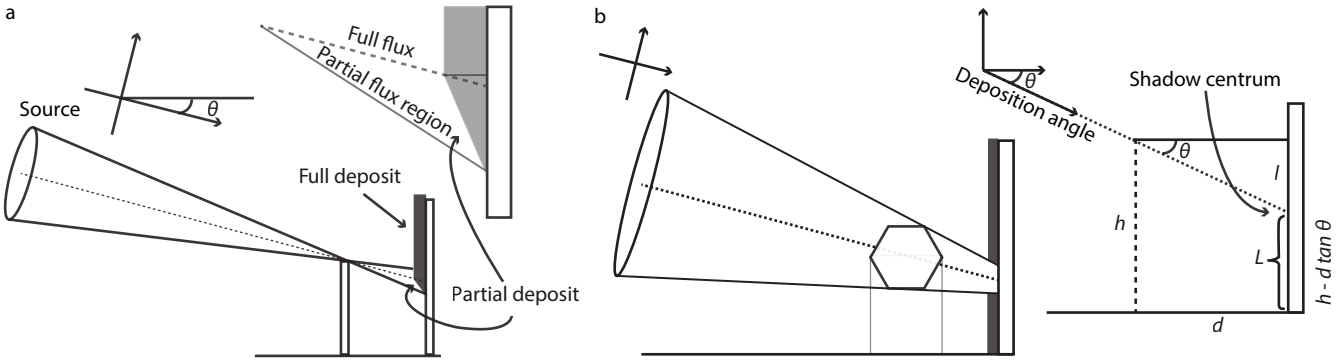


**Figure 5.1:** Illustrated principle of shadow deposition. **a.** Naked substructure achieved by placing a solid obstacle in front of the target NW. **b.** Junction created by a *floating* object, for example a kinked NW with its protrusion blocking the flux in a selective region.

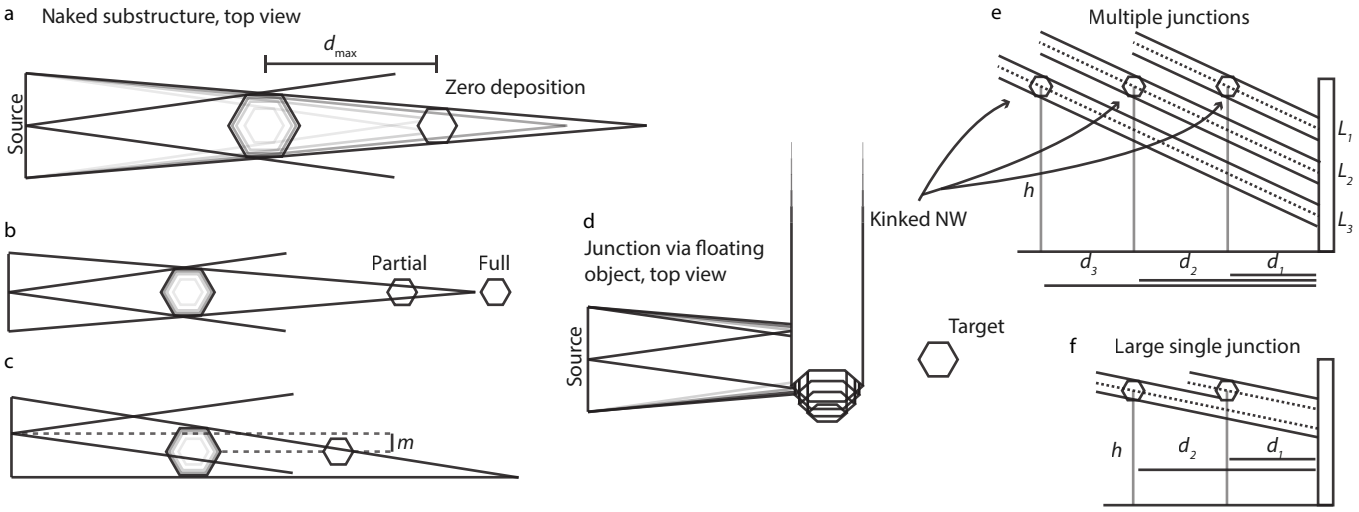


**Figure 5.2: a.** Top view of standing solid NW (as in Fig. 5.1a), creating a null flux zone around a target NW placed near the limit $d_{\max}$. **b.** As $d/d_{\max} > 1$ partial regions of the target NW are exposed to the full flux region, as $d/d_{\max}$ increases further the entire target NW is engulfed in the full flux region. **c.** Misaligment $m$ leading to partially exposed target NW. **d.** Top view of the floating object regime, realised with a secondary NW that has kinked and continued growing, acting as a suspended barrier. **e.** Multiple secondary, kinking NWs enable the definition of multiple junctions. They are constrained primarily by the limits of $d_{\max}$, but an angular component modifies the upper and lower boundaries of $d$. **f.** If the height $h$ is equal for all multiple structures, then $\theta \to 0 \implies L_{n\neq 1}(d_{n\neq 1}, \theta, h) \to L_1(d_1, \theta, h)$. The possibility to overlap the projected shadows of multiple structures allows for variations in junction length beyond the constraints of the width of the secondary NWs (which also limits their potential height).

bends, or branches directly into the line of deposition. We will concern ourselves only with NWs.

The most important equation governing these methods is also the simplest: Let $\theta$ be the deposition angle and let $d$ by the distance from the shadowing structure to the target structure, the offset $l$ of the shadow cast from the shadowing structure of height $h$ is

$$l = d \tan\theta \ , \tag{5.1}$$

and the position of the shadow, projected onto the target $L$ is then

$$L(d, \theta, h) = h - d \tan\theta \ . \tag{5.2}$$

Under the assumption that the zero flux region projected from the shadowing object adopts a uniform cone shape, some constraints on the values $d$ can adopt arise. Fig. 5.2a and b illustrates a NW shadowed by shorter, thicker NW placed in front of the target NW, akin to the situation displayed in Fig. 5.1a. If the distance between shadowing object and target increases beyond some limit $d_{\max}$, then the target will begin to receive a partial, or full deposit, depending on the ratio $d/d_{\max}$. The same occurs if the size of the shadowing object is decreased, or the size of the target object is increased beyond some limit. The shape of the source has an influence, we will assume it is a crucible with a surface shape approaching a circle with radius $r_s$, and is distanced to the shadowing NW by $d_{ss}$. We denote $r$ as the radius of the shadowing object, and $r_t$ as the radius of the target, and write

$$d_{\max} = d_{ss} \frac{r - r_t}{r_s - r} \ . \tag{5.3}$$

This is of course bound by the situation $r > r_t$, but in practice, where $d_{ss} \gg (r/r_t)$, very small variations in the realised NW sizes may allow $d_{\max} \neq 0$ even if $r \to r_t$.

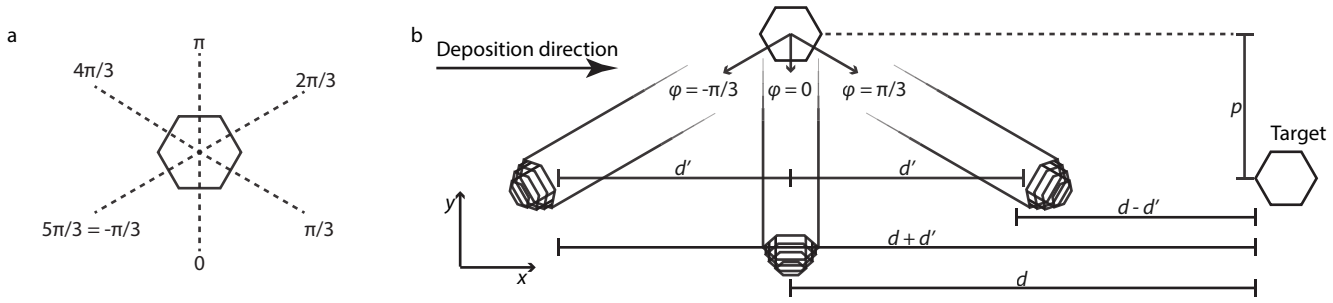


**Figure 5.3: a.** Expected kinking directions of the hexagonal structure. **b.** A secondary NW is placed at some $y$-axis offset $p$ (pitch) and distance $d$ to a target NW, the kinking direction can modify the effective distance by $p \tan \phi$, where $\phi = 0$ is a kink perpendicular to the $x$-axis (deposition direction).

Misalignment of the NW pattern with respect to the source introducing non-uniformity in the shape of the null flux cone, expressed as a change in the angles between the source edges and the shadowing object. The situation is shown in Fig. 5.2c; a target NW that would otherwise be fully covered if the pattern was aligned perfectly, instead receives a partial-, or full deposition depending on how big the misalignment is. Misalignment $m$ enters the equation as an offset in the radius of the source, so we rewrite Eq. (5.3)

$$d_{\max} = d_{ss} \frac{r - r_t}{r_s + |m| - r} \, . \tag{5.4}$$

For floating objects, the shadows will be projected from secondary NWs placed in close proximity to the target, which can be kinked on purpose,[48] and grow along a new direction, e.g. into the deposition path from the source to the target. Fig. 5.2d illustrates such an example where the possible deposition paths of the source are more limited. If multiple of such secondary NWs are placed in a specific pattern, a set of junctions can be defined with control over their positions on the target NW as illustrated in Fig. 5.2e. Depending on the deposition angle, such a scheme could be used for making junctions of different characteristics; for example, as $\theta \to 0$ an overlap between projected shadows starts to form, allowing increased junction lengths beyond their $r$ defined constraints (Fig. 5.2f).

For small values of $\theta$ (<20), Eq. (5.3) still holds for floating objects, but $r_t$ now becomes the radius of the projected shadow $r_L$,

$$r_L \approx r - \left( \frac{d}{d_s} (r_s - r) \right) \tag{5.5}$$

where $d_{\max}$ is now simply $d$, distance between shadowing object and target. So junction lengths can be individually defined by tuning the dimensions and placement of the shadowing object. So can individually define junction lengths according to the desired width of $L$. Misalignment does not enter into the equation unless $m$ is increased beyond the length of the kinked segment.

Fig. 5.3a shows the expected kinking directions for an InAs NW. Because the hexagonal structure promotes kinking directions perpendicular to the facet, there are three scenarios that result in comparable (although slightly different) shadow patterns, illustrated in Fig. 5.3b. If we assume that a kink is always sufficiently long to block deposit path, let then the pitch $p$ denote the offset in $y$-coordinate from the base of the secondary NW, let the $\phi$ be the angle of the kink, where $\phi = 0$ is the direction perpendicular to the deposition direction, as illustrated in Fig. 5.3b), let $d$ be defined only for the $x$-axis, and let $d'$ be the

| $\phi$ | $L$ |
|---|---|
| 0 | $h - d\tan\theta$ |
| $+\pi/3$ | $h - \left[(d - \sqrt{3}p)\tan\theta\right]$ |
| $-\pi/3$ | $h - \left[(d + \sqrt{3}p)\tan\theta\right]$ |

**Table 5.1:** Possible shadowed positions cast from a kinking structure located at coordinates $(x, y) = (d, p)$ at a deposition angle $\theta$.

$x$-coordinate distance between the $\phi = 0$ kink and a $\phi \neq 0$ kink such that the effective distance of the kink to the target becomes

$$d_k \equiv d + d' \tag{5.6}$$

$d'$ generalises to

$$d' = p\tan\phi\ . \tag{5.7}$$

and (given the constraints on kinking directions) simplifies to

$$d' \equiv \begin{cases} 0 & \phi = 0 \\ \pm\sqrt{3}p & \phi = \mp\pi/3 \end{cases} \tag{5.8}$$

So for a given shadow position, there are two alternative possible results (5 alternative possibilities if we include the fact that the kink might not even grow in our desired direction), summarised in Tab. 5.1. The generalised shadow position equation is limited to cases where the kink grows in any direction that lies between perpendicular and parallel to the deposition direction,

$$L(d, \theta, h, \phi) = h - \left[(d - p\tan\phi)\tan\theta\right],\ |\phi| < \pi/2 \tag{5.9}$$

There is 50% chance that the kink extends in a direction opposite the pattern. A strategy to increase yield of useful NWs is to place two secondary NWs opposite each other. There is experimental evidence to suggest that close proximity of NW structures lowers the likelihood of kink formation, and although the exact mechanism behind this is not currently understood, the workaround consists of placing the two opposing NWs with a slight offset to each other.

To end this section, a design that utilises the concept of a standing secondary NW and two floating/kinking secondary NWs is shown in Fig. 5.4. The optimal distances $d$ are determined from input parameters: deposition angle $\theta$, expected height of the nanostructures $h$, and the desired separation between shadow positions $L$. The pitch $p$ can be set freely constrained only by the expected length of the kinked segment. This design, and other variants will be discussed in Sec. 5.2.

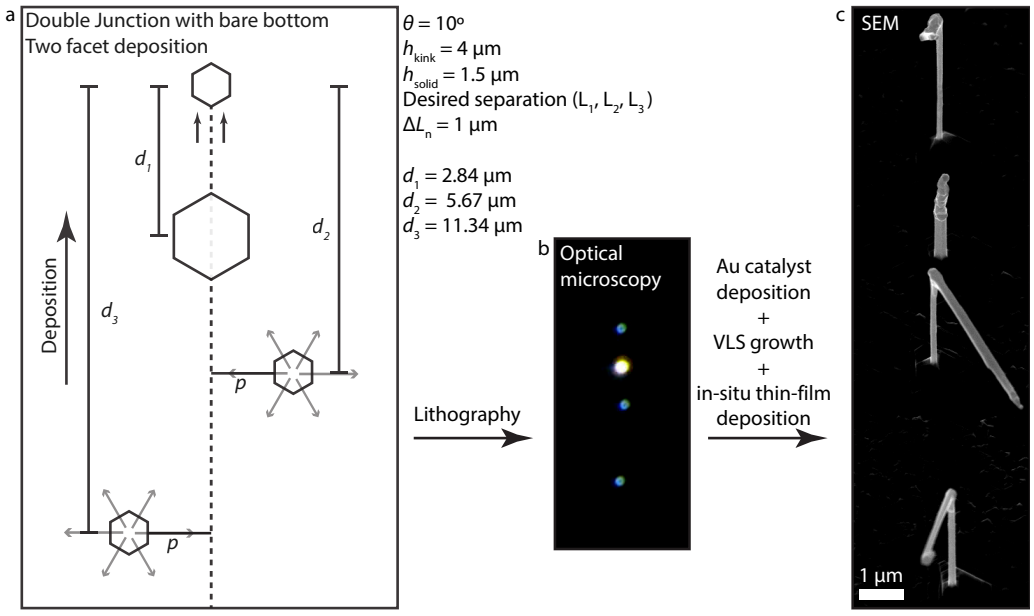


**Figure 5.4: a.** Design example for a double junction NW with a naked substructure. Two kinking NWs and a larger, shorter NW, which possess low kinking probability. **b.** Optical microscopy of the substrate after lithography shows the definition sites for deposition of the Au catalyst. Orientation follows the design in **a**; showing the target NW at the top, followed by the thick, short NW, Scanning electron microscopy of the finished design shows an example of sub-optimal NW kinking, but since the direction adds $\sqrt{3}p$ to both $d_2$ and $d_3$, and $h_2 \approx h_3$, the separation $L_2 - L_3$ roughly maintained.

## 5.2 Shadow Junctions

Having established the parameters necessary for fine control of the shadow deposition, we will move to the experimental realisation of shadowed junctions formed on InAs NWs using Al as the deposited metal.

Double junctions made of superconductor-semiconductor-superconductor-semiconducor-superconductor (or S-N-S-N-S, S: superconducting state, N: normal state) materials are among the current proposals for hosting exotic quantum states, specifically Majorana bound states hosted at the two far ends of a superconducting thin-film (Sec. 1).

The designs presented here were made with two purposes; as a trial of the shadow patterning technique, and as the experimental realisation of multiple junctions on a single NW, with controlled junction dimensions. We will start with a presentation of the designs themselves, before exploring their realised counterpart.

### 5.2.1 Design principle

The designs are based on the ability of NWs to extend radially (to kink), if the nucleating (Au) element is transferred to one of the facets of the NW during VLS growth (accomplished by the introduction of a small amount of gallium when the NW has grown to its desired height). We will refer to these as kinked-, or kinking nanowires (KNW) or structures, while the main NW (the shadowed) is referred to as the target nanowire (TNW). The parameters controlling VLS growth, such as the timing of the Ga flux will determine the height at which the kink occurs. For our purposes, the NW height and thickness will primarily depend on the size of the nucleating particle. Combinations of Au particle sizes

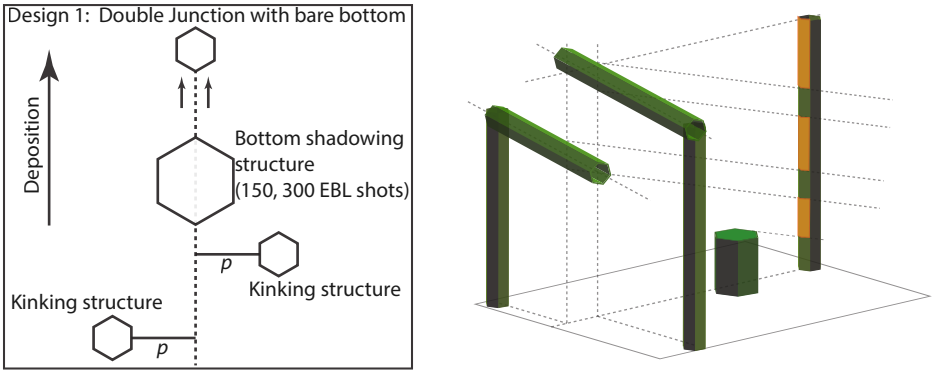


**Figure 5.5:** Design 1. The simplest in terms of *things that can go wrong*. Left: Schematic, top down view. Right: Projection view (the nucleating gold cap is hidden for clarity). Two facets are coated in the deposited material, owing to the hexagonal structure and its orientation to the substrate. As the kinking directions protrude from the facets, the orientation ensures maximal likelihood that the kinking direction points towards the central axis (dashed line).

can be used to achieve various goals; for example, a tall TNW grown together with smaller thicker KNWs can be used to produce long segments of metal coating, or yield long junctions if the kink is sufficiently thick. At significant thickness, the larger particles, resulting in small but wide NWs, usually do not kink, and can be used to shadow the entire bottom section of the TNW if placed in close proximity.

### Design 1 and 2: Double Junction with naked bottom

Design 1 and 2 are intended to produce a NW with two junctions in sequence and a terminating thin-film layer towards the bottom of the NW.

Design 1 is illustrated in Fig. 5.5. Two kinking structures are placed pitched a distance $p$ left and right with respect to the central axis of the design (perpendicular to the deposition direction). The pattern is intended to produce NWs aligned such that the deposited film covers two facets of the TNW, but more importantly, the possible kinking directions (protruding from the hexagonal facets) maximise the possibility that the kinked structure extend in front of the TNW. A short structure is placed central to the TNW, shadowing the bottom part.

Design 2 (shown in Fig. 5.6 left panel) is a variation without the short structure, instead attempting to produce the bottom shadow by placing a kinking structure central to the TNW, in the same manner as one would the short and thick NW, but relying on the much taller KNW to do the job. The idea behind this comes from the possibility that the bottom KNW can also shadow one of the other KNWs producing a single junction NW in addition to the TNW.

The width of the short structure in design 1 minimises the negative impact of misalignment of the pattern during substrate preparation. The bottom NW in design 2 risks not shadowing the TNW in cases where it lacks the proper height, which can occur if the kink is initiated early, or if the NW in general is too short. Disregarding these two problems, both designs should have similar probability of success (defined as both kinked structures pointing inwards towards the centre) $\sim 25\%$.

### Design 3: Triple Junction with naked bottom

Design 3 is illustrated in Fig. 5.6 middle panel. The intention is to produce three junctions in sequence, and to terminate the thin-film near the bottom of the NW.

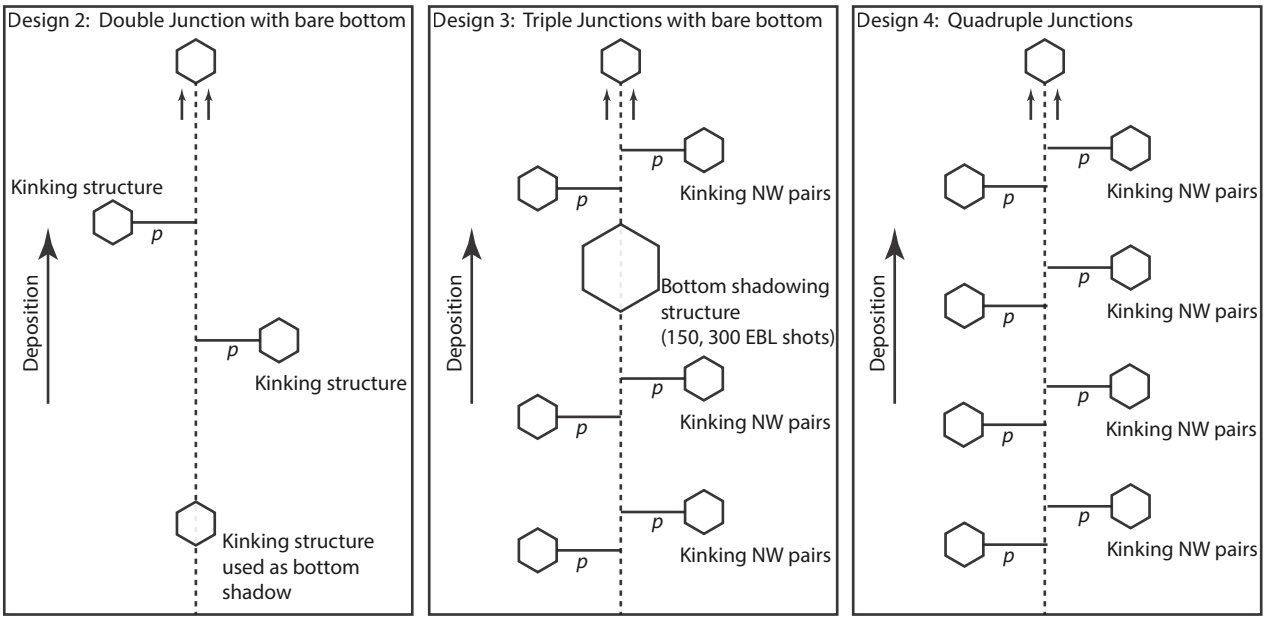


**Figure 5.6:** Schematics of designs 2, 3 and 4, intended for double-, triple-, and quadruple junction NWs respectively.

It is also designed to increase the probability of junction formation by placing pairs of KNWs opposite each other, in principle, doubling the probability of a kink pointing in the correct direction. It has been empirically observed that the propensity to kink is reduced when NWs become closely spaced, for this reason the paired KNWs are distanced 200 nm apart with respect to the deposition direction. A thick, short NW is used to ensure the termination of the bottom thin-film segment. Depending on the distance between KNW pairs, additional kinking structures have a chance to create a suitable shadow junction on one of the other kinking structures. This is especially the case if the pattern is slightly misaligned. The kinks often grow equally long, or longer, than the height of the NW, thus if the spacing is large enough for NWs to not shadow each other, or if there is some misalignment in the pattern, a double junction can form on the two NWs closest to the TNW, and single junctions can form on the middle NW pairs.

#### Design 4: Quadruple Junction

Design 4 is illustrated in Fig. 5.6 right panel. The intention is to the maximise the number of junctions, both on the TNW but also on the KNWs that make up the rest of the pattern. This design is the least sensitive to misalignment; in fact, it is improved if misalignment occurs, as the multitude of KNWs can produce shadows onto their counterparts along the deposition direction. In the best case scenario, four well defined junctions are produced in sequence on the TNW.

### 5.2.2 Results

The designs were patterned on a InAs 2" wafer growth substrate, prepared according to the standard protocol described in 4.1, and grown with the VLS mechanism using molecular beam epitaxy. For each design, variations of the nucleating droplet sizes were these: For the shadowed/TNW, seven variations

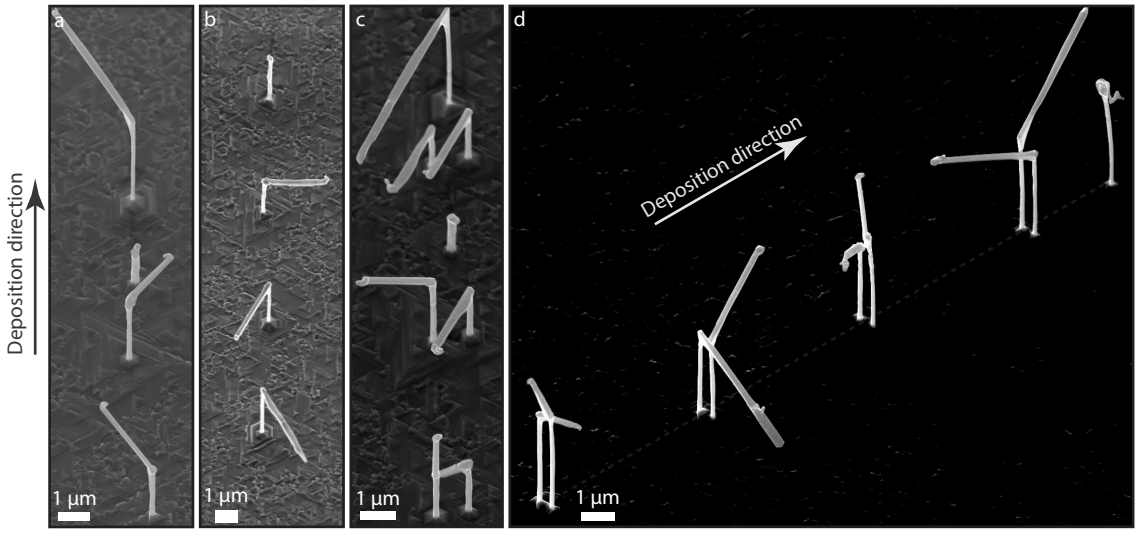


**Figure 5.7:** The four designs realised. The images are randomly selected and illustrate differences in NW height and diameter. **a.** Design 1. **b.** Design 2. **c.** Design 3. **d.** Design 4.

on the number of single electron beam lithography (EBL) shots were tried: 1, 5, 10, 15, 20, 25, 50, which gradually decrease the height of the NW, while also increasing thickness. The same variation of EBL shots were tried for the KNWs. For the bottom shadowing NW, aiming for a short stature, but wide structure, 150 EBL shots and 300 EBL shots were used. Four variations on the pitch $p$, distancing the wires by 200 nm, 300 nm, 400 nm, and 500 nm. This amounts to 392 combinations for design 1 and design 3, and 196 combinations for design 2 and design 4.

Fig. 5.7 shows scanning electron microscopy (SEM) image examples of the realised designs. In all of the example, the desired kinking direction has been fulfilled, either in all cases (Fig. 5.7a and b), or partially by at least one member of the NW pairs (Fig. 5.7c and d).

Design 3 proved to be the most successful in terms of creating the intended junctions. Due to a small misalignment of the pattern with respect to the wafer, it also produced an ample supply of double junctions. The performance of design 1 and 2 is comparable. The small misalignment of the pattern, resulted in the thick NW in design 1 not always being successful in shadowing the bottom of the target. Design 2, with its kinking bottom shadowing NW, can in some cases compensate if the kinking orientation happens to point the correct way. A combination approach of design 1 and 2 would gain the benefit of both designs without any apparent sacrifice. No quadruple junctions were found, but double and triple junctions were present. If double junctions are included as a success criteria, then the rate of success for design 4 is 7.4% when the KNWs were thin (1 EBL shots), but 3.7% when this was raised to 5 EBL shots and 10 EBL shots. The NWs furthest away from the target were too far away for the given deposition angle. The ratio of success for design 3 is roughly 8:3 compared to design 1 and 4.

To illustrate the growth, and to comment on some observations, we will discuss a few samples.

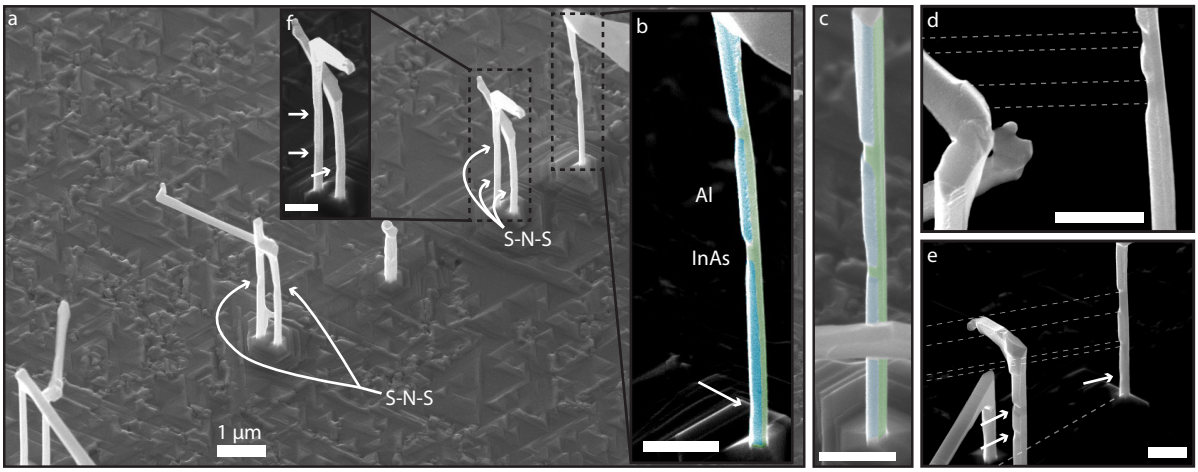


**Figure 5.8:** Shadow patterned double junctions imaged with SEM. **a.** A design 3 pattern. Three single junctions are formed on the non-TNWs, and one double junction. **b.** Pseudo-coloured close-up of the TNW from **a**. The white arrow points to the partial formation of a third junction. The thin-film thickness is roughly 25 nm. **c.** Pseudo-coloured double junction. **d.** SEM of a short double junction near the top of a TNW. Dashed lines are drawn in accordance to the deposition angle. **e.** Relatively long junction followed by a short junction; attributed to the kinking orientation of the far back NW. At the bottom of the TNW, a partial third junction is partially shadowed (indicated by a white arrow). Note also the additional double junction formed on the secondary NW. Dashed lines from the junctions are drown in accordance to the deposition angle. Dashed line drawn from the base of the NW follows the central axis of the design pattern. **f.** Slightly zoomed and contrast edited inset in **a** with junctions annotated by white arrows.

### Double Junctions

A selection of well defined double junctions is presented in Fig. 5.8. Fig. 5.8a: Intended for a triple junction. In addition to the junctions formed on the TNW, three separate single junctions are formed on the additional (kinked) NWs, and one double junction is formed on a KNW.

Fig. 5.8b shows a close-up of the TNW from the same pattern, displaying two well defined junctions. The third junction is not fully formed, but a trace of its formation is seen as an indent in the Al film, where the film becomes thinner due to only being partially shadowed. For this to form a triple junction, the entire pattern should be positioned closer to the target, while reducing the height of the KNW pairs. The design could also be made more compact, if a long thin-film island is not the goal.

Fig. 5.8c shows an example of two well defined junctions formed on the TNW, also displaying the highly pristine morphology of the epitaxial thin-film.

For thinner NWs, the kinking direction is not always perfectly radial from the NW, the protrusion sometimes appears diagonally from the intended direction. Fig. 5.8d shows an example of a typical result, the SEM image is taken near the top of a TNW, where two kinked structures in the pattern have kinked diagonally, one of which can be seen in the figure. When the KNWs are spaced in the right way, their diagonal protrusions may collectively create two short junctions in sequence, as is the case in the figure, or they may overlap to create a junction that can vary in length as a function of the amount of overlap.

The half-formation of a third junction is somewhat common, the signature indent in the deposited thin-film is noticeable for most of the TNWs when the KNWs are formed by 1-10 EBLS. Fig. 5.8e shows a TNW suitable for a double junction device, but with a small indent in the thin-film near the bottom. For device purposes, this area would be covered by a contacting lead, and is not an issue. The indent however, can also occur if the design uses a thick, middle NW,

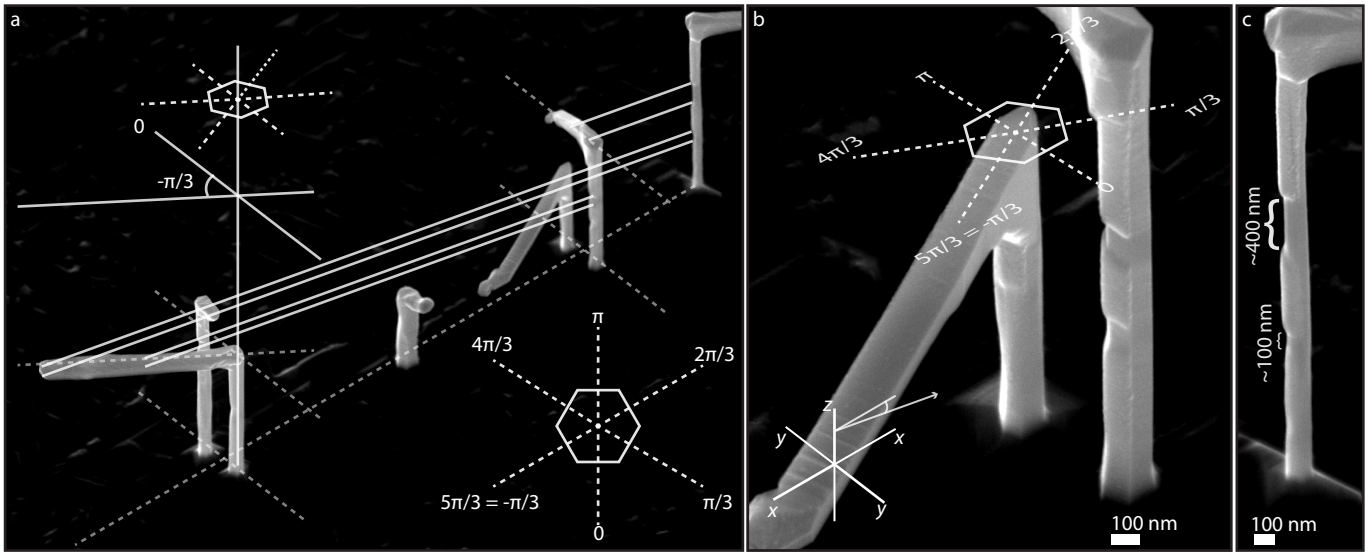


**Figure 5.9: a.** Illustrating the effect of an alternative kinking direction. The overall morphology of the kink can contribute to a difference in coverage area, as seems to be the case here. Note that the SEMs are taken at a 30°angle, skewing the perspective. The neighbouring NW does not kink far enough to create a shadow. Lines are added as a coordinate system and can be compared to the illustrated designs in Fig. 5.6. The NW-to-NW lines are drawn from the borders of each junction, they are oriented with respect to the deposition angle and the central axis of the design. Illustration in the bottom right corner shows the standard directions for radial growth protruding from a hexagonal facet. **b.** Close-up of the front KNW pair, the schematic has been skewed 30°to match the perspective of the image, when this is done, the kinking direction matches the expected facet-determined direction. The facets of the KNW are easier to see at the bottom of the NW. The arrow in the coordinate system shows the deposition direction. **c.** Close-up of the TNW, with approximate measurements of the junction lengths (the bottom junction length includes the border region with partial shadowing). Since the image is taken at a 30°angle, the scales should be doubled when measuring vertically.

and the pattern is slightly misaligned. Even if the 150-300 EBLS NWs do not kink, their Au cap may move around a bit, and sometimes grows a small hat, that can create unintended shadows, or partial shadows.

The NW shown in Fig. 5.8e also displays a peculiar feature, a long junction followed by a short junction. The long junction is abnormally long (around 400 nm), this is a result of the front KNW having a considerably thick kink. Secondly, the small junction is smaller than intended (the junction measures around 100 nm when the partial shadow is included, making the junction itself much smaller). The explanation comes from the kinking orientation. When the kinks are not aligned perpendicularly to the deposition direction, the effective distance is slightly changed, which can also change the coverage area of the shadowed NW. Fig. 5.9a shows a larger view of the design that resulted in the aforementioned junction. By tracing a line from each border of the formed junctions, and orienting them with respect to the deposition source angle, it is possible to estimate the origin of the shadow, revealing that the small junction is the result of a sideways kink in one of the bottom KN, which however extends just far enough for the edges of the kink to form a small shadow on the TNW. The image is also an example of KNWs that kink in accordance to their hexagonal facets. Fig. 5.9b shows a close-up SEM of the front KNW pair with diagram of the kinking directions. Fig. 5.9c is a close-up of the TNW, the large junction measures approximately 400 nm, and the small junction is circa 100 nm. The width of the TWN itself is estimated to around 110-120 nm. Note that the perspective is skewed 30°, so when measuring the heights the scales should be doubled.

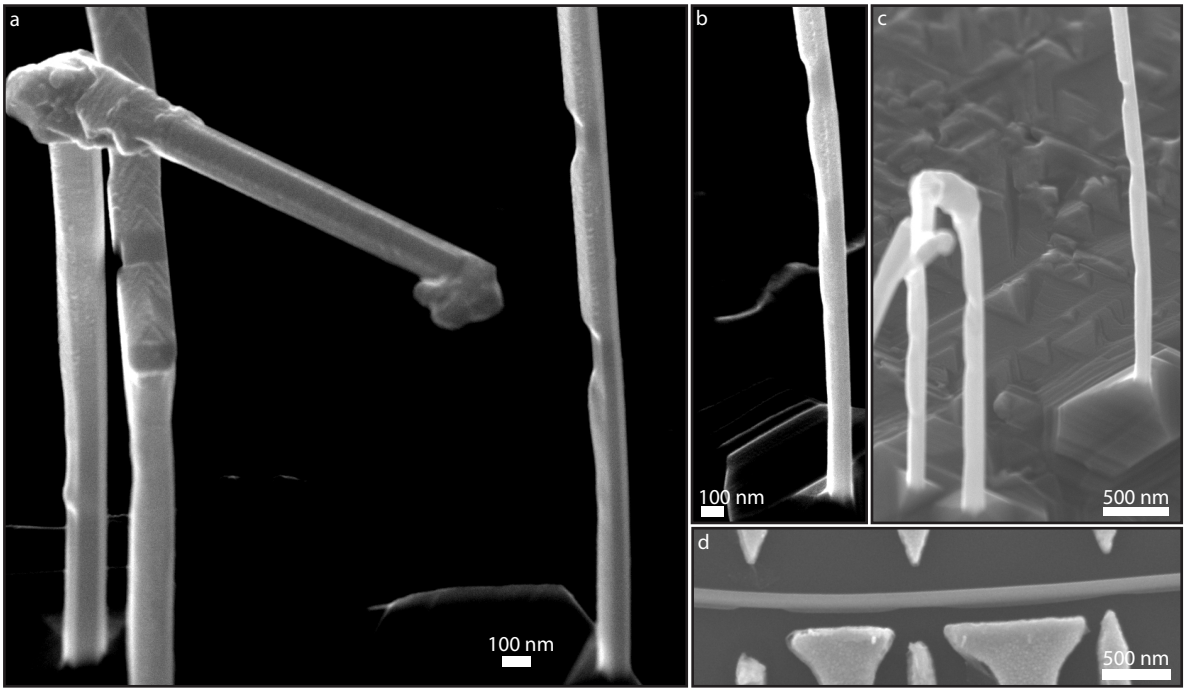


**Figure 5.10:** Shadow pattern triple junctions viewed in SEM. **a.** Top to bottom: The two first junctions are easily noticeable, showing well defined features and film morphology. The Al film becomes less consistent after the second junction, but terminates after about 1 µm, leaving a bare InAs bottom. Note the SEM stage is tilted 30°during imaging, so the scale is doubled when measuring vertically. **b.** Two well large junctions followed by a small, circa half-sized junction. Again the Al film terminates after approximately 1 µm. **c.** Triple junction TNW and double junctions formed on the front KNW pair; a slight indent in the bottom part of one of the KNWs suggests possible formation of a third junction; the result of a slanted kink further back in the pattern. **d.** SEM of a device created from one of the triple junction NWs from this batch. Again the first top junctions (left side) are highly consistent, while the bottom becomes smaller, with a longer partially covered region.

### Triple Junctions

Fig. 5.10 shows a selection of successful triple junctions. A common occurrence for triple junction patterns is the formation of two long and well defined junctions, followed by a smaller junction with a slightly less well defined morphology. This occurs when the thin film decreasing gradient becomes small, making the decrease more continuous in nature. Besides the random effects of kinking, leading sometimes to smaller, or less well defined junctions, an additional effect comes from the effective width of the shadows being decreased as their distance to the TNW grows. It is a simple effect of the deposition source being many times larger than the shadowing objects, making partial shadowing from the edges of the source a very real issue. When this happens, the thin film risks not terminating at all, but simply approaching a *very* thin film layer where the junction should form. This makes some of these smaller junctions difficult to address in SEM and they should preferably be imaged using TEM to prove that they indeed form the intended junctions. Fig. 5.10d shows a triple junction NW that was selected for integration into a device, the junction far right side of the image is a good example of a small, gradually decreased, yet clearly defined junction.

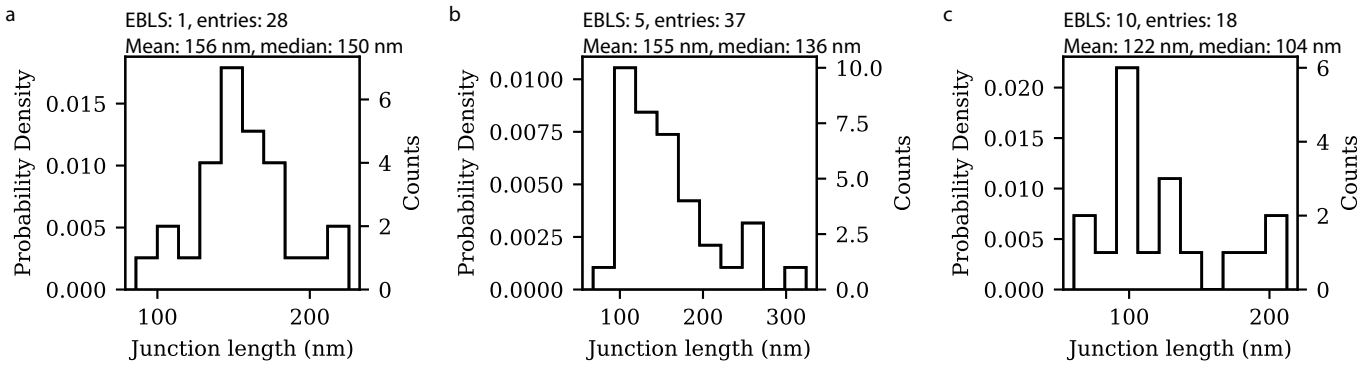


**Figure 5.11:** Distributions of junction lengths for shadow junctions defined by KNWs grown from nucleating catalyst particles of **a.** 1 EBL shot, **b.** 5 EBL shots, and **c.** 10 EBL shots.

#### Junction lengths

The length of 83 shadow junctions have been measured by SEM. There is generally a discrepancy between junctions formed by KNWs with their expected size, and KNWs that are thicker in their kink than in the base NW. For examples of this, refer back to Fig. 5.8e and f, which produce junctions that are considerably larger than their intended length. An ideal case scenario was presented in Fig. 5.10a. The length measurements were primarily performed on patterns where the KNW was not excessively thick. Fig. 5.11a, b, and c, show the probability density distributions of junction lengths formed by NW sizes defined by 1, 5, and 10 EBL shots, respectively. Junctions formed by the thinnest wires approach a normal distribution with a mean of 156 nm. Contrary to expectation, increasing the NW thickness did not yield thicker junctions, the 5 EBL shot defined NWs have roughly the same lengths (mean = 155 nm), although the distribution is skewed slightly towards smaller values. Increasing the NW thickness further skews the distribution towards yet smaller junctions, the 10 EBL shot defined NWs produce junctions mainly of about 100 nm; the distribution appears Gaussian, but the statistics are too sparse to properly determine its exact nature.

If we assume that the fluctuations in junction lengths are not associated with NW thickness, or that changing the NW thickness also changes other parameters (such as their height, and thereby effective shadowing angle), meaning that the junctions cannot be separated into distinct categories, the junction lengths become normally distributed (Fig. 5.12). Fitting a Gaussian to this distribution yields a good fit, with a mean junction length $\mu = 136 \pm 3$ nm, and standard deviation $\sigma = 40 \pm 3$ nm (chi-squared = 10.72, Ndof = 15, Prob = 0.77, fitted to the frequency/count binned distribution).

### 5.2.3 Conclusion

The formation of double and triple junctions has been demonstrated quite clearly by selected examples. The design patterns have proven useful even in the face of small misalignment, which hinders the intended bottom shadowing; but in turn can produce a wealth of double junctions formed on secondary NWs. Double junctions are well defined, with junction lengths being consistent with the intended pattern. They exhibit well defined borders, the thin-film morphology appears pristine in SEM. Triple junctions suffer from unintended variations of the third junction, but not in a manner that renders them uninteresting for

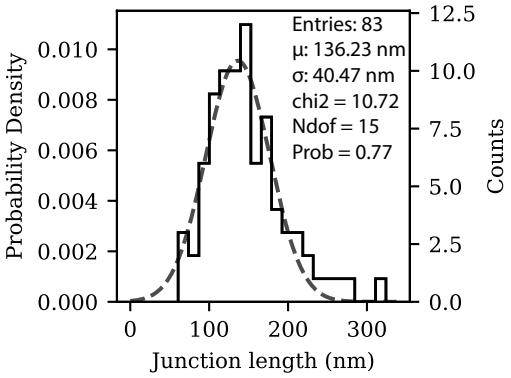


**Figure 5.12:** Distribution of collected junction lengths.

device purposes. At the time of writing, NWs produced from this growth have been used in 20 quantum devices of various designs.

83 junctions have been measured in SEM, revealing differences between junction lengths when the KNW height-to-thickness aspect is reduced. The focus was on junctions where the kink of the KNW is similar to its base structure, this means that some additional outliers may pop up if the measurements were performed again without regard to this criteria; with enough data the distributions even might skew towards larger junction lengths.

The average junction length of these *correctly* small junctions ranged between ~100-155 nm depending on the KWN thickness as defined by its Au particle size, with thicker KNWs yielding smaller junctions. The exact nature of why this is not clear, but one explanation for the apparent decrease in junction length with thicker NWs could be that the expected height the NWs also decrease, which slightly alters the effective shadow angle, something which was not accounted for in the design variations. A close study of the NW height as a function of catalyst particle size, under equal growth conditions could possibly enable the future designs to account for this problem.

Above 15 EBL shots, kink NWs typically did not grow tall enough for the shadow of those furthest away to reach the TNW. If a sufficiently large deposition angle is chosen, the shadowing NWs can be placed closer together, which would improve the possibility of success in general, but this introduces the possibility of an uneven distribution of the thin-film. One problem to consider for the paired NWs in design 3 and 4, is the chance of closely spaced kinks to collectively produce a larger junction than intended, if their width makes this shadow overlap possible. An alternative outcome could be the formation of a very small thin-film segment formed in the middle of a junction that appears to stem from correctly oriented NW kink pairs, if the NWs kinks are too thin.

The width of the middle, thick structure should generally be made as large as possible. NWs grown from nucleation particles made from $\geq 5$ EBL shots are usually rigid enough that their tendency to clamp together is heavily reduced. Only in cases where the wide NW is in extremely close proximity (less than 100 nm) to a thin NW is there a possibility of merging.

Future characterisation of the thin-film quality, especially in the regions of the junctions, should preferably be performed by TEM.

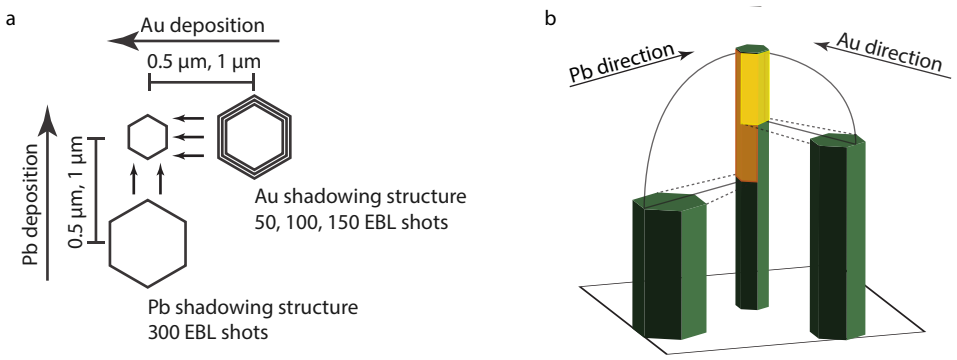


**Figure 5.13:** Overall design principle behind the double deposition strategy. The thin film segment length can be controlled by either changing the height of the shadowing NWs (by changing the number of EBLS) or the distance from the shadowing NW to the main NW. **a.** Top view. In the present work, the distances tried were 500 nm and 1 µm, and the number of EBLS was varied only for the Au shadowing NW, and were 50, 100, and 150 EBLS. The Pb shadowing structure remained at 300 EBLS to obtain a long segment of Pb. The placement of the Pb and Au shadowing NWs with respect to the growth substrate was chosen such that the Pb thin film would cover two facets of the main NW, and the Au layer would cover three facets and overlap one of the Pb covered facets. **b.** Projection view (the nucleating gold cap is hidden for clarity).

## 5.3 In-situ deposited epitaxial Pb and Au contact

In this section we will use the shadow patterning technique to address the experimental challenge of contacting Pb thin films formed on nanowires. Pb possesses the desirable property of having a superconducting phase, able to withstand a magnetic field that is significantly higher than Al. The bulk critical field value of Pb is 8 times higher than Al.[49–51] Because a high magnetic field is useful for controlling Andreev Bound States and because magnetic fields are in general a control mechanism of topological states of matter,[18,52] achieving a significantly higher range of operations is immediately desirable. Futhermore, Pb has a high compatibility with InAs,[20] allowing for an interface with very low strain, so should in principle be an ideal material. Pb however poses an experimental challenge as it is sensitive to ambient atmosphere conditions, and dissolves easily in water. For device fabrication, this means that a Pb thin film may be easily damaged if the device is chemically etched, because the crystalline purity desired of the thin film is unmaintanted. Further, the evaporation of Au contacts after ion milling yields a disordered Au/Pb interface. An ordered metal-metal interface should be expected to yield transport properties superior to disordered interfaces. Previous attempts by our research group have in some cases found no Pb remaining in the sample after the etch procedure. It is a general experience in the research group that etching the thin-film leads to uneven morphology in the etch region. Generally speaking, any etch or contact procedure has a chance of introducing contaminants to the material.

Producing a clean Pb/Au interface however can possibly be achieved using shadow structures to allow in-situ deposition of both the Pb thin film and the contacting Au without breaking vacuum at any step. Besides the main (shadowed) NW, at least two structures are required to create a S-N junction: A thick, short NW will shadow the main NW from one direction, for example allowing the deposition of Pb. A thick, slightly longer to medium length NW will shadow the main NW (including the bottom part of the deposited Pb layer)

such that the top part of the NW (which will be covered in Pb) receives a layer of Au.The Au layer can then be targeted for further contacting with Ti/Au.

### 5.3.1 Design principle

The design produced to achieve this goal is shown in Fig. 5.13, and this was used to produce one batch of InAs/Pb S-N junctions with an in-situ evaporated Au contact to the Pb part. The catalysts are aligned such that Pb will cover two facets, and Au will cover three facets, essentially wrapping around the Pb layer. The Pb shadowing NW is grown from a 300 electron beam lithography (EBL) shots catalyst particle, and will therefore result in a relatively short NW of a considerable thickness. Both the 500 nm and 1000 nm spacing should provide sufficient coverage, but as metal deposition is inherently imprecise, we expect the 500 nm spacing to be optimal. Since alignment of the sample during metal deposition is a concern, it would be beneficial to grow the Au shadowing NW as thick as possible. Naturally a 300 EBLS catalyst particle will result in a Au layer that will overlap the Pb thin film (unless we could somehow place the NWs arbitrarily close to each other without them merging), and even if this was avoided, we wish for a long Pb thin film, so the Au layer should ideally be placed as high up as possible while still being reasonably large for use as a contact. As a compromise between thickness and height, a 50 dot catalyst particle, placed with a 500 nm spacing should result in the Au deposit layer to terminate towards the top of the main NW which would leave a Pb thin film of length 1 µm. The 500 nm spacing should be sufficient to protect the main structure for a small misalignment error during the metal deposition process, while still being a reasonably safe distance away from the main structure to avoid a merge during the growth. Naturally, a combination of catalyst sizes and distances were attempted. The Au shadowing structure was varied by 50, 100, and 150 EBLS, both the Au shadowing and Pb shadowing structures were varied by distances of 0.5 µm and 1 µm. The shadowed NW was varied in EBLS 1, 3, 5, 7, 10, 15, 25 to provide some variance of rigidity. The design was prepared for a deposition angle of 10°.

### 5.3.2 Growth characterisation

The batch was investigated with scanning electron microscopy. In total 264 NWs were investigated, and 78 NWs were identified that fulfilled the goal of the growth, corresponding to a yield of 30%. A NW is considered successful if both metal layers are present, and is otherwise clean of metal in unintended areas. Fig. 5.14 shows a selection of NWs from different variations as acquired by SEM. The Pb shadowing NW is seen to the left in all images and the Au shadowing NW is seen to the right, with the main structure in the middle. The selection displays variations that are in accordance to the design variations, namely we see different lengths of *free* Pb thin film depending on the height and distance of the Au shadowing NW. Fig. 5.14a-e shows a relatively long Au layer, which is suitable for contacting externally. Fig. 5.14c shows a pattern that achieves a long Au layer, by using a slightly thinner, taller Au shadowing NW but distancing it by 1 µm. Fig. 5.14g shows closely spaced NWs, yielding a long Pb section, but sacrificing the length of the Au layer, making it less suitable for deposition of extra contacts. A closer inspection (h and i) also reveals an artifact, which could be attributed to a very thin layer of Au stemming from misalignment to the metal source. The Au shadowing NW was created from the small catalyst particle variant (50 EBLS), yet closely spaced to the main NW.

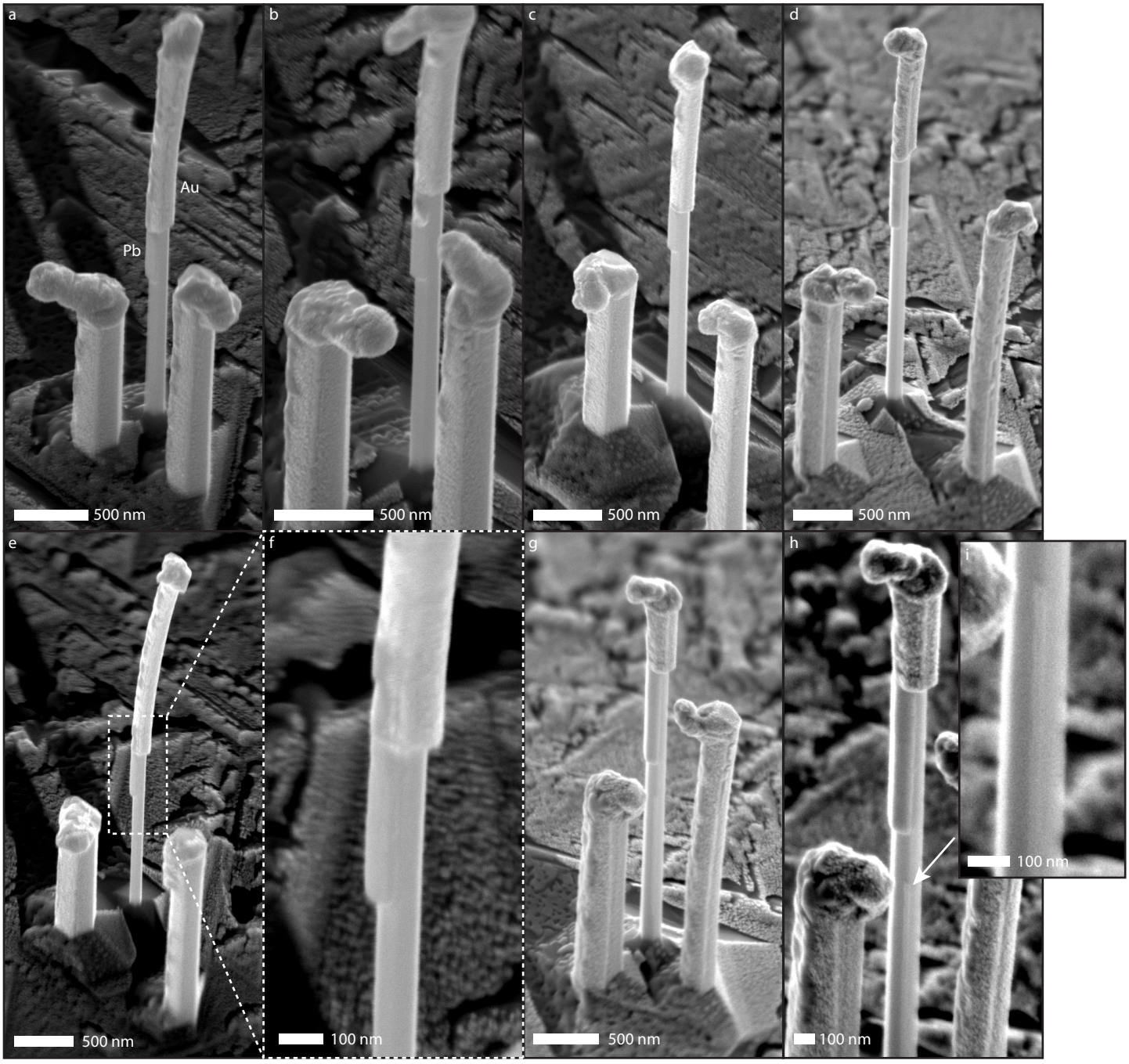


**Figure 5.14:** SEM images of samples produced with the designs displayed in Fig. 5.13. **a.** Structures placed at 500 nm distance, Au shadowing structure grown from 150 single electron beam lithography (EBL) shots. **b.** Pb shadowing NW distanced by 1 µm. **c.** Au shadowing structure grown from 100 EBLS and distanced by 1 µm. **d.** Au shadowing structure grown from 50 EBLS, both Pb and Au shadowing structures distanced by 1 µm. **e.** Au shadowing structure grown from 150 EBLS and distanced by 1 µm. **f.** Zoom-in on marked region in **e**. **g.** Au shadowing structure grown from 50 EBLS and distanced by 500 nm. **h.** High-contrast zoom on structures shown in **g**, displaying an artifact which could stem from misalignment with respect to the Pb shadowing structure, possibly yielding a thin residue of Pb. **i.** Digital zoom on the marked region in **h**.

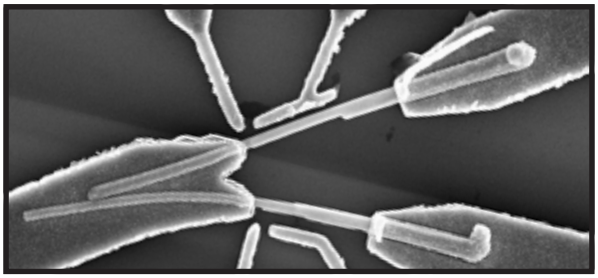

**Figure 5.15:** Two S-N junction devices created from the InAs/Pb-Au shadow batch, showing the two different thin-film lengths that were produced. The top of the NWs are oriented towards the right, evidenced by the thick deposit, being Au. The crossover from Au to Pb can be seen clearly as an abrupt change in layer thickness.

### 5.3.3 Outlook

Evaporation the Au contact in-situ has successfully created Pb-Au interfaces which should, at least theoretically, have much lower disorder than conventionally deposited Au contacts. Further characterisation using transmission electron microscopy would be the next step in strengthening this claim.

The batch presented in this section has been transformed into devices and characterised by other members of our research group, although the transport experiments are still inconclusive at the time of writing. Fig. 5.15 shows an example of two S-N junction devices.

The use of Pb as a semiconductor thin-film in InAs based quantum devices has recently received renewed interest with the display of a hard superconducting energy gap extending above 8.5 T in an epitaxially matched InAs/Pb based device.[20] The shadow approach to contacting Pb could be a step towards improving the materials quality, and thus properties in future devices.

# 6 Electron Transport in InAs/Al Shadow Junctions

In this chapter, we will examine the transport characteristics of a set of selected devices based on InAs nanowires with Al thin-films forming superconducting-normal-superconducting junctions produced using the shadow deposition method. This chapter is divided into two parts, belonging to two different growths. The first growth (reference QDEV897) was produced for single junctions, before the onset of this project, and did not apply specific design schemes. Two devices were produced, fabricated by I-Ju Chen. Data from the best device will be shown, as the other did not exhibit desirable transport properties. The second section shows a device produced from the growth (reference QDEV1018) using the designs described in Sec. 5.2, the 'final' test of the refined shadow deposition technique.

The motivation for studying these shadow junctions stems partly from the fact, that conventional junctions on InAs nanowires formed by chemical etching do not typically display ballistic transport characteristics (Sec. 1). While it is of general interest to create junctions with clean material interfaces, successfully producing ballistic NWs is also part of the step towards realising their proposed role in hosting Majorana bound states (Sec. 1).

## 6.1 Ballistic transport signatures and QPC behaviour in a 100 nm shadow junction

**Internal reference / growth: QDEV897**

The device (depicted in Fig. 6.1) consists of single shadow junction on a InAs NW with a deposited Al layer with a thickness of approximately 20 nm. The junction measures approximately 100 nm in the bare region, and has transition lengths of approximately 30 nm. A (side-) gate is positioned opposite the junction. The device is otherwise gated by a global (back-) gate formed underneath the substrate. Unfortunately, a defect in the southernmost contact resulted in an incomplete connection to the NW. The measurements were therefore performed in a two-terminal configuration, connecting only the northernmost (**S**) and third contact (**D**).

Initially, we will suspend superconducting phenomena by either applying a parallel magnetic field above the critical field strength ($B_C = 10$ mT for bulk Al),[50,53] or operating the device at a temperature above the critical temperature of Al. For pure bulk Al, the critical temperature ($T_{C,Al,bulk}$) is approximately 1.2 K,[50] and the normal state operational temperature was set at 2 K. In future reference to this device we will refer simply to the effective critical field as $B_C$, leaving the thin-film thickness specificity implied. We will assume that the

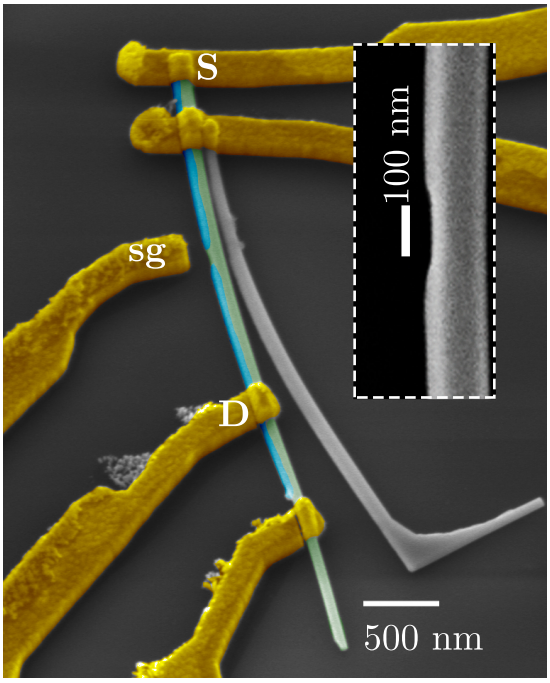


**Figure 6.1:** Pseudo-colour SEM image of the device. Blue: Al, green: InAs, yellow: Au/Ti. Inset: SEM close-up of the junction (acquired prior to contact lithography). Annotations mark the source (S) and drain (D) contacts and the sidegate (sg). The Al layer has an approximate thickness of 20 nm, and the junction length is comparable to the width of the NW. The bottom Au/Ti contact was faulty and therefore the device was operated in a two-terminal configuration.

magnetic field is globally applied, and near parallel to the NW, and we will generally use $B$ to refer to the field strength.

### First look and tuning of the junction potential / the constriction

Operating the device at $T = 29$ mK and at magnetic field $B = 5$ T, we have dispensed any superconducting effects of the cooled metal layer. We first probe the device with a sweep of the global potential barrier using the backgate; six independent measurements are shown in Fig. 6.2a. At zero magnetic field, we expect conductance to increase in a single step, followed by a flat plateau situated at $G = 2e^2/h$, as the characteristic indicator of conductance quantisation and ballistic transport. In our data, where we expect field induced splitting of the plateau into values of $e^2/h$, $2e^2/h$, and $3e^2/h$, the first step occurs in two parts, marked by peaks at $V_{\mathrm{bg}} \sim -2.5$ V and $V_{\mathrm{bg}} \sim -2$ V. These two peak resonances are followed by a plateau at $G \sim 1.4e^2/h$, after which the next step occurs near $V_{\mathrm{bg}} \sim -0.8$ V, and develops into a plateau at approximately $G \sim 2e^2/h$. These steps are not ideal, the peaks indicate some resonant transport at specific Fermi energies, and the slope of the plateau is not a desirable effect. The apparent misalignment of the plateaus will be addressed shortly, but first we will utilise the sidegate to manipulate the potential in the NW and junction.

The sidegate serves to modify the potential barrier in the NW. The size and placement of the sidegate means that a field effect will not only widen or narrow the constriction of the junction, but act akin to the backgate, although the effect is asymmetric (as opposed to the uniformly acting backgate), and potentially strongest near the junction. While these early measurements indicate that the junction is inherently ballistic, altering the NW potential may improve these

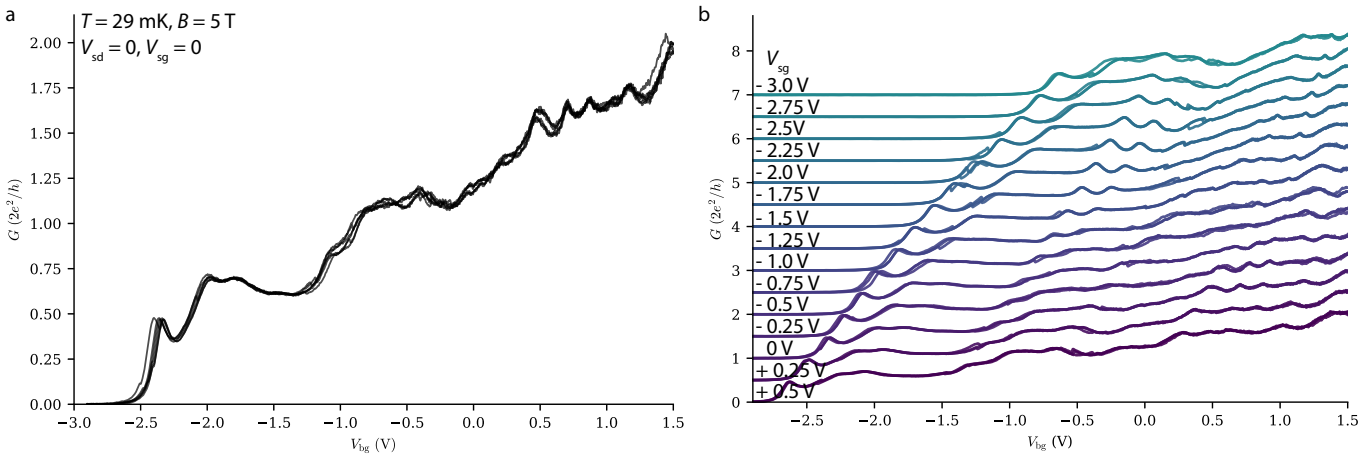


**Figure 6.2:** Raw data of normal state conductance-backgate measurements and example tuning of the sidegate potential. **a.** Raw data of normal state ($T = 29$ mK, $B = 5$ T) conductance-backgate measurements in the native device setup ($V_{\mathrm{sd}} = 0$ and $V_{\mathrm{sg}} = 0$). The staircase pattern signature of ballistic transport and quantum point contact behaviour is repeated in six measurements. To demonstrate the reproducibility, three measurements were performed before any change in the sidegate potential, and three measurements were performed after slowly sweeping the sidegate between $V_{\mathrm{sd}} = [0.5, -3]$ V before going back to $V_{\mathrm{sd}} = 0$. **a.** Conductance-backgate voltage characteristics at different sidegate voltages. Step-like quantized conductance behaviour can be seen at $V_{\mathrm{sd}} = 0$, but increasing the potential barrier of the junction pronounces the features, notably seen as an increase of the step gradient and an increased consistency of the first plateau (maintaining the plateau flatness); up until a certain point. Modifying the constriction ($V_{\mathrm{sd}} < 0$) also reduces the gate voltage space at which the device can be operated. Each sweep is repeated three times.

features, and without the use of the global backgate, the sidegate itself may be used to close off and open the device. Fig. 6.2b shows repeated measurements of conductance vs. backgate for sidegate voltages in the range $V_{\mathrm{sd}} = [0.5, -3.0]$ V in increments of 0.25 V.[i] As can be seen from Fig. 6.2b, changing the local junction potential also changes backgate operating ranges. As the barrier is increased ($V_{\mathrm{sg}} < 0$), the first plateau becomes more well defined, and the step itself slightly sharper. From these measurements, a sidegate voltage in the range -1.75 V to -2.25 V appears viable. Having explored the ranges of interest for the sidegate in the millikelvin regime, the external magnetic field was reduced to 0, and instead temperature was increased to $T = 2$ K.

### Raw data of normal state, zero-field measurement

Fig. 6.3 shows a raw data sweep of the conductance-backgate characteristic measured at $T = 2$ K, zero magnetic field, and without an applied bias voltage. The device is pinched off below $V_{\mathrm{bg}} < -2.5$ V, and a step increase to a resonance peak occurs at $V_{\mathrm{bg}} \approx -2$ V, which develops into a plateau, situated around $\sim 0.7G_0$, in the range $V_{\mathrm{bg}} = [-1.9, -1]$ V. The basic trend is similar to the $B = 5$ T measurements just described. Naturally, without the field induced splitting. These measurements are presented without taking into consideration the resistance inherited from the lithographically defined contacts, thus we are not measuring the intrinsic conductance of the device itself, but a sum of the contact resistances and the device resistance. In the following sub-section we will briefly describe the assumptions about the device and how we may take the contact resistance into account.

[i] Repeated for both backgate up-down sweeps, and sidegate up-down sweeps.

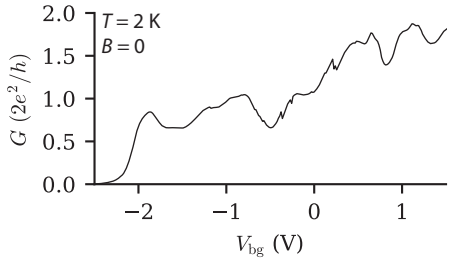


**Figure 6.3:** Normal state raw conductance-backgate characteristic at zero bias voltage and zero magnetic field, measured at $T = 2$ K.

#### Series resistance of the contacts

The data described so far may convince us that a QPC-like behaviour can be established in the device. While the series resistance of the cryostat has been calibrated before data treatment, we have not considered the resistances of the lithography defined contacts and the potential resistance between these leads and the nanowire. The defect in the southernmost contact, while left floating, could contribute some unknown resistance value, although in all likelihood of negligible magnitude as the drain contact is in direct extension of the device. This defect however obfuscates the resistance of the active drain contact (**D**), by hindering a direct measurement of the series resistance between the two southern contacts.

The device is further complicated by the adjacent NW connected to the second northern contact. Due to the aforementioned defect, this contact was left unconnected, and in principle is not expected to influence the characteristics of the device; yet it is not possible to reject with absolute certainty that some capacitance effect may occur.

The contact resistance between the two closely spaced northern contacts was probed at T = 2 K and zero magnetic field, by measuring the conductance-backgate characteristics at zero source-drain bias, and by measuring the conductance versus source-drain characteristics at zero backgate voltage. From the measured conductance (shown in Fig. 6.4a and b) there appears to be some gate dependency, which may indicate some conduction through the semiconductor rather than the metal (likely due to the thinness of the metal layer), and although small it is not entirely negligible. The approximate resistance is $R_S \approx 0.05h/e^2 = 1.36$ kΩ (extracted from the measurements in Fig. 6.4b). Subtracting this resistance alone (as shown for $B = 5$ T in Fig. 6.4c) does not change the data much, and does not produce a satisfying conductance curve, and perhaps neither should it be expected to, not only because there is likely some variation in each individual contact, but also because we are now neglecting the resistance of the bottom (working) contact. Alternatively, since the conductance plateau is well defined (mostly so for $B = 5$ T), we may fit the series resistance to be subtracted in a manner that minimizes the difference between the first conductance plateau and a value of exactly $2e^2/h$. Such a fit yields series resistance $R_S = 4591$ Ω ($\pm 219$ Ω). All data presented hereon has been corrected for a series resistance corresponding to the fitted $R_S = 4591$ Ω unless explicitly stated.

### 6.1.1 Zero- and non-zero field normal state measurements

Fig. 6.5 shows three series resistance corrected normal state ($T = 2$ K) $G$-$V_{bg}$ traces at zero field and at parallel magnetic fields of 1 T and 5 T. Correcting for

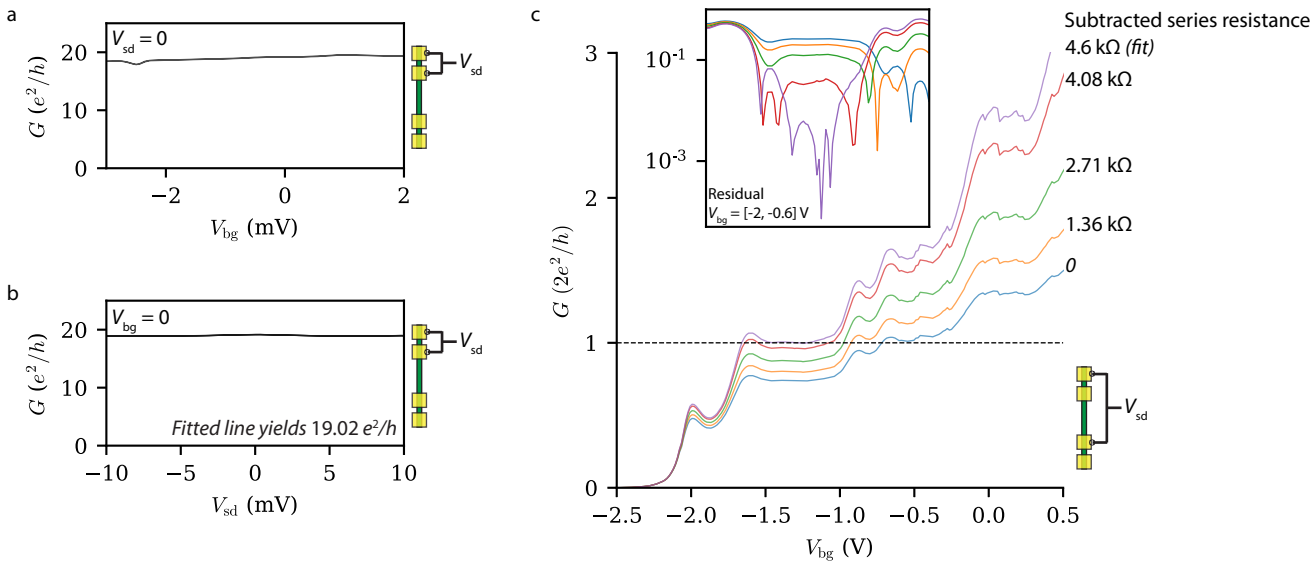


**Figure 6.4:** Calibration of the contact series resistances. **a.** Conductance-backgate traces between the two northern contacts at zero bias voltage (repeated two times). **b.** Conductance-bias voltage traces between the two northern contacts at zero gate voltage (repeated four times). The line was fitted to yield an offset of $19.02e^2/h$, corresponding to a measured series resistance $R_{S,\text{measured}} = 1.36$ kΩ. **c.** Calibration of the series resistance to the $G = 2e^2/h$ plateau. Subtracted values are as follows: Blue: Raw data without calibrated resistance. Orange: 1.36 kΩ ($R_{S,\text{measured}}$), Green: 2.71 kΩ ($2R_{S,\text{measured}}$), Red: 4.08 kΩ ($3R_{S,\text{measured}}$), Purple: 4.59 kΩ (the fitted series resistance). Inset: residual to $2e^2/h$ within the range $V_{\text{bg}} = [-2; -0.8]$ V. The data in **a** was recorded in the normal state at $T = 2$ K without applied magnetic field. The data in **b** was recorded in the normal state by applying a magnetic field $B = 5$ T.

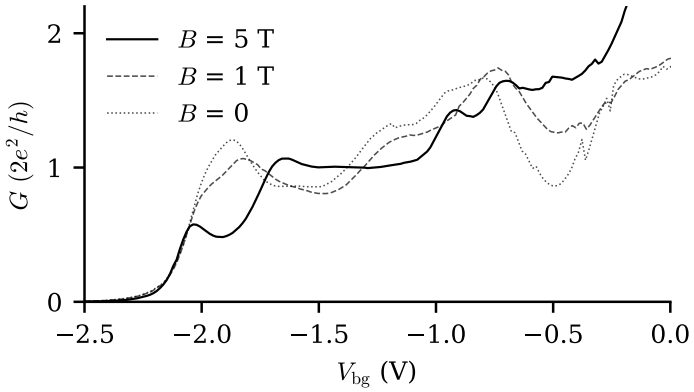


**Figure 6.5:** Differential conductance $G$ vs backgate voltage $V_{\text{bg}}$ for zero and non-zero magnetic field, at temperature $T = 2$ K. Source/drain bias $V_{\text{sd}} = 0$, $T = 2$ K, magnetic field $B = (0, 1, 5)$ T. The $B = 5$ T measurement has been aligned along $V_{\text{bg}}$ in post-processing. The transmission resonances near the $G = 2e^2/h$ plateau is suppressed by the magnetic field, and a new step emerges at $G = e^2/h$. Data corrected for series resistance. The $B = 0$ trace is the corrected data otherwise used in Fig. 6.3.

series resistance results in a steeper step gradient. Correcting the series resistance *fixes* the misalignment of the $G_0$ plateau, and correctly aligns the $0.5G_0$ and the $1.5G_0$ plateaus to their expected values. The ballistic transport features, notably the single step up to a plateau value, and the maintained plateau over a certain gate range is generally consistent for all three measurements, up to a gate value of $V_{\mathrm{bg}} \sim -1$ V, where the $G$ increases, only for the $B = 0$ and $B = 01$ T traces to drop in $G$, ideally these should maintain the conductance value of $G = G_0$ until a new step to $2G_0$ would occur. Resonances in the conductance at lower $B$ (0 and 1 T) can be attributed to the fact that the Ti/Au leads are not necessarily[i] adiabatically coupled to the NW; non-zero reflection probability at the interface between the leads results in backscattering which, when coherent, changes the conductance behaviour in a systematic fashion. The higher magnetic field (5 T) suppresses this coherent backscattering, leading to an apparant stabilisation of the $G_0$ plateau.

### 6.1.2 Bias spectroscopy

As changing the backgate voltage is closely related to changing the Fermi energy in the device, and changes in voltage bias is equivalent to changing the chemical potentials at the source/drain contacts (the two ends of the 1D channel), measuring the conductance as a function of both gate voltage and voltage bias provides insight into the energy structure of the device. Such bias spectroscopy was performed at $T = 2$ K, at the magnetic field strengths $B = (0, 1, 5)$ T (Fig. 6.6). The data is visualised such that each line represents a $G$-$V_{\mathrm{sd}}$ trace performed at a different $V_{\mathrm{bg}}$. The ascension of lines reflect increasing backgate voltage along with the resulting increase in conductance, consistent with an *opening* of the device. Large spacing in conductance is observed when the conductance gradient is large, and bundling of lines occur in stable regions, or plateaus, in the conductance. In this manner, the bias spectrum becomes an analogue of the energy band structure, with plateaus linked to the sub-bands in the structure. For comparison, refer back to the theoretical saddle point potential QPC model bias spectrum shown in Fig. 2.5 (Sec. 2.1), showing the $(0.5, 1, 1.5, 2, 2.5)G_0$ sub-bands. At zero field (Fig. 6.6a), two features are identifiable: the $2e^2/h$ plateau, occurring at $V_{\mathrm{sd}} \sim 0$ (slightly obscured by resonant behaviour), and the formation of a half-plateau ($G = e^2/h$) in the bias range $|V_{\mathrm{sd}}| \gtrsim 4$ mV. Raising the magnetic field to $B = 1$ T reduces the resonance peak somewhat, while maintaining the aforementioned features. At $B = 5$ T (Fig. 6.6c), spin splitting takes effect, and splits the zero-bias $2e^2/h$ plateau as well as finite bias $e^2/h$ plateau. The values of the split finite bias plateaus are not situated perfectly, but roughly correspond to $0.5e^2/h$ and $1.5e^2/h$.

Mapping $V_{\mathrm{bg}}$ and $V_{\mathrm{sd}}$ to the $G$ in a colourmap allows for inspection of the bias voltage dependent energy spacing of conductance levels. An example is shown in Fig. 6.7a, displaying the $B = 5$ T bias spectrum. The resulting patterns (diamond structures) provide useful information, as the intersection of pattern edges (thusly called diamond tips) correspond directly to the energy spacing of the sub-bands in the energy structure, with $\Delta\epsilon_{i,j} = eV_{\mathrm{sd=0,sd=tip}}$ being the energy spacing between sub-bands $i$ and $j$. The lever arm $\alpha_g = \frac{V_{\mathrm{sd}}}{\Delta V_{\mathrm{bg}}}$ can be extracted from the energy spacing and the gate voltage range of a plateau, which allows transforming the gate voltage spectrum into units of energy.[29] Fig. 6.7b shows the transconductance ($\mathrm{d}G/\mathrm{d}V_{\mathrm{bg}}$) of the same colourmap, mainly as a

[i] and in fact, highly unlikely

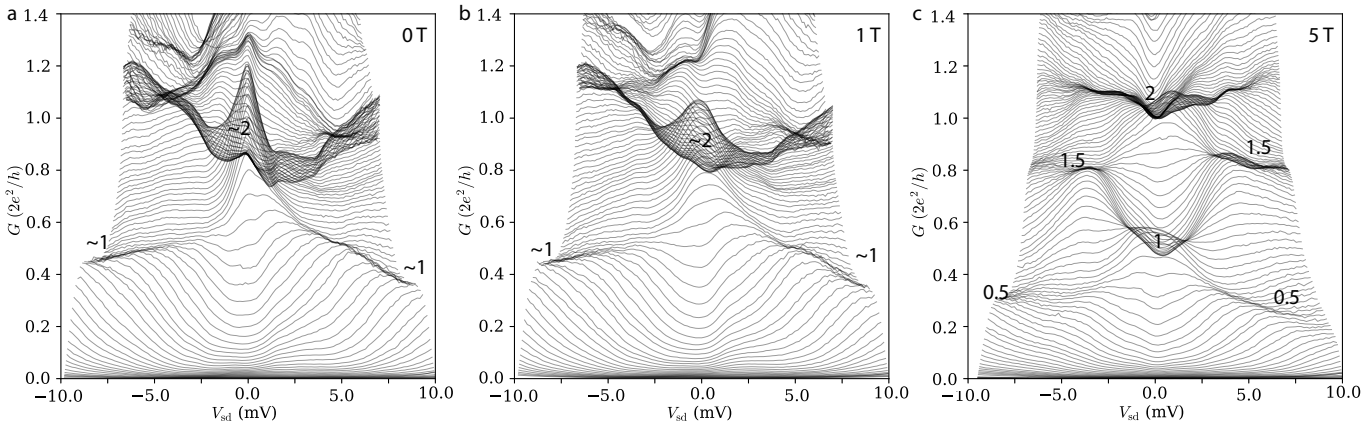


**Figure 6.6:** Bias spectroscopy recorded at $T = 2$ K. **a.** $B = 0$. **b.** $B = 1$ T. **c.** $B = 5$ T. Each line represents a $G - V_{sd}$ trace at a fixed $V_{bg}$ value. Lines bundle together where plateau would form in a standard $G - V_{bg}$ plot, and are thus indicative of a channel being filled (or rather, a new mode appearing). The $2e^2/h$ plateau and the sub-bands are split into different levels by the magnetic field at $B = 5$ T.
Annotated values are in units of $e^2/h$. Data corrected for series resistance.

visual aid,[i] the gradient shows the step-like behaviour in a clear manner, with $\mathrm{sd}G/\mathrm{sd}V_{bg} = 0$ corresponding to plateau areas. Extracting the sub-band spacing from the transconductance yields sub-band spacings of roughly $\sim 10$ meV and $\sim 5.5$ meV from the $2e^2/h$ and $Ne^2/h$ plateaus respectively.

Fig. 6.8 shows a colourmap representation of the zero field data in a longer backgate range, here the first zero bias plateau as well as finite bias plateaus are clearly visible in the transconductance Fig. 6.8b, but it becomes clear that resonances make a trace at the higher conductance values difficult.

### 6.1.3 Magnetic field induced peak splitting

So far we have presented data including measurements made with an external magnetic field, we have however not addressed a fundamental feature; the Zeeman energy splitting, which (in our data) presents itself as a separation of the $N = 1$ peak into a lesser peak, occurring prior to the $N = 1$ step, and a *normal* $N = 1$ step (see Fig. 6.5 for example). As mentioned previously, a signature of the Zeeman splitting is also seen as the formation of a new set of (quarter-) plateaus in the $B = 5$ T bias spectrum (Fig. 6.6c).

Fig. 6.9 shows the recording of the conductance as a function of $V_{bg}$ and $B = [0, 5]$ T, performed at $T = 29$ mK, thus allowing us to directly observe the Zeeman energy splitting. Fig. 6.9a shows superconducting effects being fully suppressed around $B \geq 500$ mT at which peak splitting becomes evident. The first resonance peak around $V_{bg} \sim -1.1$ V presents the most obvious splitting, and allows a direct observation of the effect. At higher conductance levels, the effect is less distinct; the second resonance peak ($V_{bg} \sim -0.25$ V) is broadened by a shoulder feature (more clearly seen in Fig. 6.11a), and the peaks $B$-dependent peak splitting is difficult to trace to the same origin point; at the same time there appears to be some charge induced change in the backgate space, evident by the sudden peak position change at $B = (1.4, 3.1)$ T, hindering the emergence of a clear pattern, though it is obvious that some field dependent splitting occurs.

[i] Subtracting the linear conductance increase may also be a viable method, although in this case it was not preferable. Appendix section 8.1 shows examples of this procedure demonstrated on the data shown here.

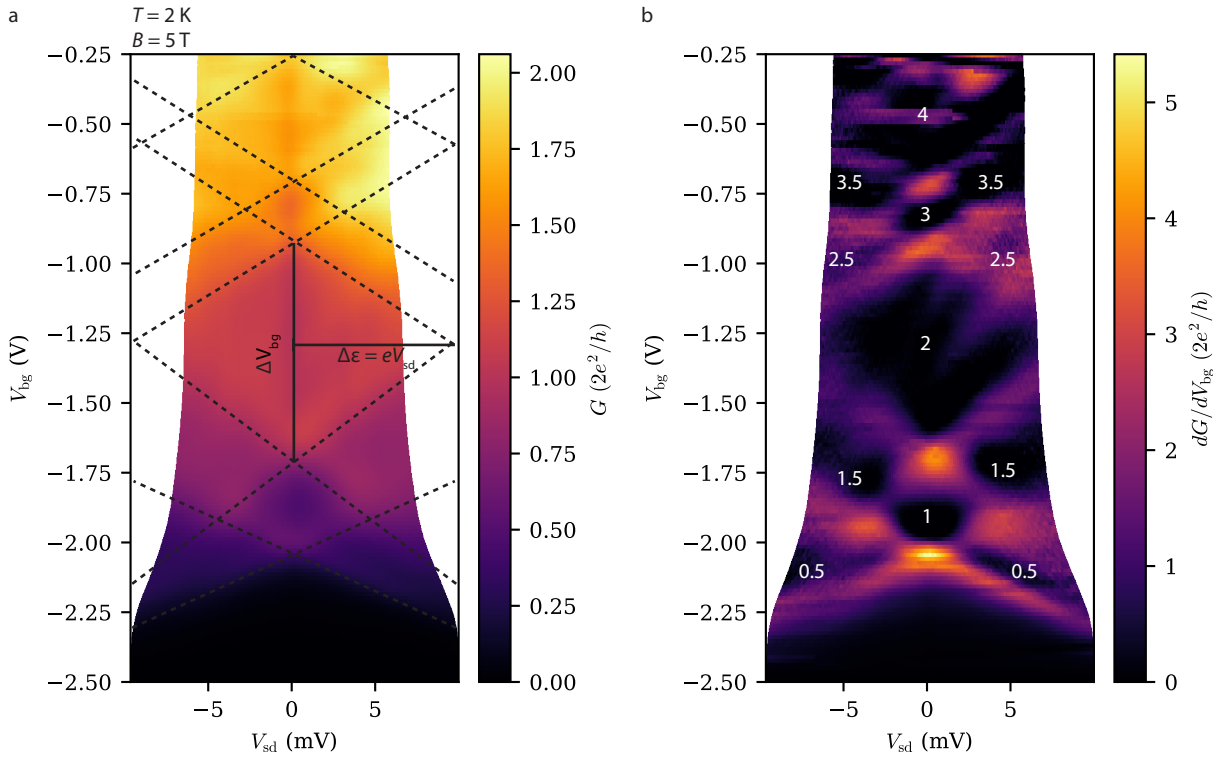


**Figure 6.7: a.** Colourmap representation of the bias spectrum recorded at $B = 5$ T (Fig. 6.6c), truncated to the range $V_{\mathrm{bg}} = [-2.5, -0.25]$ V. Dashed lines input in as a visual aid and were extracted following the contours of the transconductance ($\mathrm{d}G/\mathrm{d}V_{\mathrm{bg}}$). The resulting pattern, called a diamond structure, more readily displays the width of plateaus as a function of $V_{\mathrm{sd}}$. The tips of the diamond align with the sub-bands of the energy structure, and the energy spacing between sub-bands $i, j$ can be extracted directly from the bias voltage readout at the tip: $\Delta\epsilon_{i,j} = eV_{\mathrm{sd,tip}}$. **b.** Transconductance of the bias spectrum. The annotated values represent the conductance values in units of $e^2/h$. Date corrected for series resistance.

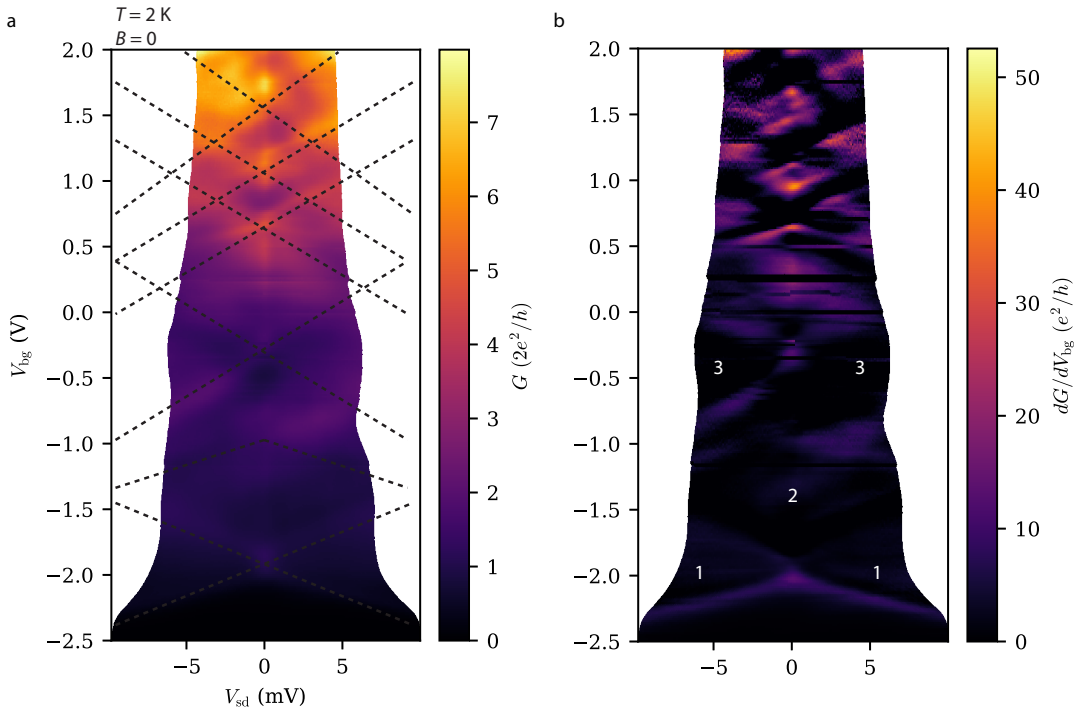


**Figure 6.8: a.** Colourmap representation of the normal state, zero-field bias spectrum recorded at $T = 2$ K, displaying a longer backgate range. Dashed lines are drawn from the transconductance and are meant as a guide to the eye, drawn from **b.** Transconductance of **a**. Annotated values are in units of $e^2/h$, and are set in as a guide corresponding to expected values of the conductance plateaus. The finite bias $e^2/h$ plateau and zero bias $2e^2/h$ plateaus can be seen clearly in the transconductance, but the location of the higher conductance value plateaus becomes more difficult to trace accurately.

At $V_{\mathrm{bg}} \sim 0.9$ V two clearly distinct peaks appear, but they become difficult to trace at $B \sim 1$ T, even appearing to split once again, though the signal is smeared. They seem to reappear at $B \sim 3$ T following their original pattern. These signals are too diffusive to clearly trace, but if one suggests that a linear line follows each of them then they closely resemble the Zeeman effect, although they will not originate from the exact same point.[i]

Analysis of the peak resonance positions (Fig. 6.10a and Fig. 6.11a) shows that the $V_{\mathrm{bg}} \sim 0.9$ V peak is neighboured by a resonance at $V_{\mathrm{bg}} \sim 1.1$ V, and this could account for crossing of the peak splitting lines, making a clear distinction difficult, especially given the smeared appearance of the signal.

**Extraction of the effective $g$ factor**

Fig. 6.9c shows a zoom on the region of interest for the first resonance peak; an ad hoc peak finding algorithm was produced to extract the $V_{\mathrm{bg}}$ position of each conductance peak, marked with white dots. The $V_{\mathrm{bg}}$ distance between each peak is converted to energy $E$ via the lever arm (extracted from Fig. 6.7) and each point as a function of magnetic field is shown in Fig. 6.9d. Fitting the points in Fig. 6.9d to Eq. (2.11) yields an effective $g$ factor of $\sim 17$, which is 13 Enhancement of the effective $g$ factor beyond the bulk value has been reported for NW based systems composed of InAs/Al, with values of for example 18,[41], 20,[6,40] 23.[6] and 50.[6]

It is expected that spatial confinement reduces $g^*$, and numerical studies have shown the NW diameter range where enhancement of $g^*$ is strongest to lie in the range 10-100 nm after which enhancement increases only marginally.[54] The NW in our device has a diameter just slightly above 100 nm, so an effective $g$ factor above bulk value is not unexpected.

**Effective $g$ factor at higher conductance**

Subtracting the linear background increase in conductance as a function of $V_{\mathrm{bg}}$ allows the peaks to stand out more clearly in a manner resembling the signatures of the transconductance spectrum, Fig. 6.10 shows the $G$ vs $B$ vs $V_{\mathrm{bg}}$ dataset with the linear background subtracted from each trace along the $V_{\mathrm{bg}}$ axis; Fig. 6.10a is divided into two parts with two different colourscale ranges, to avoid saturating the the SC region or underexposing the normal state region, thus we can see more clearly the origin point of the split peaks, and the splitting around $V_{\mathrm{bg}} \sim 0.9$ V (dashed lines in Fig. 6.10a) can more easily be traced.

If we assume that the split peaks at $V_{\mathrm{bg}} \sim 0.9$ V can be traced linearly then the more smeared spectrum at higher magnetic fields becomes less influential, and we can use the low field area which roughly produces the dashed lines indicated in Fig. 6.10b. Fig. 6.10c shows these lines as a function of $B$ with the $V_{\mathrm{bg}}$ axis converted to energy $E$ (normalised to originate at zero) via the lever arm extracted previously. Fig. 6.10d shows these lines compared to the $N = 1$ peak data extracted previously, with a straight line fitted to each point; coincidentally these lines do not originate perfectly at zero energy either, instead bearing a highly similar separation at $B = 0$. Fig. 6.10e shows the Zeeman energy splitting $\Delta E_z$ as a function of $B$ for both the $N = 1$ and the $V_{\mathrm{bg}} \sim 0.9$ V lines, the green line being the fit from Fig. 6.9d with $g^* = 17.3$ and the black line being the numerical difference between the traced lines, with a proportionality consistent with $g^* = 12.6$.

If we regard the higher field area of the spectrum then a line is clearly visible in the region between the two split peaks, or indeed it can be regarded as sitting

[i] A closer look at this is provided in the appendix Sec. 8.1 Fig. 8.3

| $V_{\mathrm{bg}}$ | $g^*$ |
|---|---|
| $-1.1$ V | $\sim 17$ |
| $+0.9$ V | $\sim 13$ (or $\sim 10$)[ɬ] |

**Table 6.1:** Effective $g$ factors extracted at different backgate voltages. Data and procedure shown in Fig. 6.9 and Fig. 6.10. [ɬ]Depending on the method used.

right in the same gate-energy space as the lower $V_{\mathrm{bg}}$ peak; tracing the peaks with this line would result in a lower effective $g$ factor, but would fit poorly with the data in the lower field region. Indeed, if we follow the trace from high field towards low we can see that what begins as a noticeable peak turns into a valley in the range $B \sim [1.5, 3]$ T. The same seems occur for the secondary peak, although the valley seems to lie at a marginally higher gate voltage than the trace would suggest. Extracting the peaks via the naïve approach and fitting the difference in energy spectrum yields $g^* \sim 10 \pm 1$, the additional data showing extracted peaks and fits are shown in appendix section 8.1).

We have extracted two different effective $g$ factors, at two different backgate voltages, $V_{\mathrm{bg}} = -1.1$ V: $g^* \sim 17$, and $V_{\mathrm{bg}} = +0.9$ V: $g^* \sim 13$ (or $\sim 10$ depending on our method).

The gate voltage dependency of $g^*$ has been shown in recent studies to be tuneable, yielding values between 2-22.[38,41,42] This tuneability of $g^*$ has been shown to be randomly linked to the backgate voltage;[38,41] there is thus no expectation that increasing or decreasing the gate voltage should yield a proportional response in $g$.

### 6.1.4 Second order transition from superconducting to normal state behaviour in the parallel magnetic field

Under application of a magnetic field, we expect a bulk superconductor to switch from superconducting phase to normal state in a discontinuous fashion; a sudden jump in resistance, when the critical field is reached. For a thin film superconductor, this transition has been known to change in a smoother, second order transition manner when subjected to a perpendicular field.[55] A second order transition is possible to observe in the parallel orientation as well. At $T = 29$ mK, by decreasing the parallel field strength in small increments of 50 mT, we observe the reemergence of the superconducting phase at $B < 500$ mT and its enhancement as $B \to 0$. Fig. 6.11a shows stacked conduction curves as a function of $V_{\mathrm{bg}}$ taken in the range $B = [0, 5]$ T. The graph is normalised to $B$, each line being offset by 50 mT. The conductance-backgate characteristics feature large amplification of the peak resonances, which subside as the field is increased. To better observe the transition characteristic, the peak value of the first and second resonance can be mapped as a function of the magnetic field. The resonance peaks are extracted using a boolean `AND` mask to limit the $V_{\mathrm{bg}}$ range of interest combined with `max` filtering of the conductance values, the procedure is shown in the appendix section 8.1. Fig. 6.11b shows the first 15 gate space traces, offset by the magnetic field at which they were recorded with the first two resonance peaks as well as the first plateau highlighted. Fig. 6.11c shows the conductance value of the extracted values for each conductance-backgate trace as a function of the magnetic field strength. The transition can be said to occur at$\sim 450$ mT and $\sim 400$ mT, for the first and second resonance respectively, as shown in the derivative values in Fig. 6.11d. At $> 550$ mT (the vertical dashed line in Fig. 6.11d) the effect has been fully suppressed.

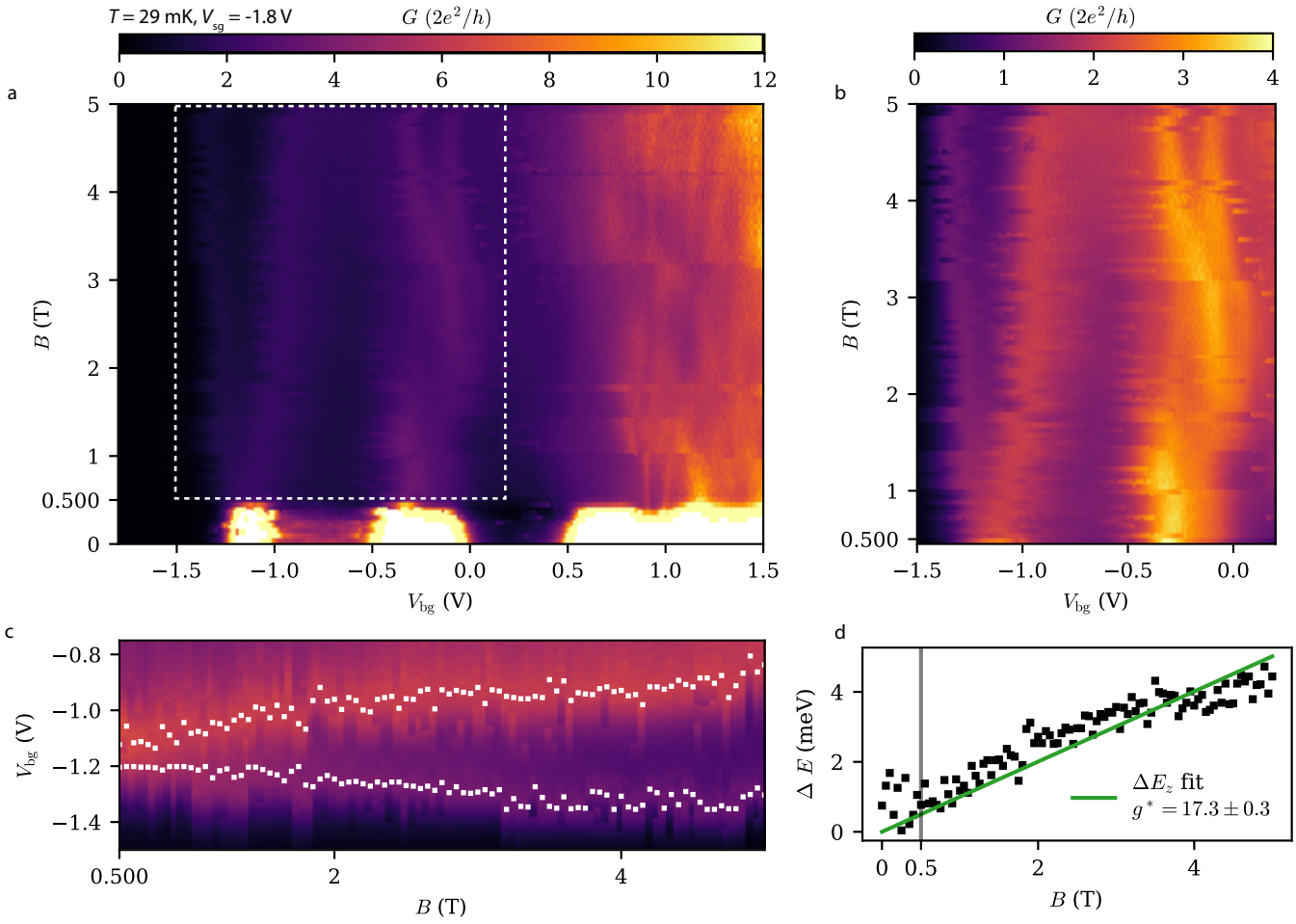


**Figure 6.9:** Magnetic field induced suppression of supercurrent effects, Zeeman energy splitting, and extraction of the effective $g$ factor. **a.** Backgate voltage $V_{\mathrm{bg}}$ sweeps as a function of magnetic field $B$. Supercurrent effects are suppressed at $\sim 500$ mT, at which peak splitting begins to become noticeable. The first resonance peak is situated around $V_{\mathrm{bg}} = -1.1$ V and is the most obviously split peak. The second resonance peak ($V_{\mathrm{bg}} = [-0.5, 0]$ V) features a shoulder (see perhaps Fig. 6.11) with the peak splitting being less clear. Around $V_{\mathrm{bg}} \sim 0.9$ V and $B = 0.5$ T two clearly distinct peaks that appear to originate from the same point can be noticed, they can be followed to around $B \sim 1$ T where they become diffusive; and it appears as if the first peak splits again. Around $B \sim 3$ T the peaks can be picked up again, following the pattern they originally had between $B = [0.5, 1]$ T. **b.** Zoom-in on the dashed area in **a**, with a more saturated colourscale. **c.** The range of interest of the first resonance peak and the result of an ad hoc peak extraction algorithm (white points). **d.** The difference between each point extracted from **c** as a function of magnetic field $B$, converted to energy $E$ via the lever arm extracted from Fig. 6.7, and fitted to the Zeeman energy via Eq. (2.11) yields an effective $g$ factor slightly above the bulk value (15 for InAs). The vertical grey line indicates the boundary $B < 450$ mT where the extracted peaks are less consistent due to the device being in the superconducting regime; setting the lower bound on the fitting data to this line does not change the outcome of the fit. Data corrected for series resistance.

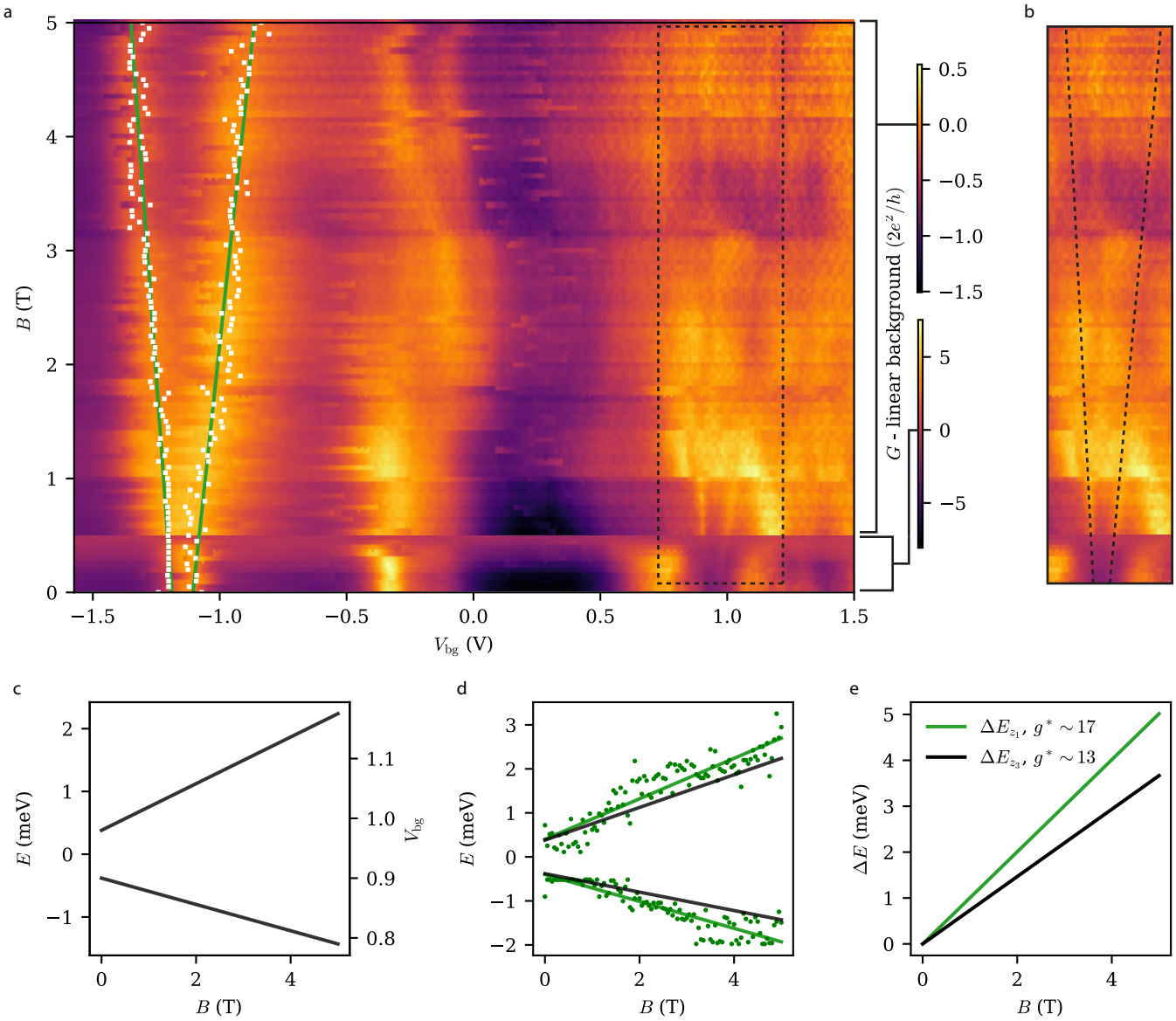


**Figure 6.10:** Linear background subtracted data shown in Fig. 6.9. The linear background of each $V_{\mathrm{bg}}$ trace has been subtracted, and the superconducting region ($B < 450$ mT) is shown with a different colour range than the normal region. **a.** Background subtracted colourmap from Fig. 6.9 shows more clearly the resonance peaks in the superconducting region, consistent with the values shown in Fig. 6.11. The colour scale is individualised for the superconducting- and the normal state regions to better show the entire dataset without saturating or underexposing any particular region. The white dots correspond to the peaks extracted in Fig. 6.9c and the green lines are the best fit to each set of dots. **b.** Attempt at tracing the split peaks within the area marked by dashed lines in **a**. **c.** The trace in **b** converted to energy $E$ via the lever arm extracted from Fig. 6.7. **d.** The same trace as **c** compared to the green lines (and related dots) extracted from the first split resonance peak. **e.** Fitted Zeeman energy splitting of the traces from **b** compared to the fitted data of the first split resonance.

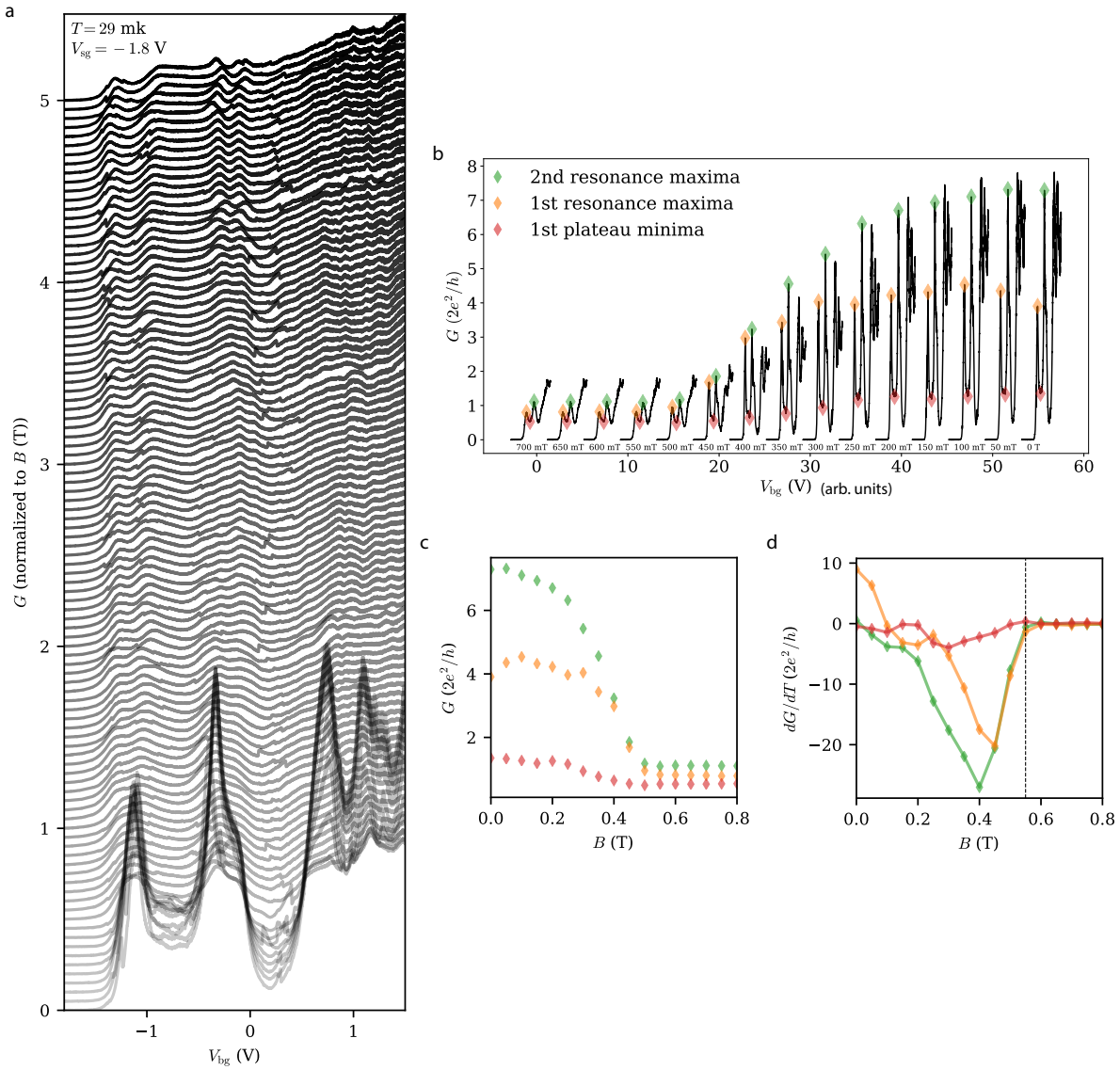


**Figure 6.11:** Suppression of supercurrent effects at high magnetic fields. **a.** Low temperature gate-conductance characteristics at magnetic fields from 0 to 5 T, recorded in steps of 50 mT. **b.** $G$ as a function of $V_{\mathrm{bg}}$, offset by $-B$ in the range $V_{\mathrm{bg}} = [-2.8, 1.5]$ V. The resonance peaks (marked) are extracted using an ad hoc algorithm. **c.** Extracted peaks of the first two resonance maxima, and the first plateau minimum plotted as a function of magnetic field $B$, showing a second-order transition from the superconducting state to the normal state and suppression of supercurrent at $B < 500$mT. **d.** Derivative of the peaks in **c**. Vertical dashed line marks $B = 550$ mT. Data recorded at $T = 29$ mK, $V_{\mathrm{sg}} = -1.8$ V. The appendix section 8.1 contains the steps from **b** to **c** and an extended version of **e** showing the absolute residual to 0 for the entire spectrum $B = [0, 5]$ T. The data is not corrected for series resistance, as displaying the SC regime would otherwise be unmanageable.[F]

[F] For example, the conductance of the $B = 350$ mT measurement shown in **b** goes from $8G_0$ to $80G_0$ with the subtraction of only the previously measured series resistance. Using the fitted value it *measures* above $4000G_0$.

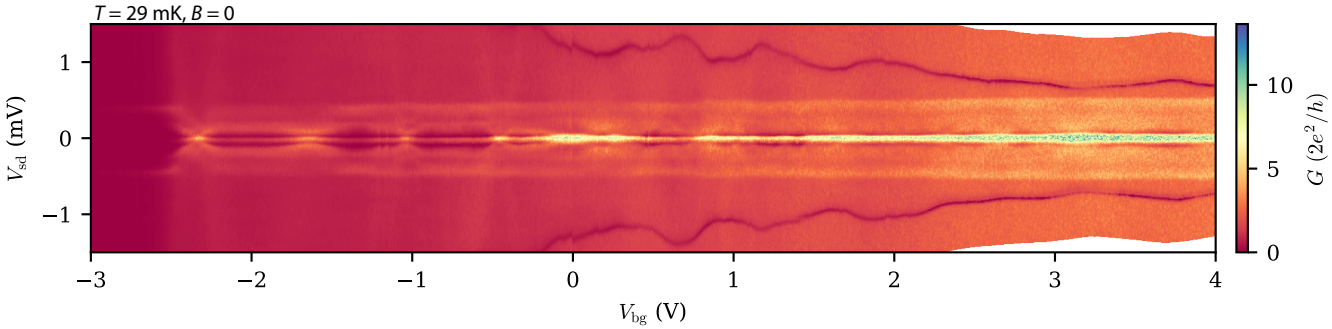


**Figure 6.12:** Superconducting regime bias spectrum shows formation and maintenance of a ZBP.

### 6.1.5 Superconducting regime

So far, superconductivity has been a phenomena we have suppressed, and while it is not the primary focus, we will end this section with a low temperature, zero field bias spectrum, to show that the junction exhibits some desirable properties related to hybrid devices, namely signatures of Andreev bound states, including a persistent zero bias peak. As the device could not be operated in a 4-terminal configuration, the measured values are likely not representative, and the measurements thus constitute purely a qualitative description. Fig. 6.12 shows a broad range gate sweep, with the onset of conductance around $V_{\mathrm{bg}} \sim -2.5$ V, marked by the formation of Andreev reflection (AR) signatures in the finite bias regime that evolve into a zero bias peak which persists throughout the entire spectrum.

### 6.1.6 Summary

In this section we have characterised an InAs/Al NW based device with a junction of approximately 100 nm, formed by shadow deposition. We have demonstrated basic quantum point contact behaviour, namely conductance quantisation, demonstrating relatively clean behaviour of a single channel regime. We have extracted the effective $g$ factor ($\sim 17$ and $\sim 13$) and shown, in agreement with recent studies,[38,41,42] that it is sensitive to changes in the backgate voltage. Finally, we have probed the superconducting regime in two ways, first we demonstrate a second order transition, and conclude that the device transitions to the normal state completely at $B \sim 550$ mT, which puts the device critical field $B_C$ somewhere between 450-550 mT, depending on definition, which is 6-7 times larger than similar, epitaxial thin-film devices,[16] and 4-5 times larger than the $B_C$ for bulk Al.[50,53] Secondly, bias spectra shows the formation of the superconducting gap, and the formation of a persistent zero bias peak.

## 6.2 Transport features in a 350 nm shadow patterned junction

**Internal reference / growth: QDEV1018**

This section features a device based on a NW produced using the multiple junction designs presented in Sec. 5.2. Although several devices were produced, some of which are at the time of writing awaiting transport experiments, I have selected the best performing device, in terms of the sought QPC behaviour.

The device is depicted in Fig. 6.13. It consists of an InAs NW with an in-situ deposited, thin-film epitaxial layer of Al (thickness $\sim 25$ nm), contacted

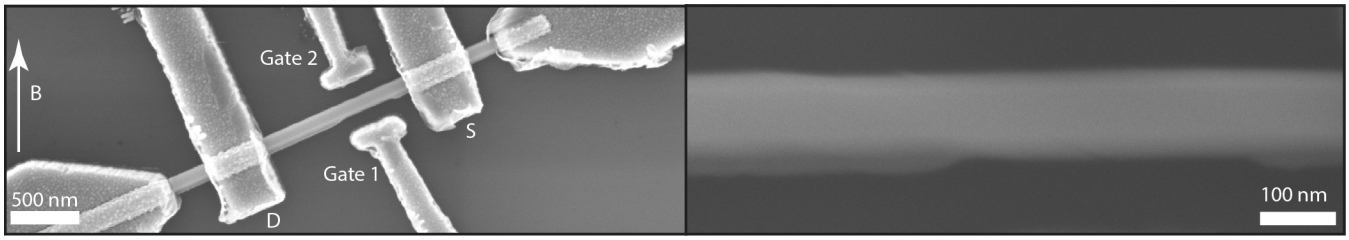


**Figure 6.13:** Left: SEM of the device. InAs NW with half-shell Al thin-film with a film thickness of roughly 25 nm. The junction length measures $\sim 350$ nm, circa 3.3 times the width of the NW. Two side gates (Gate 1 and Gate 2) control the junction potential. One of the outer contacts was defective, and it was therefore run in a 2-terminal configuration using the inner contacts, marked S (source) and D (drain). The arrow pointing north indicates the direction of the magnetic field $B$. Right side: SEM close-up of the junction and the Al film seen as a contrasting layer, taken after the transport experiments were concluded.

to four Ti/Au probes (of which three were functional). The junction was made according to the design principles described in section 5.2, and the NW is part of the experimental growths produced during this project. The junction is relatively long, with a length of $\sim 350$ nm corresponding to approximately 3.3 times the NW thickness. The junction potential is locally controlled by two side gates. Unfortunately, faults during the bonding of the device resulted in an uncontacted backgate, disabling possible manipulation of a global chemical potential. Due to the faulty contact, the device was operated in a 2-terminal configuration, using the two inner probes denoted S and D in the SEM. The magnetic field direction is indicated on the SEM, and as can be seen, the junction experiences both a parallel and a perpendicular component, which are estimated to be $B_{||} \approx 0.423B$ and $B_{\perp} \approx 0.906B$.

The normal state properties of the device are tested at a temperature of 2 Kelvin. At 0 gate voltage, the device has a base conductance of roughly $G_0$. Fig. 6.14 shows the pure gate-conductance characteristics of the device, recorded at magnetic fields between 0 and 7.5 T. The first plateau is distinct, especially at a field of 1 T (Fig. 6.14b) where the resonances present in (a) are smoothened. At higher fields, the plateau changes slightly, and at $B = 7.5$ T it appears to split into two parts which reach near $\frac{1}{2}G_0$ and slightly below $\frac{3}{2}G_0$ at higher gate voltage, with the additional field serving to smoothen the $e^2/h$ plateau. Bear in mind, the vertical axis of Fig. 6.14a and b have similar limits, while c and d get progressively lower, a direct comparison is shown in the appendix section 8.2. To probe device stability, the gate voltage was swept back and forth successively. The bottom row was recorded at $\sim 30$ mK with applied field, the pattern is reproducible, though some features stand out as more exaggerated than in the 2 K measurements, compare for example the 1 plateau in b and e and the small step around $V_{\mathrm{bg}} \sim 3$, as well as some of the features in the opening of the first conductance channel. The operating range of the device lies within roughly $V_{\mathrm{g}} = [-1.5, 5]$ V. Larger values did not yield sufficient change in conductance to warrant further probing. The series resistance of the contacts was fitted according to the principles described for the previous device,[i] with a fitted series resistance $R_S = 2.19$ kΩ.

Bias spectroscopy performed at 2 K (Fig. 6.15) and 30 mK (Fig. 6.16) yield a better picture of the first channel opening, with the expected half-plateau formation as the source-drain bias is varied, and plateau splitting as the magnetic field is increased. At higher conductance levels, the transport signatures become less obvious, with the zero field data being slightly obscured by resonances.

[i]The procedure is shown in the appendix 8.2, otherwise see Fig. 6.4 in the previous section.

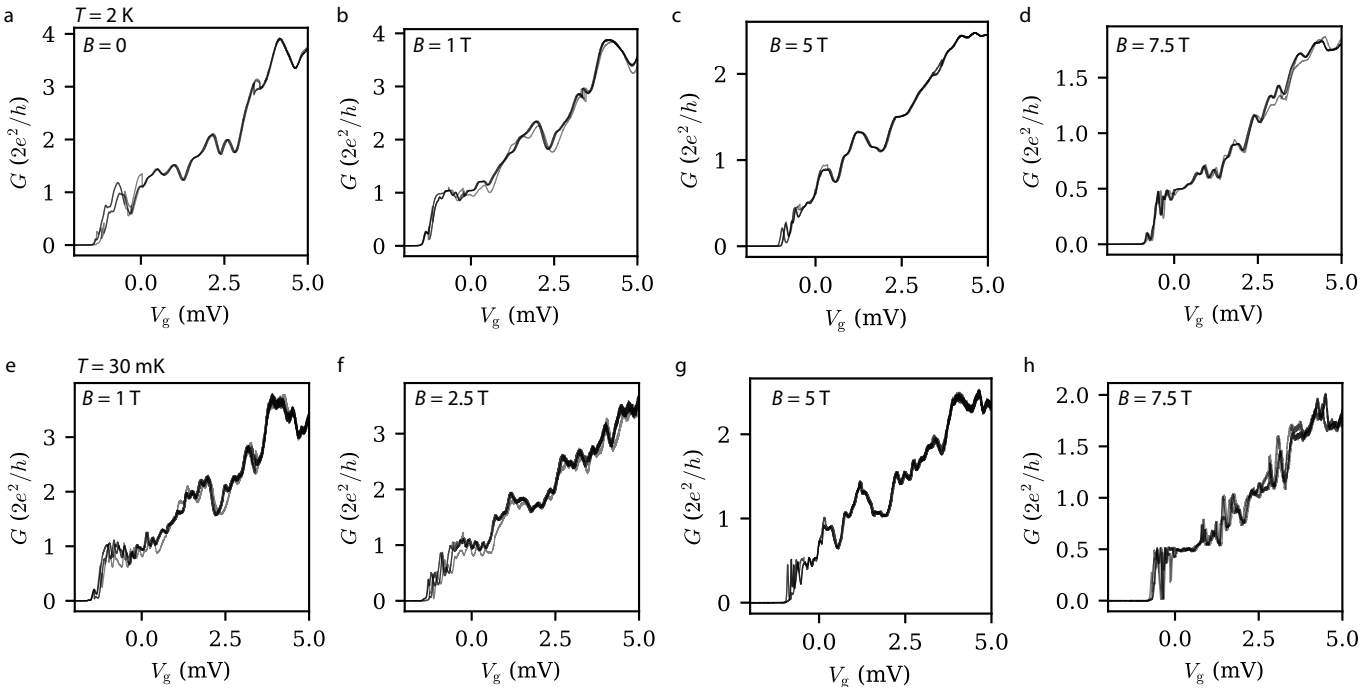


**Figure 6.14:** Gate-Conductance characteristics in the normal state. Top row: $T = 2$ K: **a.** $B = 0$. **b.** $B = 1$ T. **c.** $B = 5$ T. **d.** $B = 7.5$ T. Bottom: $T = 30$ mK, $B \geq 1$ T: **e.** $B = 1$ T. **f.** $B = 2.5$ T. **g.** $B = 5$ T. **h.** $B = 7.5$ T. Each plot features five traces, up- and down sweeps made successively, except **a** which features only four.

Fig. 6.15 shows bias spectra performed at $B = (0, 1, 5)$ T, with annotated values in units of $e^2/h$, from the $B = 1$ T spectra, we can see the formation of the $(1, 2, 3, 4, 6, 7)$ $e^2/h$ plateaus, in relatively good agreement with the theoretical model, though there are unexplained features in the spectra, for example the formation of the $3e^2/h$ plateau at finite $V_{\mathrm{sd}}$ seems to appear in two places (Fig. 6.15b).

Again, we end this section by probing the superconducting regime. Fig. 6.17 shows extended bias spectroscopy recorded at $T = 30$ mK and zero field. The bias spectrum shows a persistent ZBP, and gate dependent enhancement which appears to follow the pattern of resonances seen in the $V_{\mathrm{g}}$ sweeps for the device in the normal state (Fig. 6.14).

### Summary

In this section we have characterised an InAs/Al NW based device with a shadow patterned junction of approximately 350 nm, making junction is more than 3 times the width of the NW. It demonstrates quantised conductance in accordance with the expectations from a quantum point contact, with relatively clean channels up to conductance levels of $\sim 6e^2/h$, at least in the $T = 2$ K temperature range and with an applied field $B = 1$ T. We have probed the superconducting regime by bias spectroscopy, showing formation of the superconducing gap, and a persistent zero bias peak. Additional data on the magnetic field dependency of the gap at different gate voltages is compiled in the appendix.

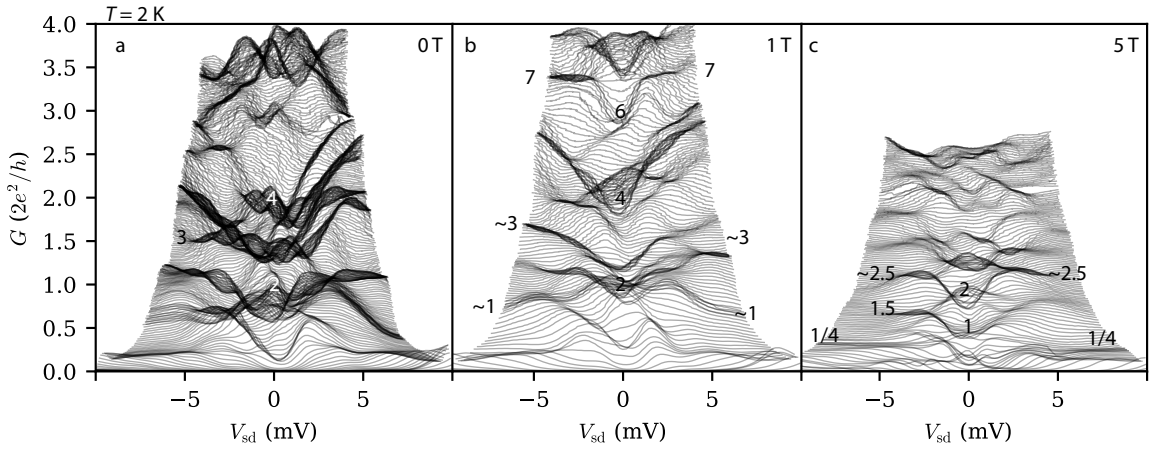


**Figure 6.15:** Bias spectroscopy of the device recorded at $T = 2$ K at increasing magnetic field (**a.**: $B = 0$, **b.**: $B = 1$ T, **c.**: $B = 5$ T). The annotated values are in units of $e^2/h$.

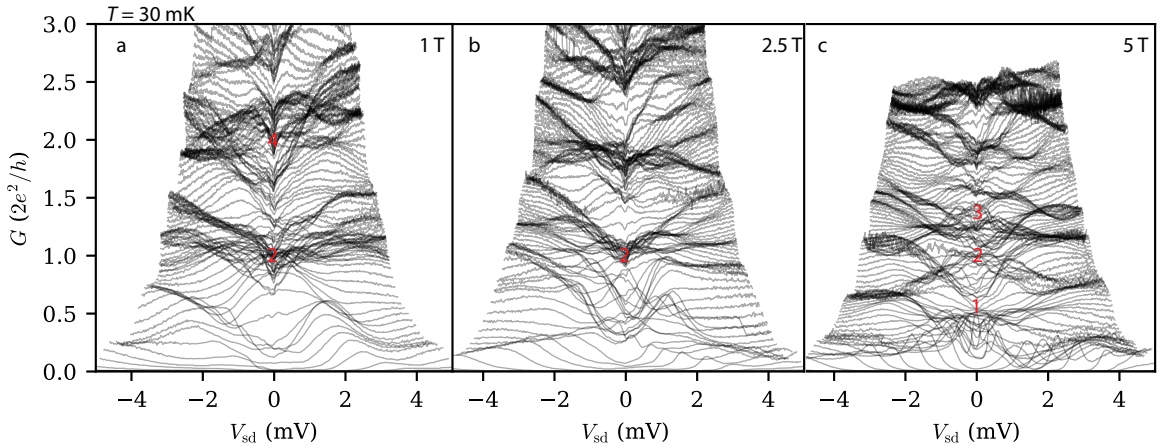


**Figure 6.16:** Bias spectroscopy of the device recorded at $T = 30$ mK at increasing magnetic field (**a.**: $B = 0$, **b.**: $B = 1$ T, **c.**: $B = 5$ T). The annotated values are in units of $e^2/h$.

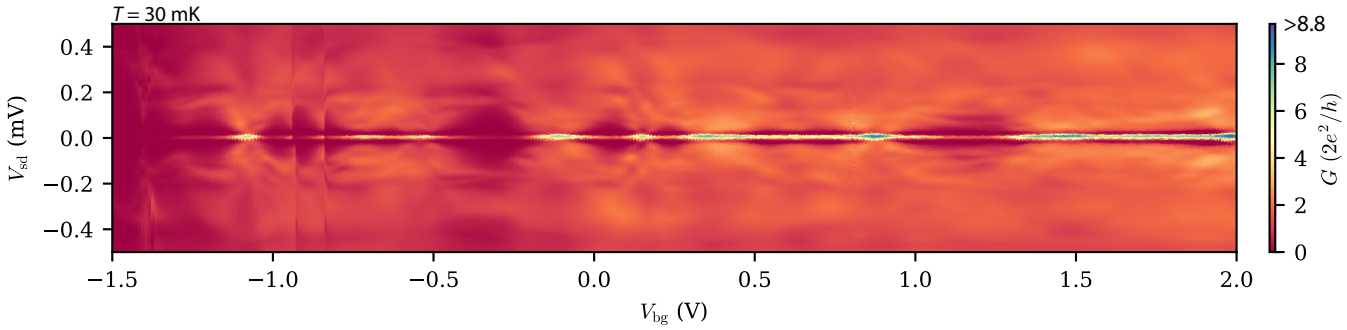


**Figure 6.17:** Gate-bias spectroscopy showing formation and persistence of ZBP.

# 7 Conclusion and Outlook

In this work, the shadow patterning method has been employed and expanded to for control over the junction formation on nanowires. We have extended the principles of shadow patterning by considering a multitude of factors that influence the possibilities for finely tuned designs. This has led to a set of geometrically derived equations which govern the selective deposition of in-situ evaporated thin-films onto nanostructures. Following this, a set of designs for the creation of multiple Josephson Junctions have been defined and tested. These demonstrated the formation of single, double, and triple Josephson Junctions, with good yield. The creation of a quadruple Josephson Junction was not successful, but the design yielded several double and triple junctions, in accordance to expectations.

A scheme for the in-situ double evaporation of two epitaxial, overlapping thin-films was created with the intention of creating an in-situ gold (Au) contact onto an epitaxial lead (Pb) thin-film. The design was successful, and demonstrates the flexibility of the use of secondary nanowires as the shadowing objects.

A total of 16 devices have been made to test shadow junctions in electron transport. Six of these could not be characterised due to issues from the bonding process, and from the remaining ten, two devices were displayed ballistic transport characteristics,. The two devices consisted of a 100 nm junction, and a 350 nm junction on two different nanowires. Ballistic transport was characterised by using the Quantum Point Contact as a reference model for an idealised 1-dimensional system. Bias spectroscopy revealed, in both cases, ballistic transport signatures under normal state conditions, with and without the use of an applied magnetic field. Future work should be directed at strengthening this claim, and at this time of writing, several devices have already been fabricated using the design schemes presented in this work.

By utilising the kinking ability of nanowires, the in-situ growth of the shadowing nanowires provides a flexible method for junction design, with no additional processing of the growth substrate. Thus, the method allows rapid prototyping of new designs, and generally quick fabrication of a large number of well defined hybrid structures. This scheme addresses some of the requirements for the realisation qubit relevant systems (Sec. 1).

Shadow deposition is gaining traction as an attractive alternative to conventional patterning by etching. A number of recent studies have displayed some sophisticated methods for creating shadowed junctions. By processing a chip with defined bonding paths, Heedt et al. and Borsoi et al. have created an integrated shadow-wall in the device substrate, allowing the superconductor to be deposited onto the already transferred nanowire.[47,56] The benefit comes in limiting exposure of the epitaxial film to ambient conditions, and it provides a reliable method for creating junctions with a prespecified length. Jung et al. have demonstrated a similar concept with a walled substrate acting as a shadow on selective area grown (SAG) networks.[57] Here, an indium phosphide (InP) substrate is covered in a silicium nitride (SiN) mask that is then etched to create

an access point to the substrate; the shadowing InP walls are then grown from the substrate. Etching the mask further, the indium anthimonide (InSb) SAG nanowire can then be grown from the substrate, and then shadowed.

The method used in this work, presents a different approach. Growing the shadowing nanowires in-situ, the junction is formed without breaking vacuum from the growth process, and should yield the cleanest possible interface between the film and the nanowire. The question remains, which is the most important; the semiconductor-superconductor interface, or the overall quality of the film itself. From a materials science perspective, this question could be addressed with a combination of transmission electron microscopy, and energy dispersive x-ray spectroscopy. Ultimately however, the result will be judged in terms of the transport properties, and should be supported by thorough statistical evidence.

The future of shadow junctions appears bright, and this work offers a contribution to the growing methodology behind the fabrication of designer nanostructures

# Bibliography


1. Doh, Y.-J. *et al.* Tunable Supercurrent Through Semiconductor Nanowires. *Science* **309,** 272–275 (2005).
2. Van Woerkom, D. J. *et al.* Microwave spectroscopy of spinful Andreev bound states in ballistic semiconductor Josephson junctions. *Nature Physics* **13,** 876–881 (2017).
3. Fu, L. & Kane, C. L. Superconducting Proximity Effect and Majorana Fermions at the Surface of a Topological Insulator. *Phys. Rev. Lett.* **100,** 096407 (9 2008).
4. Alicea, J., Oreg, Y., Refael, G., von Oppen, F. & Fisher, M. P. A. Non-Abelian statistics and topological quantum information processing in 1D wire networks. *Nature Physics* **7,** 412–417 (2011).
5. Mourik, V. *et al.* Signatures of Majorana fermions in hybrid superconductor-semiconductor nanowire devices. *Science* **336,** 1003–1007 (2012).
6. Albrecht, S. M. *et al.* Exponential protection of zero modes in Majorana islands. *Nature* **531,** 206–209 (2016).
7. Lutchyn, R. M. *et al.* Majorana zero modes in superconductor–semiconductor heterostructures. *Nature Reviews Materials* **3,** 52–68 (2018).
8. Prada, E. *et al.* From Andreev to Majorana bound states in hybrid superconductor–semiconductor nanowires. *Nature Reviews Physics* **2,** 575–594 (2020).
9. Aguado, R. A perspective on semiconductor-based superconducting qubits. *Applied Physics Letters* **117,** 240501 (2020).
10. Janvier, C. *et al.* Coherent manipulation of Andreev states in superconducting atomic contacts. *Science* **349,** 1199–1202 (2015).
11. Lutchyn, R. M., Sau, J. D. & Das Sarma, S. Majorana Fermions and a Topological Phase Transition in Semiconductor-Superconductor Heterostructures. *Phys. Rev. Lett.* **105,** 077001 (7 2010).
12. Oreg, Y., Refael, G. & von Oppen, F. Helical Liquids and Majorana Bound States in Quantum Wires. *Phys. Rev. Lett.* **105,** 177002 (17 2010).
13. Gill, S. T., Damasco, J., Car, D., Bakkers, E. P. A. M. & Mason, N. Hybrid superconductor-quantum point contact devices using InSb nanowires. *Applied Physics Letters* **109,** 233502 (2016).
14. Proposal, A. P. Andreev qubits for scalable quantum computation, andqc.eu (2021).
15. Krogstrup, P. *et al.* Epitaxy of semiconductor–superconductor nanowires. *Nature Materials* **16,** 400–406 (4 2015).
16. Chang, W. *et al.* Hard gap in epitaxial semiconductor–superconductor nanowires. *Nature Nanotechnology* **10** (3 2015).

17. Grove-Rasmussen, K., Jespersen, T., Jellinggaard, A. & Nygård, J. Hybrid Superconducting Devices Based on Quantum Wires. English (ed Narlikar, A.) (2017).

18. Deng, M. T. *et al.* Majorana bound state in a coupled quantum-dot hybrid-nanowire system. *Science* **354,** 1557–1562 (2016).

19. Tanta, R. *et al.* Morphology and composition of oxidized InAs nanowires studied by combined Raman spectroscopy and transmission electron microscopy. *Nanotechnology* **27,** 305704 (2016).

20. Kanne, T. *et al.* Epitaxial Pb on InAs nanowires for quantum devices. *Nature Nanotechnology* **16,** 776–781 (7 2021).

21. Carrad, D. J. *et al.* Shadow Epitaxy for In Situ Growth of Generic Semiconductor/Superconductor Hybrids. *Advanced Materials* **32,** 1908411 (2020).

22. Gazibegovic, S. *et al.* Epitaxy of advanced nanowire quantum devices. *Nature* **548,** 434–438 (2017).

23. Krizek, F. *et al.* Growth of InAs Wurtzite Nanocrosses from Hexagonal and Cubic Basis. *Nano Letters* **17,** 6090–6096 (2017).

24. Goffman, M. F. *et al.* Conduction channels of an InAs-Al nanowire Josephson weak link. *New Journal of Physics* **19,** 092002 (2017).

25. Gomes, U. P., Ercolani, D., Zannier, V., Beltram, F. & Sorba, L. Controlling the diameter distribution and density of InAs nanowires grown by Au-assisted methods. *Semiconductor Science and Technology* **30,** 115012 (2015).

26. Tchernycheva, M. *et al.* Au-assisted molecular beam epitaxy of InAs nanowires: Growth and theoretical analysis. *Journal of Applied Physics* **102,** 094313 (2007).

27. Cord, B. *et al.* Limiting factors in sub-10nm scanning-electron-beam lithography. *Journal of Vacuum Science & Technology B: Microelectronics and Nanometer Structures Processing, Measurement, and Phenomena* **27,** 2616–2621 (2009).

28. Raghunathan, A. & Hartley, J. G. Influence of secondary electrons in high-energy electron beam lithography. *Journal of Vacuum Science & Technology B* **31,** 011605 (2013).

29. Ihn, T. Semiconductor Nanostructures (2013).

30. Ren, Y. Spin Effects in Quantum Point Contacts (2011).

31. Büttiker, M. Quantized transmission of a saddle-point constriction. *Phys. Rev. B* **41,** 7906–7909 (11 1990).

32. Kouwenhoven, L. P. *et al.* Nonlinear conductance of quantum point contacts. *Phys. Rev. B* **39,** 8040–8043 (11 1989).

33. Martin-Moreno, L., Nicholls, J. T., Patel, N. K. & Pepper, M. Non-linear conductance of a saddle-point constriction. *Journal of Physics: Condensed Matter* **4,** 1323–1333 (1992).

34. Patel, N. K. *et al.* Ballistic transport in one dimension: additional quantisation produced by an electric field. *Journal of Physics: Condensed Matter* **2,** 7247–7254 (1990).

35. Pidgeon, C. R., Mitchell, D. L. & Brown, R. N. Interband Magnetoabsorption in InAs and InSb. *Phys. Rev.* **154,** 737–742 (3 1967).

36. Konopka, J. Conduction electron spin resonance in InAs. *Physics Letters A* **26,** 29–31 (1967).

37. Saldaña, J. C. E. *et al.* Coulombic subgap states (2021).

38. Vaitiekėnas, S., Deng, M. T., Nygård, J., Krogstrup, P. & Marcus, C. M. Effective $g$ Factor of Subgap States in Hybrid Nanowires. *Phys. Rev. Lett.* **121,** 037703 (3 2018).

39. Vekris, A. *et al.* Josephson junctions in double nanowires bridged by in-situ deposited superconductors (2021).

40. Das, A. *et al.* Zero-bias peaks and splitting in an Al–InAs nanowire topological superconductor as a signature of Majorana fermions. *Nature Physics* **8,** 887–895 (12 2012).

41. Csonka, S. *et al.* Giant Fluctuations and Gate Control of the g-Factor in InAs Nanowire Quantum Dots. *Nano Letters* **8,** 3932–3935 (2008).

42. Schroer, M. D., Petersson, K. D., Jung, M. & Petta, J. R. Field Tuning the $g$ Factor in InAs Nanowire Double Quantum Dots. *Phys. Rev. Lett.* **107,** 176811 (17 2011).

43. Gawarecki, K. & Zieliński, M. Electron g-factor in nanostructures: continuum media and atomistic approach. *Scientific Reports* **10** (2020).

44. Tadjine, A., Niquet, Y.-M. & Delerue, C. Universal behavior of electron $g$-factors in semiconductor nanostructures. *Phys. Rev. B* **95,** 235437 (23 2017).

45. Kanne, T. *et al.* Double nanowires for hybrid quantum devices (2021).

46. Bjergfelt, M. *et al.* Superconducting vanadium/indium-arsenide hybrid nanowires. *Nanotechnology* **30,** 294005 (2019).

47. Borsoi, F. *et al.* Single-Shot Fabrication of Semiconducting–Superconducting Nanowire Devices. *Advanced Functional Materials* **31,** 2102388 (2021).

48. Tanta, R. *et al.* Morphology and composition of oxidized InAs nanowires studied by combined Raman spectroscopy and transmission electron microscopy. *Nanotechnology* **27,** 305704 (2016).

49. Eisenstein, J. Superconducting Elements. *Rev. Mod. Phys.* **26,** 277–291 (3 1954).

50. Cochran, J. F. & Mapother, D. E. Superconducting Transition in Aluminum. *Phys. Rev.* **111,** 132–142 (1 1958).

51. Matthias, B. T., Geballe, T. H. & Compton, V. B. Superconductivity. *Rev. Mod. Phys.* **35,** 1–22 (1 1963).

52. Takei, S., Fregoso, B. M., Hui, H.-Y., Lobos, A. M. & Das Sarma, S. Soft Superconducting Gap in Semiconductor Majorana Nanowires. *Phys. Rev. Lett.* **110,** 186803 (18 2013).

53. Caplan, S. & Chanin, G. Critical-Field Study of Superconducting Aluminum. *Phys. Rev.* **138,** A1428–A1433 (5A 1965).

54. Winkler, G. W. *et al.* Orbital Contributions to the Electron $g$ Factor in Semiconductor Nanowires. *Phys. Rev. Lett.* **119** (3 2017).

55. Tinkham, M. Introduction To Superconductivity, second edition (2004).

56. Heedt, S. *et al.* Shadow-wall lithography of ballistic superconductor–semiconductor quantum devices. *Nature Communications* **12,** 4914 (2021).

57. Jung, J. *et al.* Universal Platform for Scalable Semiconductor-Superconductor Nanowire Networks. *Advanced Functional Materials* **n/a,** 2103062 (2021).

# 8 Appendix

## 8.1 Supplementary data for Ballistic transport signatures and QPC behaviour in a 100 nm shadow junction (Sec. 6.1)

### 8.1.1 Superconducting regime, extended data.

Fig. 8.1a shows a broad range gate sweep, with the onset of conductance around $V_{\mathrm{bg}} \sim -2.5$ V, marked by the formation of Multiple Andreev reflection (MAR) signatures in the finite bias regime that evolve into a zero bias peak which persists throughout the entire spectrum. The ZBP is periodically enhanced (corresponding roughly to the resonances in Fig. 6.11a) and MARs appear to converge towards the zero bias state periodically with the ZBP enhancement. Fig. 8.1b is a finer sweep of the opening of the device, showing formation of MAR features and the beginning of the ZBP. Fig. 8.1c shows three linescans taken at the very onset of conductance before the formation of the ZBP (orange), the beginning of the ZBP (purple), and within a stable region with clear MAR and ZBP (black).

### 8.1.2 Additional figures

The rest of the figures in this section comprise mainly of a supplementary 'look' at data that has already been presented, with the exception of the bias spectra Fig. 8.2 that were shown in a truncated version in the main text.

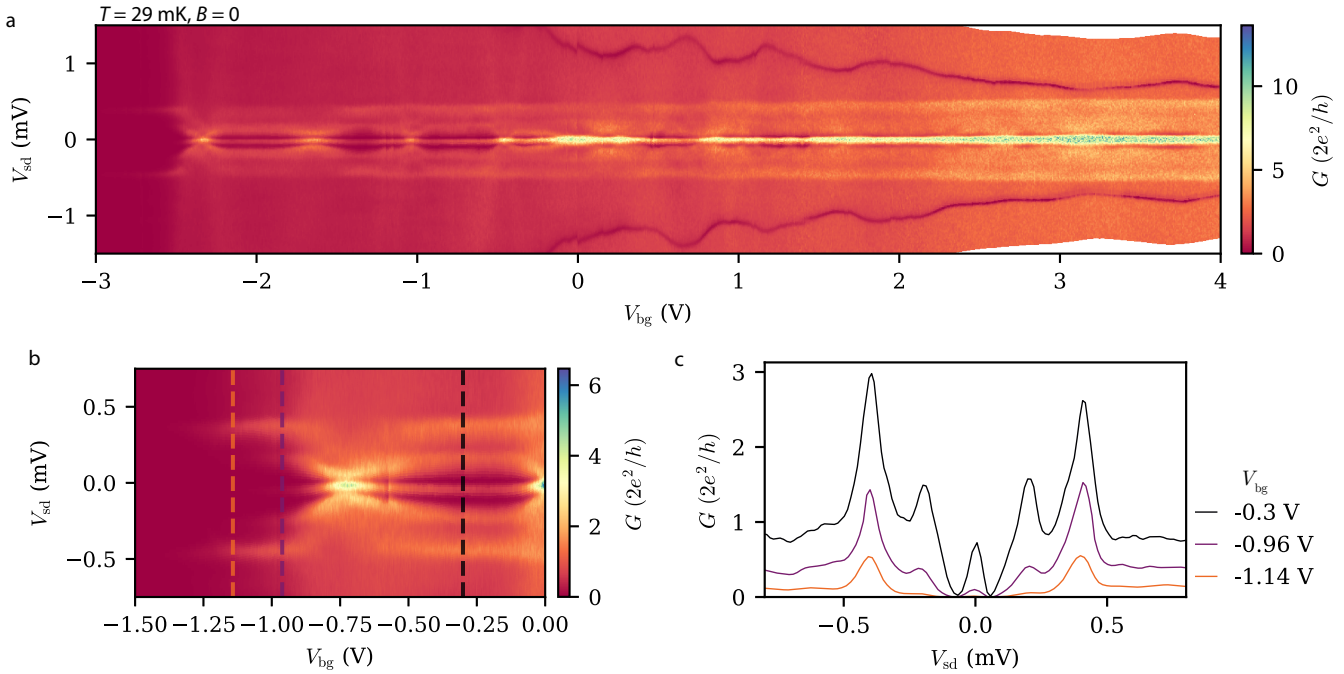


**Figure 8.1:** Superconducting regime bias spectrum. **a.** Coarse space measurement shows formation and maintenance of a ZBP. **b.** Fine measurement in the lower conductance regime showing the beginning of MAR signatures and the ZBP. **c.** Series resistance corrected linescan over the dashed lines in **b**, showing MAR enhancement and the onset of the ZBP.

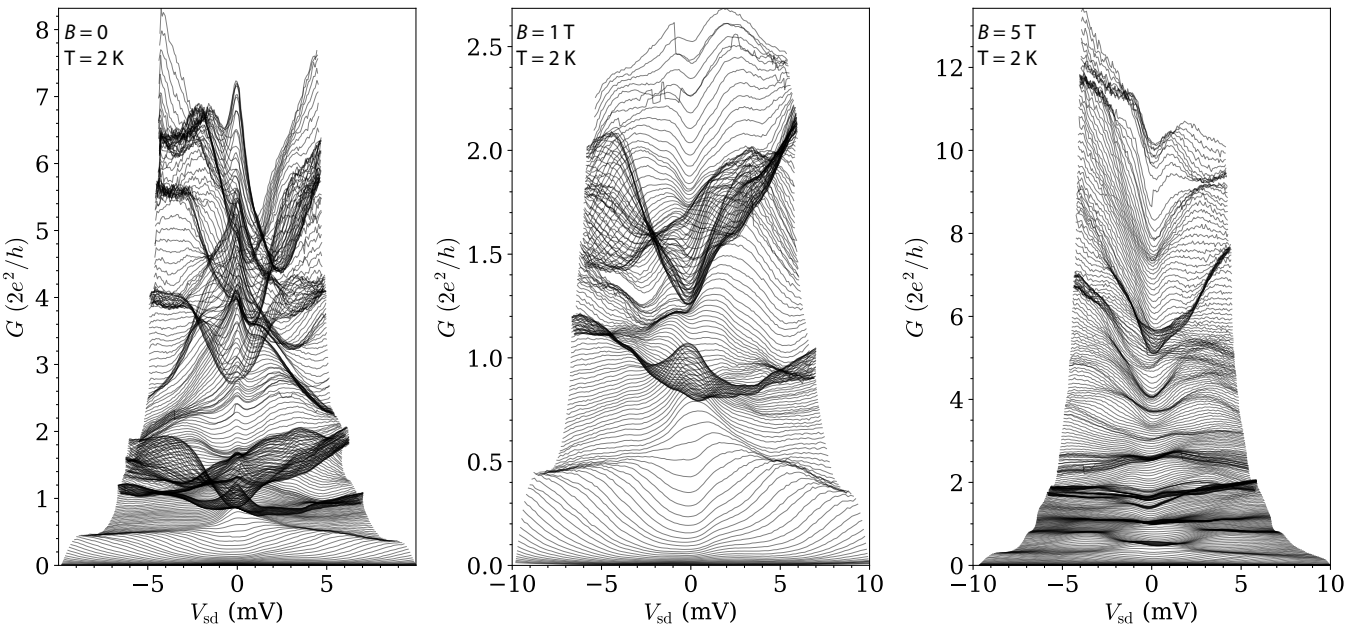


**Figure 8.2:** Supplementary to Fig. 6.6. Full range of the bias spectroscopy, recorded at $T = 2$ K, with a fixed sidegate $V_{sg} = -0.8$ V. Left to right: $B = 0$, $B = 1$ T ,$B = 5$ T. Data corrected for series resistance.

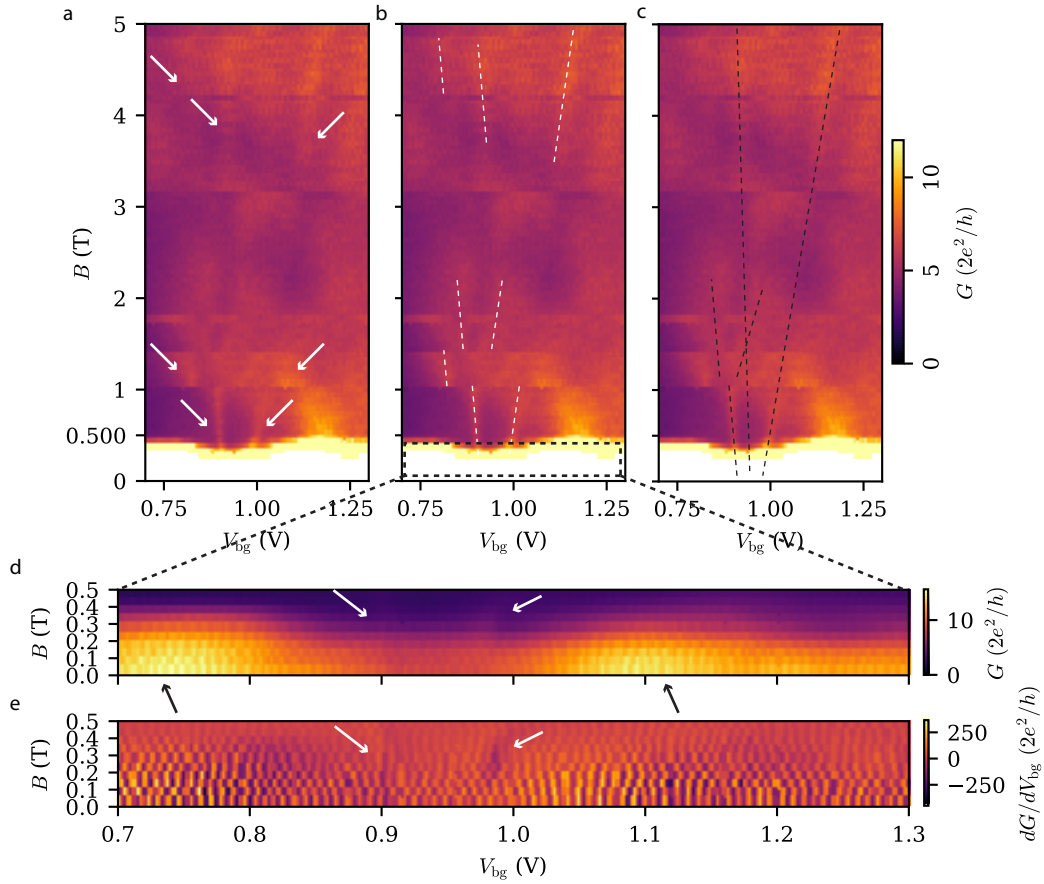


**Figure 8.3:** Supplementary to Fig. 6.9. Complementary annotations. **a.** Possible split peaks of lower and higher energies. **b.** Lines following the patterns pointed out in **a**. **c.** Following the pattern of the lower energy peak suggests a splitting an extra split, which would suggest that the two peaks are of different origin. Tracing the clearer high conductance peak suggests an even smaller $g$ factor than the extracted values, but requires the low conductance states to be the same, which is countered by their distance in gate space. **d.** Zoom-in with less saturated colourmap of the superconducting region. White arrows mark the beginning of the peak splitting. Black arrows mark the placement of the nearest large coherence peaks that would normally be assumed to produce peak splitting. **e.** Transconductance of the data in **d**.

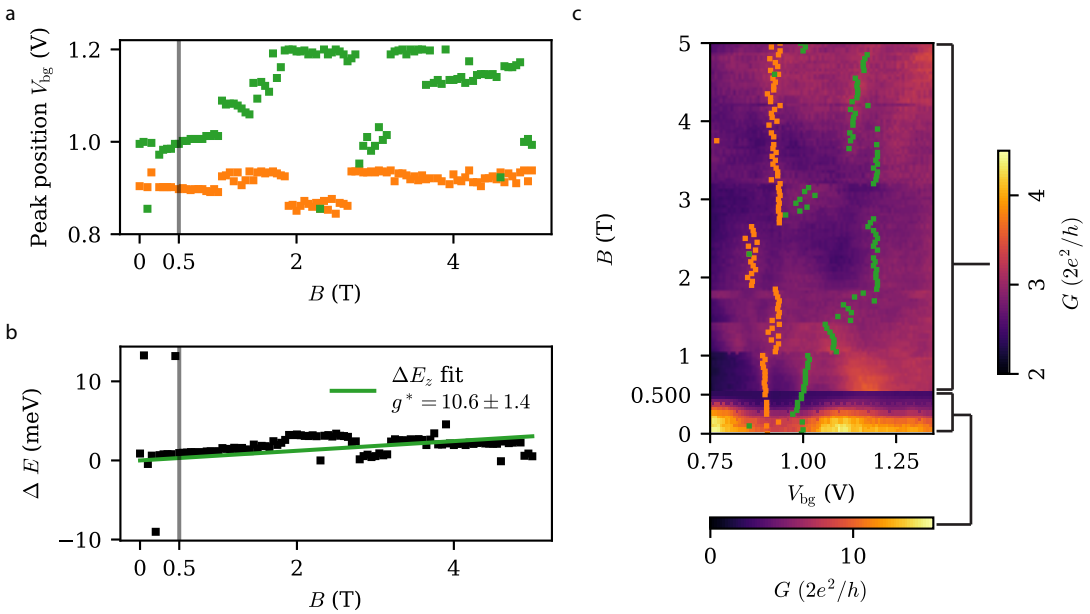


**Figure 8.4:** Supplementary to Fig. 6.10. Peak extraction of the $V_{bg} \sim 0.9$ V split peaks via peak extraction algorithm instead of line tracing the plot. **a.** Peak positions of the extracted peaks. **b.** Difference in gate voltage positions, converted to $E$ via the lever-arm extracted from Fig. 6.7 in the main text, fitted to Eq. (2.11) (fit quality parameters: $\chi^2 = 72$, NDOF $= 99$, Prob $= 0.98$). It can be argued that there is a systematic deviance to a higher value than the fitted line; and indeed from the extracted peaks it is clear that the extraction is not optimal. Nevertheless the high probability of the fit can be explained by the outliers becoming dominant contributors to the error; but being so few in number that the rest of the dataset appears much better than it perhaps is. **c.** Extracted peaks overlaid the colourmap of the spectrum, divided into two parts to better show the SC region and the normal state without saturating or underexposing the colour scales.

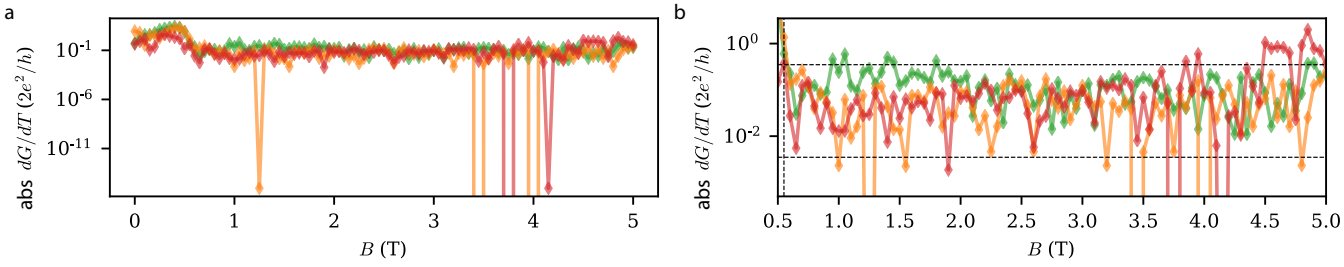


**Figure 8.5:** Supplementary to Fig. 6.11e. Both panels show the absolute residual to 0 for the derivative. **a.** The entire spectrum. **b.** Zoom-in on the region of interest in Fig. 6.11e, with dashed lines at 0.0035 $G_0$ and 0.35 $G_0$.

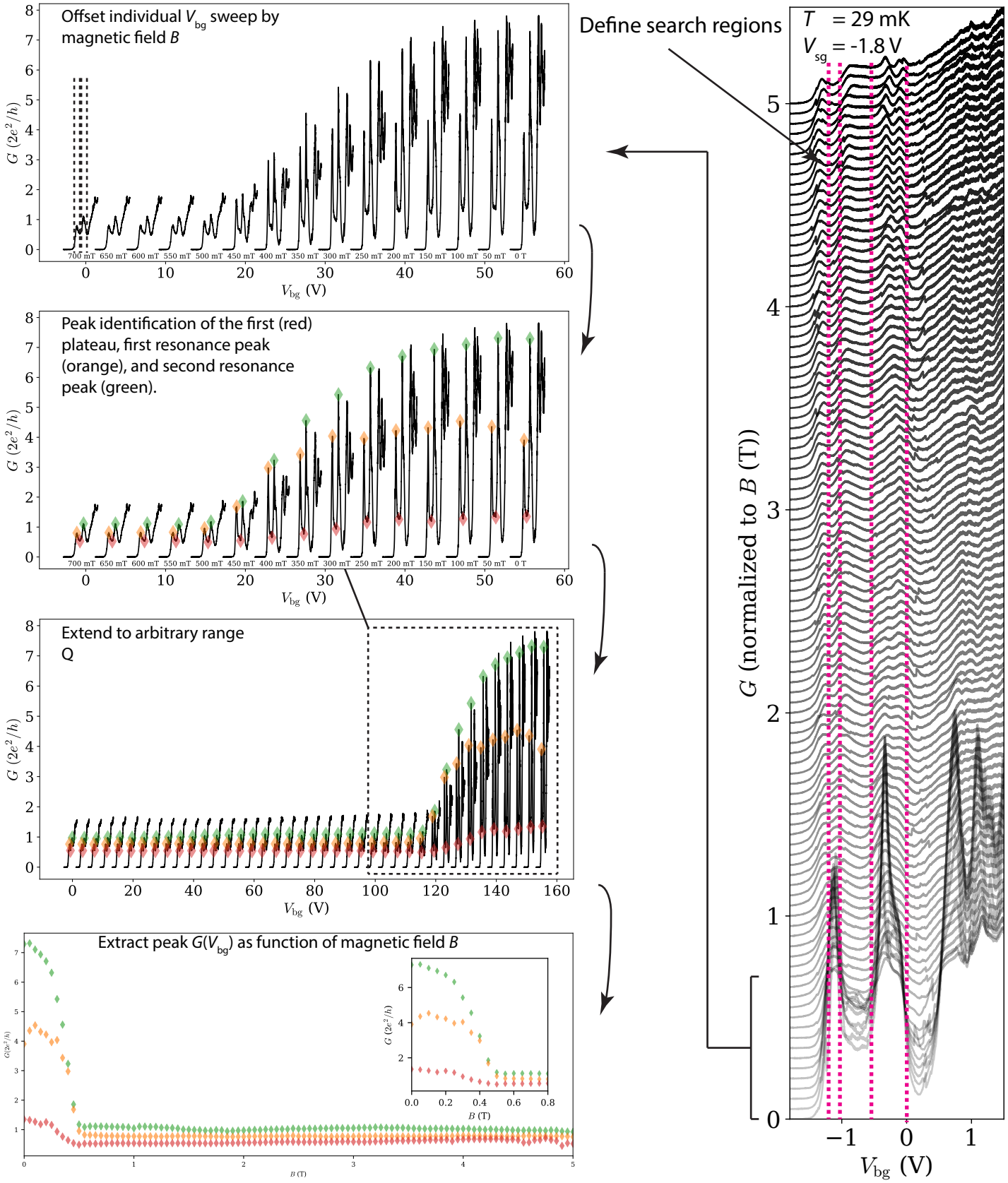


**Figure 8.6:** Supplementary to Fig. 6.11. Visual representation of the peak extraction procedure. Due to the relatively clear spectrum, defining a region of interest is straight forward. The specific algorithm is ad hoc to the dataset.

## 8.2 Supplementary data for Transport features in a 350 nm shadow patterned junction (Sec. 6.2)

### 8.2.1 Superconducting regime, extended data set

In the superconducting state, field-bias spectroscopy was performed by varying the field in units of 25 mT, while sweeping the source-drain voltage back and forth. Initial measurements were performed with the gate voltage set to zero. Fig. 8.7 shows the opening/closing of the superconducting gap as the field is increased, suppressing the superconducting regime as soon as $B \sim 180$ mT. Besides the gap itself, which appears rather soft, two signatures are present, a zero bias peak as well Andreev bound states exhibiting enhanced conductance. These states initially consist of two peaks on each side of the gap, which split into three discrete states at $B \sim 50$ mT, in the range $B = [50, 90]$ mT they are easily distinguished, and the upper (positive bias) middle state can be followed until $B \sim 120$ mT, after which it dissipates, followed by the inner state as the field is increased further. Fig. 6.17 shows extended bias spectroscopy in the superconducting state and four selected field-bias spectra at increasing gate voltages. The bias spectrum (Fig. 8.8a) shows a persistent ZBP, and gate dependent enhancement which appears to follow the pattern of resonances seen in the $V_g$ sweeps for the device in the normal state (Fig. 6.14 in the main text). Varying the gate voltage shows that there are instances where enhancement of the ZBP allows it to persist at higher $B$-field, notably Fig. 8.8b and d show a sensitive ZBP, which diminishes prior to the closure of the gap, while Fig. 8.8c and e show a ZBP that persists until the gap closes. Comparing Fig. 8.8b and d to Fig. 8.8c and e, it appears that these more *sensitive* ZBPs appear in spectra that have a more simple gap, less populated by bound states. The spectrum in Fig. 8.8e has a particularly rich set of features, and linescans across the gap (Fig. 8.9) taken at fields $B = (0, 0.04, 0.07)$ T shows what to be three distinct bound states in addition to the ZBP.

The ZBP sensitivty to the magnetic field has been shown to be increased when the field is oriented perpendicular to the NW,[40] although the particular study was performed on a junctionless InAs/Al NW. In our case, where the perpendicular component is relatively strong, it is therefore not so surprising to see the dissipation of superconductance at a much earlier stage than with the previous device, although it is comparably maintained for twice as long as the reported value ($\sim 95$ mT) in Ref. [40].

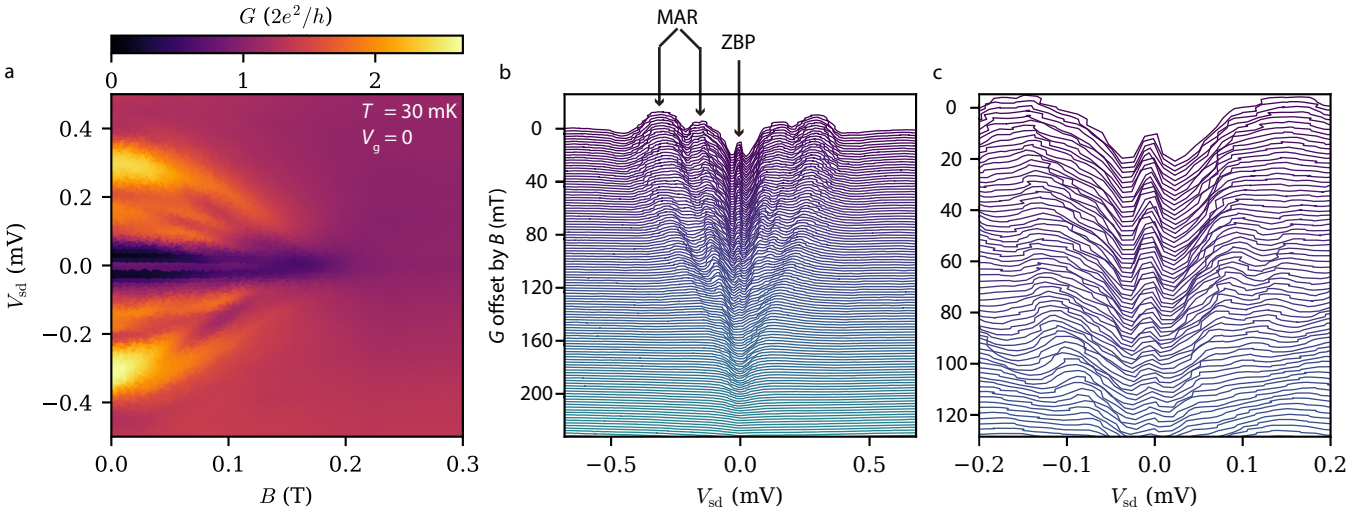


**Figure 8.7:** Field spectroscopy of the opening of the superconducting gap. A small zero bias peak present. States in the gap merge as the superconducting features dissipate by the application of increased field. The effect subsides rather early, at $B \sim 180$ mT. **a.** Colourmap representation. **b.** Zoomed lineplot, offset by $B$, each trace is spaced by 2 mT. **c.** Focus zoom on the inner gap.

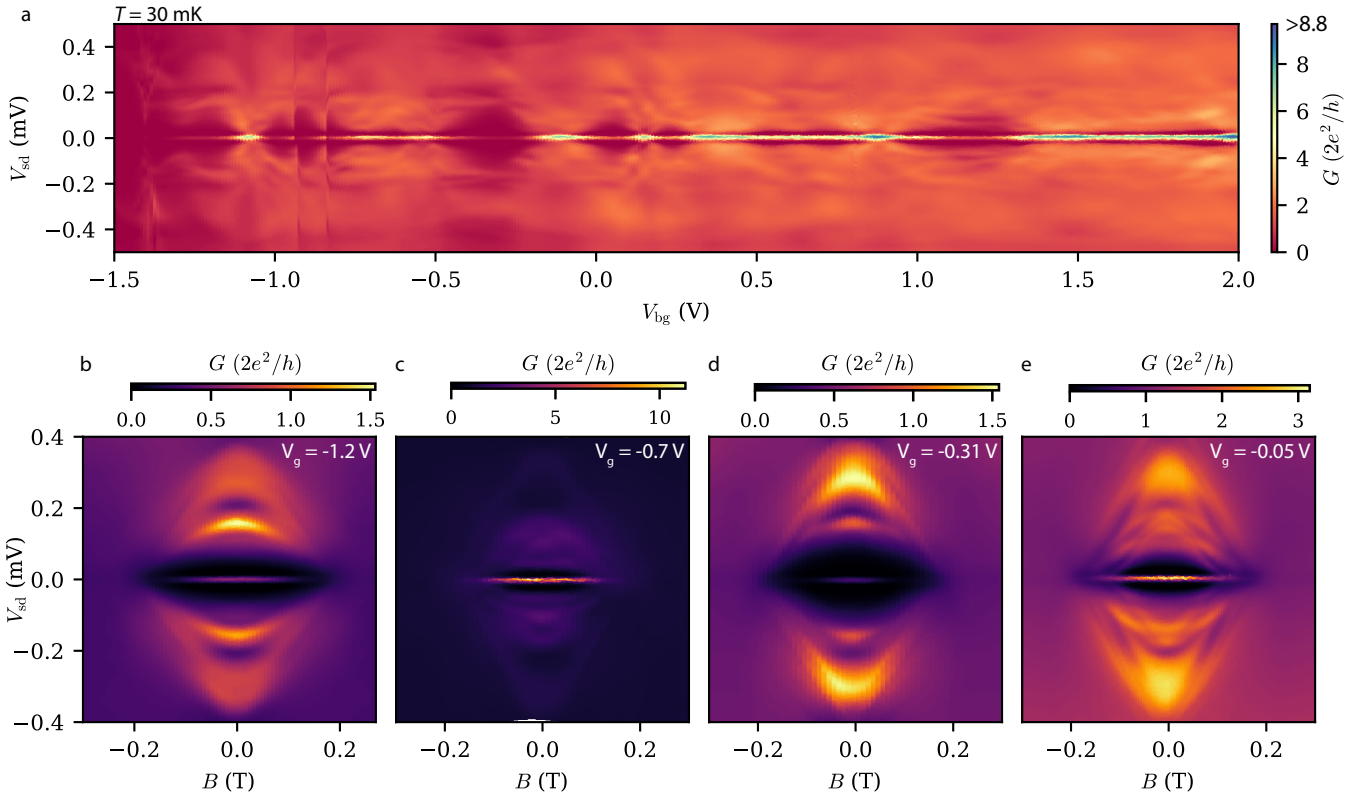


**Figure 8.8:** Gate-bias spectroscopy and field-bias spectroscopy at selected gate voltages. **a.** Gate-bias spectroscopy showing formation and persistence of ZBP. Field-spectroscopy shows opening/closing of the gap at different gate voltages $V_g$, **b.** -1.2 V, **c.** -0.7 V, **d.** -0.31 V, and **e.** -0.05 V. The spectra **b** and **d** show a ZBP that is more sensitive to the magnetic field relative to **c** and **e**. The spectra **b** and **d** are generally less feature rich as well, with **c** and **e** displaying what appears to be several bound states in addition to the ZBP.

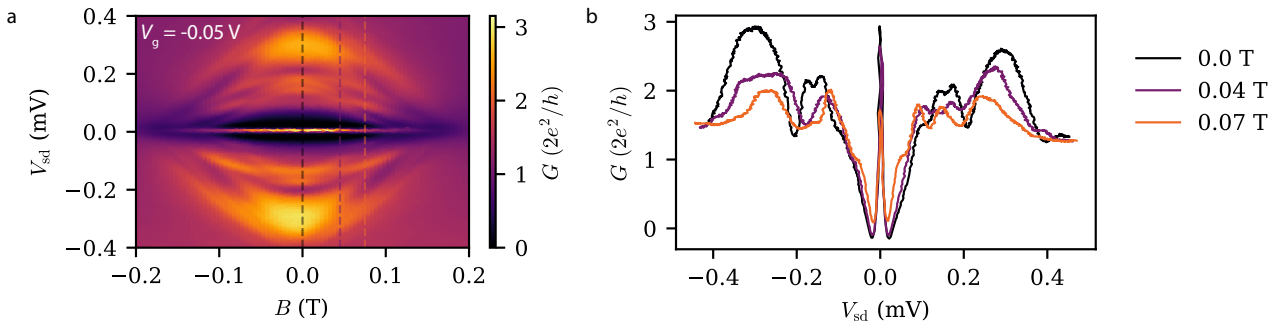


**Figure 8.9:** Linescans across the gap shown in Fig. 6.17e. **a.** The field-bias spectrum at $V_{\mathrm{bg}} = -0.05$ V, corresponding to $G \sim 2e^2/h$ in the normal state. Dashed lines indicate the placement of linescans. **c.** Linescans as shown on **a**, displaying ZBP and MAR features.

### 8.2.2 Extended bias spectroscopy and fitting of contact resistance

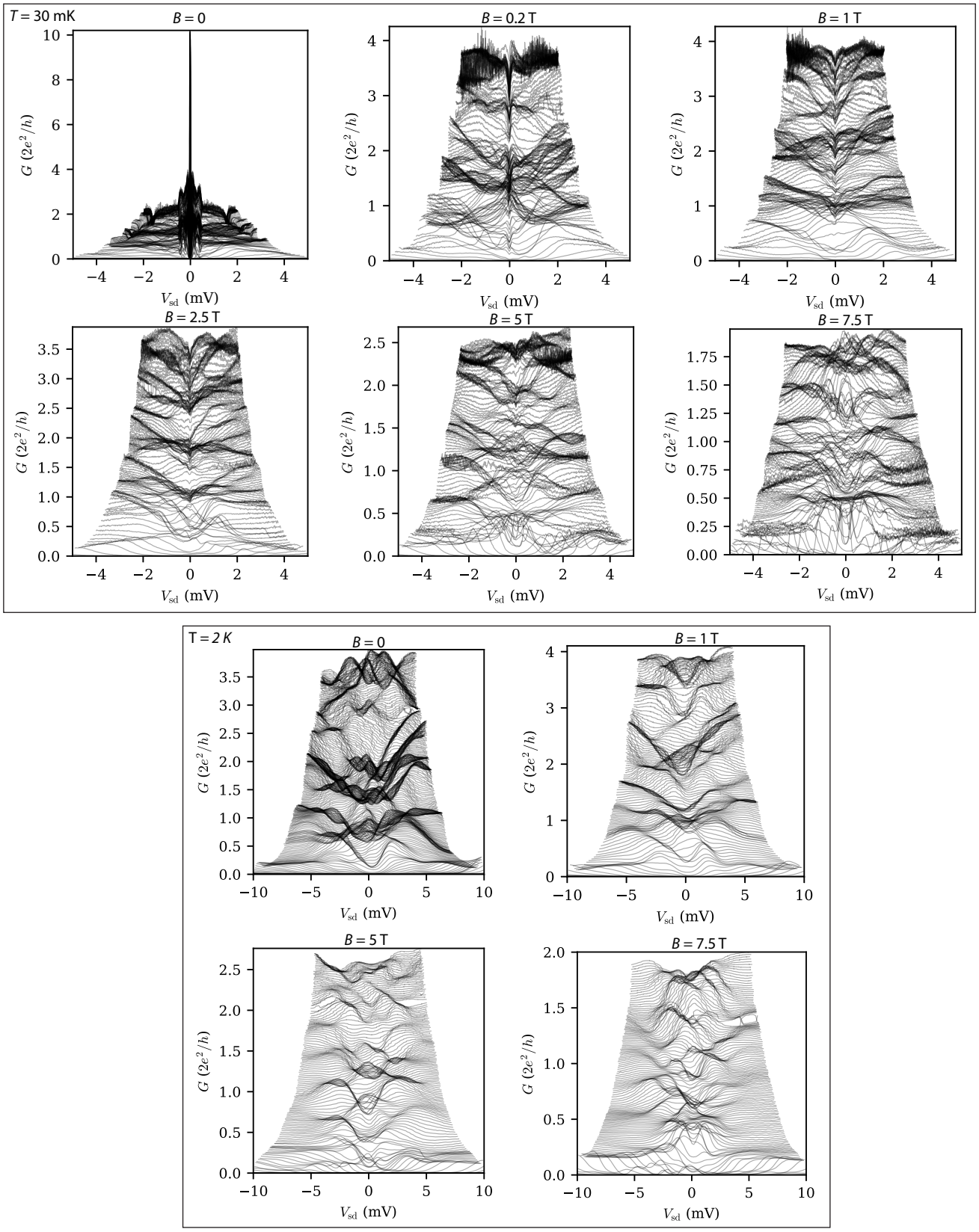


**Figure 8.10:** Supplementary bias spectra to Fig. 6.15 and Fig. 6.16. Top: Recorded at $T \approx 30$ mK. Bottom: Recorded at $T = 2$ K.

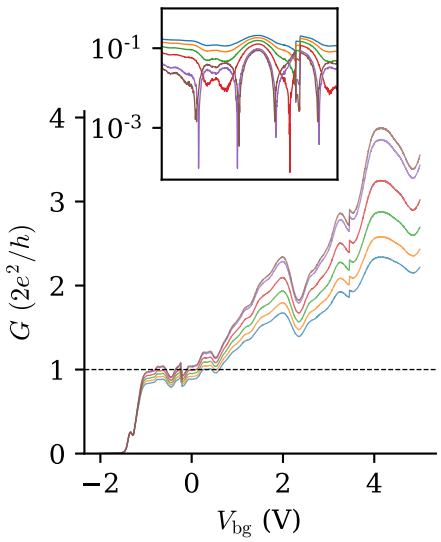


**Figure 8.11:** Fitting the series resistance by minimising the residual to the $G_0$ plateau of the conductance curve within the range $V_{\mathrm{g}} = [-1, 0]$ V. Blue: 0 subtraction of the series resistance. Orange: $0.02h/e^2$ subtracted. Green: $0.04h/e^2$ subtracted. Red: $0.06h/e^2$ subtracted. Purple: $0.08h/e^2$ subtracted. Brown: $0.085h/e^2 = 2.19$ kΩ subtracted (the fitted series resistance). The inset shows the absolute residual within the fitted range.

## 8.3 List of designs/growths

The following list details all substrate designs that resulted in growths during the production of this work.

1. QDEV1005 - InAs/Al, trial for shadow junctions.
2. QDEV1014 - InAs, closely grown nanowires for networks; fence/train track design.
3. QDEV1015 - InAs/Pb-Au, in-situ evaporation of Au contact to Pb thin film.
4. QDEV1016 - InAs/Al, shadow junctions. Nanowires did not kink due to error in the growth process.
5. QDEV1018 - InAs/Al, shadow junctions.
6. QDEV1019 - InAs, closely grown nanowires for cross-section networks; fence/crosses/pound (#).